Volumetric PIV Measurement in the Wake of Wavy Cylinder

by

Chin Hao Chang

A Thesis submitted to the Graduate Faculty of
Auburn University
in partial fulfillment of the
requirements for the Degree of
Master of Science

Auburn, Alabama
August 02, 2014

Keywords: Wavy cylinder, Flow control

Approved by

Anwar Ahmed, Chair, Professor of Aerospace Engineering
Roy Hartfield, Walt and Virginia Woltosz Professor of Aerospace Engineering
Jay Khodadadi, Alumni Professor of Mechanical Engineering

Abstract

The three-dimensional laminar flow over a straight cylinder with sinusoidal variation of cross-section was investigated using a volumetric Particle Image Velocimetry at Reynolds numbers of 15,000 and 20,000 and compared with the wake of a straight cylinder. It was observed that the boundary layer separation line was also wavy since the flow separated earlier with saddle-type attachment and later for the case of nodal attachment. Consequently, the wake was narrower behind the nodes and wider behind the saddles. The results were compared with a straight cylinder wake. Spatial characteristics of the flow suggest the presence of streamwise vortices that form midway between the saddle and the node and extend downstream. Interactions of these vortices with the von Karman vortices result in significant distortion of the coherent structures, increase the vortex formation length and suppress the large scale spanwise vortex formation. The Proper Orthogonal Distribution of the PIV data in several planes indicated that the overall energy contents of the wavelength $\lambda/D = 1.6$ was lower than the straight circular cylinder.

Acknowledgments

The author would like to thank Dr. Anwar Ahmed and Dr. M. Javed Khan for their instruction, patience, and expertise in the development of this thesis; they have been invaluable and have helped me to grow. I would also like to thank Mr. Bruce E. Heath, whose expertise on machining and willingness to give me his advice helped at every stage of the experiment. Thanks are also given to Mr. Hamza Ahmed, Mr. Abhishek Bichal and Ms. Man Ju Chih for their support, encouragement, and assistance while working in the lab. Last, but not least, the author would like to acknowledge his family for their patience and emotional support during the studies.

Table of Contents

List of Figures

List of Table

Nomenclature

A	Amplitude
C	Correlation Matrix
D	Diameter
D_{max}	Maximum Diameter
D_{min}	Minimum Diameter
D_{mean}	Mean Diameter
λ	Wavelength
λ_j	Eigenvalue
ϕ_j	Eigenvector
U_∞	Free Stream Velocity
ρ	Density
ω	Vorticity, $\frac{\omega D_{mean}}{U_\infty}$
V	Velocity
V_N	Number of snapshots
Re	Reynolds Number based on mean diameter, $\frac{\rho V_\infty D_{mean}}{\mu}$

PIV Particle Image Velocimetry

V3V Volumetric 3-conponemt Velocimetry

Chapter 1

Introduction

Cylinders are encountered in various applications such as antennas, offshore platforms, bridge cables, bridge pylons, bridge ropes, cooling towers, smoke stacks, oil delivery pipes, tall buildings, and heat exchanger tubes. The flow over the smooth circular cylinder has been widely studied because of the very unique and complex flow characteristics. As Reynolds number reaches a certain value, the vortex shedding that takes place results in the structural vibrations and fluctuating longitudinal and transverse forces due to fluid-structure coupling and resonance. An illustration of cylinder flow presented in Figure 1 shows the complexity of the flow encountered in bluff body wakes.

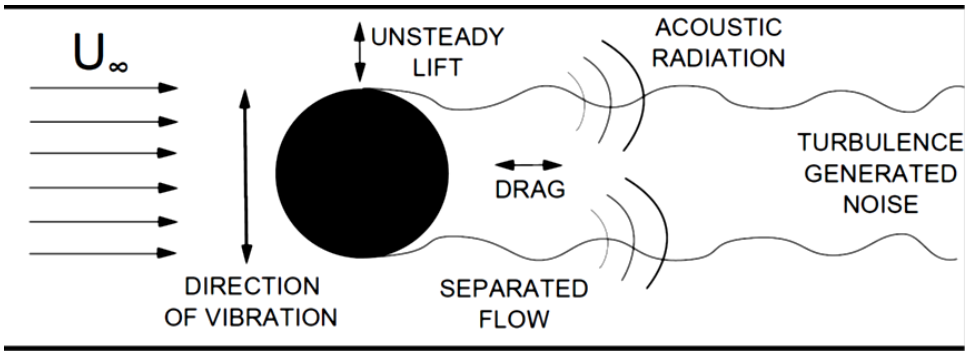

Figure 1. Cartoon of flow around a bluff body

The Tacoma Narrows bridge is a classic example of the consequence of vortex induced vibrations (Figure 2).

Figure 2: Tacoma Narrows Bridge

1.1 Description of bluff body flow

Flow over the bluff body has been classified in three different Reynolds number dependent flow regimes: creeping flow regime, steady separation regime, and periodic flow regime [1]. Between the Reynolds number ($0 < Re < 5$), the flow is termed creeping flow where the viscous forces are much larger compared to the inertial forces and flow therefore remains attached. At a Reynolds number from 4 to 5, the boundary layer separates and creates two steady and symmetric eddies in the wake. The free shear layer meets with the symmetric near wake at the end of the near wake, at the confluence point. At a Reynolds number from 4 to 48, the flow shows a steady separation regime and a pair of vortices forms in the wake of cylinder [2]. Due to the Helmholtz instability, the flow becomes unstable approximately near $Re = 30$ and is characterized by the closed near wake becoming elongated. The shear layer forms because the boundary layer separates due to the adverse pressure gradient imposed by the divergent geometry of the bluff body. The onset of periodic oscillations of the shear layer is initiated at the confluence point, and as the Reynolds number continues to increase the amplitude of flow oscillation behind the body also increase, as shown in Figure 3. The boundary layer contains vorticity which feed into the shear layer formed downstream of the separation point and induce the shear layer to roll up into a vortex. Therefore, when the Reynolds number reaches certain value, these vortices shed periodically from either side of bluff body, inducing the famous phenomena known as the von Karman Vortex street [3].

Figure 3. Laminar von Karman street at Reynolds number of 140 [4]

Gerrard [2] [5] described the vortex shedding in the following way: Vortex A shown in Figure 4.a, becomes strong enough to attract the opposing Vortex B across the near wake. Then the Vortex A separates from the shear layer, due to the approach of opposite sign of vorticity which breaks off the supply of vorticity to Vortex A from the boundary layer. Vortex A sheds downstream as Helmholtz vortex [2]. Furthermore, Figure 4.b shows Vortex A shedding off the body due to Vortex B cutting off the supply vorticity. At the same time, Vortex C forms on the same side of the bluff body and Vortex B replaces the role of Vortex A. Vortex B now grows in strength and size and attracts Vortex C across the wake. This induces the Vortex B to shed. This process repeats each time when a new vortex is shed at either side of the cylinder and the shedding continues in an alternate manner. Moreover, the vorticity shows clockwise direction in the Vortex A, whereas the vorticity shows anti-clockwise direction in Vortex B. Gerrard [13] describes how the shear layer is entrained in the separated regimes and is shown in Figure 5: (a) the shear layer is entrained into growing vortex, (b) and another part push into developing the shear layer, (c) and the last part induces a low pressure region of circulation.

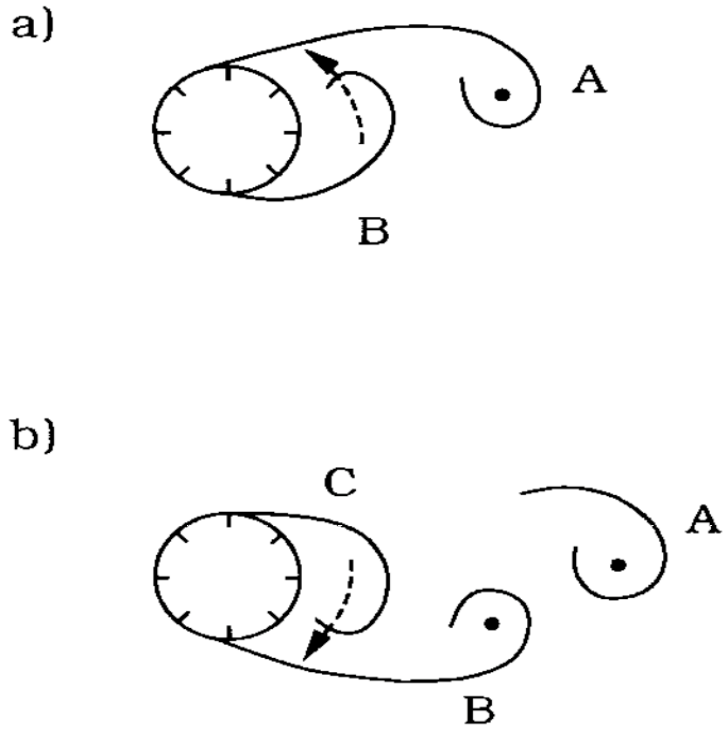

Figure 4: (a) Vortex A prior to shedding, and attracts Vortex B across the wake.
(b) Vortex B prior to shedding and attract Vortex C across the wake [2]

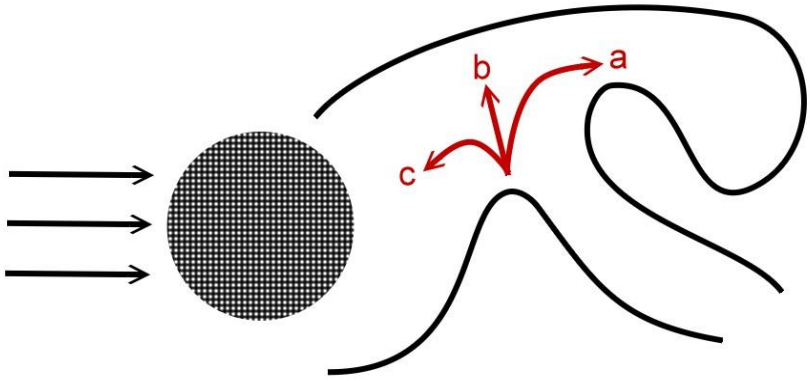

Figure 5: Sketch of shear layer entrainment [5]

For the range of Reynolds number 40 < Re < 200, shedding of vortices is predominantly two-dimensional and the vortex street is laminar. In the range of Reynolds number 200 < Re < 300, the wake begins to transition to turbulent. In the wake, the laminar flow is unstable and transitions, and gradually extends upstream until an eddy becomes turbulent during its formation. For Re > 300, the wake completely transitions to turbulent.

For Reynolds numbers ranging from 300 < Re < 300,000, flow is classified as a "subcritical regime" because the boundary layer remains laminar on the surface of the cylinder and the transition to turbulent flow occurs in the wake. With increasing Reynolds number, the transition location moves upstream towards the forward stagnation point. Increasing the Reynolds number increases the length of vortex formation; also, the shear layer becomes unstable and stronger downstream [15].

For the range of Reynolds number 300,000 < Re < 350,000, the flow regime is known as "critical regime". In this regime the boundary layer becomes turbulent at the separation point. Furthermore, non-zero mean lift occurs in this range due to the asymmetry of the flow.

For the range of the Reynolds number 350,000 < Re < 1,500,000, a "supercritical flow regime" sets in. In this regime, on both sides of the cylinder the boundary layer separation is turbulent.

1.2 Flow control

Viscous effects dominate at low Reynolds number and manifest themselves in the form of high viscous drag; however with increasing Reynolds number, because of the boundary layer separation, a large wake generates high pressure drag in addition to the unsteady forces. Modification of the wake to alleviate the negative effects fall in the category of flow control that is categorized as:

(1) Passive flow control

(2) Active flow control

1.3 Passive flow control

The passive flow control method controls the flow by modifying the body geometry or surface geometry with an aim to conquer the flow characteristics such as suppression of vortex shedding, reduction of the fluctuating mean drag. Blevins [16] indicated that the reduction of vortex-induced vibration on circular cylinders could be achieved by many methods: for instance, by avoiding resonance, reduced damping, streamlining of the cross-section, and by adding a vortex suppression devices. Because of the difficulties associated with improving damping to prevent resonance, only the last method is often utilized in practice. Geometric changes to a bluff body such as the helical strakes, splitter plates, hemispherical bumps, perforated shroud, narrow strip, ribbon cable, spoiler plates, cylindrical rings and axial slates etc. have shown promise. These devices aim to either suppress the strength of shed vortex or to induce three-dimensional flow by shedding vortices. Sumer [2] points out that the vortex shedding only happens when the two points out that the vortex shedding only happens when the two shear layers interact with each other. Hence, the interaction is restrained in one way or another, for instance by using a splitter plate at the downstream side between the two shear layers of the cylinder prevents shedding. Owen and Bearman [17] used the hemispherical bumps attached on the circular cylinder and circular cylinder with a sinuous axis. The results show a significant reduction in drag and vortex shedding with up to 25% with hemispherical bumps and up to 47% with a sinuous axis, due to the separation lines on a circular cylinder is forced to be sinuous. Nakamura and Igarashi [18] successfully reduced drag and fluctuating force approximately 15% for a circular cylinder exposed to cross-flow by attaching cylindrical rings along span. Liu, Shi and Yu [19] studied the comparison between the wake behind the circular cylinder and grooved cylinder. The results show that in the wake behind the grooved cylinder, the recirculation

zone was elongated by nearly 18.2% compared to a circular cylinder. Shoa, and Wang [20] used a narrow strip to suppress vortex shedding; the narrow strip was set parallel to the cylinder surface then adjusted the distance between cylinder surfaces and the angle. It was found that narrow strip successfully suppressed the wake at certain angle range from 30 to 55 degrees. Ahmed, Khan and Bays-Muchmore [9][21] studied the flow pattern over the wavy cylinder. The study indicated the boundary layer separates at the geometric saddles much earlier than the geometric nodes, and the wake behind the wavy cylinder at geometric nodes was narrower and faster velocity recovery rate compared to geometric saddles.

1.4 Present research on passive flow control

Bearman and Tombazis [22][23] introduced a wavy body with half-ellipse shape and spanwise wavy in conjunction with blunt trailing edge (Figure 6). It was found that increasing the wave steepness causes the base drag to decrease with lower base drag occurring at a peak. Also, the longest vortex formation occurred where the base pressure was lowest. Bearman and Owen [24] investigated reducing the bluff body drag by introducing the blunt spanwise wavy surface leading edge and blunt trailing edge of square cross-section (Figure 7). The experiment was conducted at the Reynolds number 40,000, and drag reduction of 30% was achieved for the wave amplitude between 0.06 and 0.09. Darekar and Sherwin [10][25] used the numerical methods to investigate the flow past the square cross-section cylinders with a wavy stagnation face (Figure 8). This was effective in suppressing the Karman vortex shedding due to three-dimensional shear layers by diverting spanwise vorticity into streamwise and vertical components of vorticity, which made the shear layers less susceptible to roll up in to the Karman vortex. Drag reduced by approximately 16% at Reynolds number of 100, but the drag slightly increased at higher Reynolds numbers compared to the smooth cylinder.

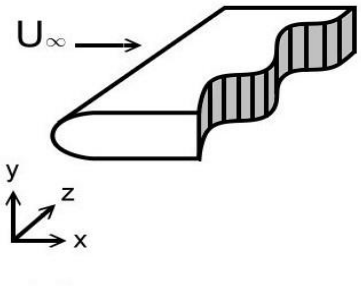

Figure 6: Rear Wavy cylinder [22]

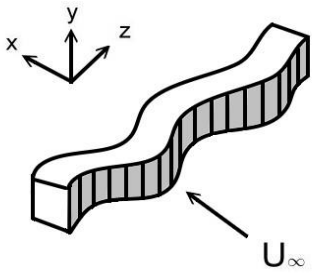

Figure 7: Square section wavy cylinder [24]

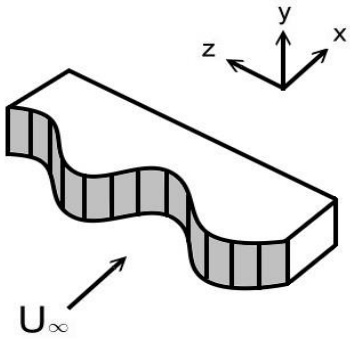

Figure 8: wavy Stagnation surface

Moreover, Kim and Choi [27] adopted active flow control methods investigating the flow over a circular cylinder at Reynolds numbers 40 to 3,900 by forcing the slot to blow and suction at the top and bottom surfaces. The forcing outlines are sinusoidal in the spanwise direction and have two different phases: the in phase distributed forcing and the out phase distributed forcing (Figure 9). The Karman vortex shedding was reduced not only in laminar flow conditions, but also in turbulent flow conditions. The in phase distributed forcing reduced the mean lift and mean drag fluctuations for all Reynolds numbers, and the maximum drag reduction occurred at the Reynolds number 100. Due to the vortex shedding mismatch, the phase along the spanwise direction that the in phase distributed produced then reduces the drag [27]. The out phase distributed forcing reduced the mean lift and mean drag

fluctuation at Re = 3,900, due to the separating shear layer distortion and vortex shedding occurring in the further downstream direction, but it does not reduce the drag at low Reynolds numbers.

Figure 9: Cylinder with active control, left showing the in-phase mode and right showing the out-phase mode

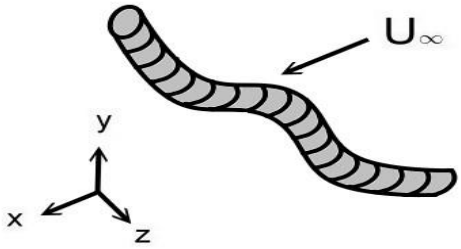

Figure 10: Sinusoidal wavy body

Furthermore, a cylinder with the diameter sinusoidal variation along the spanwise direction and the circular cross-section is named wavy cylinder. Due to the geometry of the wavy cylinder, three-dimensional flow can be naturally created. Ahmed and Bays-Muchmore [9] studied the wavy cylinder using the same amplitude but different wavelengths and found the drag coefficients at the geometric nodes were greater than at the geometric saddles. Moreover, painting dye on the surface of a wavy cylinder shows the separation obviously was three-dimensional and the distortion is greater at shorter wavelength wavy cylinder. The topology of the surface shear stress filed and flow visual manifest that there exists a saddle point of separation at each geometric saddle, and that the boundary layer rolls up into

streamwise vertical structure near the geometric node, it was appeared to be two trailing vortices then merge into a single structure end in an asymmetric flow pattern rather than the symmetric pattern [9]. Ahmed et al [21] further investigated the flow filed behind the wavy cylinder. Behind the nodal point the formation of trailing streamwise vortices give rise to a locally narrower wake, a rapid wake velocity suppression and recovery of the turbulence development within the separated boundary layer. Reynolds stress behind the geometric saddles was higher than the geometric nodes; it can be attributed to (a) higher level of shear-layer turbulence contained behind the saddles separated boundary layers (b) the Karman vortex behind the saddles have greater total circulation since behind the nodes due to the streamwise vortices, some of the vorticity of the separated boundary layer entrained (c) In von Karman formation region all Reynolds stress values is large, due to the dynamics of the vortex rolling up and tearing away , the wake behind the saddle is larger than node, therefore the Reynolds stress may higher. Owen [26] also investigated flow over the sinuous wavy bluff body by using flow visualization. The results show the flow behind the sinuous wavy bluff body is quite different between the circular cylinders, and found the Karman vortex shedding was suppressed and the drag is substantial reductions. Keser [28] investigated a circular cylinder with sinusoidal waviness along the spanwise direction by numerical methods (figure 10). The simulation indicated when increase the wave steepnesses from 0.125 to 0.14 the shedding is not suppressed, but the large scale vortices from the separated boundary layers was delayed for longer time.

Lam [11] studied the lift and drag reduction effect on the different wavy cylinders and the related effects on flow induced vibration. By changing the geometric wavy amplitude and wavelength of the wavy cylinder, it was expected that such type of cylinder could get a better control vortex shedding and suppression of FIV. Cylinder with a constant value of wave amplitude, they found the value of wavelength ratio from 1.45 to 2.27 at Reynolds number ranges of 20,000 to 50,000, the maximum drag reduction up to 20 %. It was also found that the wavy cylinders root-mean-square fluctuating lift coefficient are lower than the circular cylinder, but the hot-wire and load cell signals show that the Strouhal numbers of wavy cylinder are mostly same as a corresponding straight cylinder. Furthermore, Lam [12] studied the near wake velocity distributions of a wavy cylinder. They found the average vortex formation length behind the wavy cylinder was longer than circular cylinder and point out a relation between the elongated vortex formation and vibration suppression and drag reduction. Moreover, the vortex formation length on the geometric saddle has a longer formation region and rapid reverse flow, the rib-like structure found near the saddle plane at Re = 600; also they found the cylinder with the wavy geometry play a crucial role in drag

reduction and vortex formation length and vortex shedding suppression. Zhang [6] using the particle image velocimetry (PIV) technique to measurement the three-dimensional near wake structures behind a wavy cylinder at Reynolds number of 3,000. The streamwise vortices with alternating positive and negative were observed along the spanwise direction were well organized. They suppress the formation of the large-scale spanwise vortices and regular vortex shedding and reduce the overall turbulent kinetic energy in the near wake of wavy cylinder. Lee and Nguyen [7] conducted experiments in the range of Reynolds numbers from 5,300 to 50,000 and tested two sinusoidal models with wavelength to diameter ratios $\lambda/D = 1$ and $\lambda/D = 2$. The results compared to the straight cylinder showed that with a wavy cylinder with $\lambda/D = 2$, a large reduction in drag was achieved. At Re = 10,000 the maximum drag reduction obtained for $\lambda/D = 2$ was 22%. The experimental results indicated that the drag reduction was related to the reduction of vortex formation length behind a wavy cylinder. Lam and Lin [8] investigated the effect by different wavelength and amplitude at Reynolds number 100 and 3,000 using numerical methods. At Re = 100, the optimal wavelength ratios $2.5 \leq \lambda/D \leq 6$ and amplitudes ratio $0.05 \leq a/D \leq 0.225$ showed the maximum drag reduction approximate of 18%, moreover, the R.M.S lift coefficient were significantly reduced to nearly zero. Lin [29] investigated the flow around the sinusoidal wavy cylinder at Re = 3,000 and showed that the wavy surface leads to form of 3-D free shear layer, and the vortex formation elongated downstream to a value larger than the straight cylinder. Therefore, the sinusoidal wavy cylinders mean drag coefficient remained smaller than the corresponding straight cylinder.

1.5 Objectives

Two-dimensional flow over the straight cylinder has been studied for many years. However, most of the complex flow phenomena are three-dimensional. Thus, in recent years studies have been aimed towards work on the three-dimensional flow due to the available computational tools. In the recent years different types of cylinders with sinusoidal surfaces along the spanwise direction, called wavy cylinders, were introduced. Over the past years Ahmed and Bay-Muchmore [9], Ahmed et al [21], Tombazis and Bearman [23], Bearman and Owen, Owen and Szewczyk [26], Darker and Sherwin [25], Keser [28], Lam et al [11][12], Zhang et al [6], Lee and Nguyen [7], Lam and Lin [8], studied the several types of wavy cylinders either using experimental methods or numerical methods. These methods have been proven effective to control the flow-induced vibration and reduced mean drag

fluctuation. The present research focuses on the range of the Reynolds number from 10,000 to 20,000 on the subcritical flow regime.

The information available by using three-dimensional PIV measurements of wavy cylinders in the literature is limited. Therefore, this research is using three-dimensional PIV measurements the wake behind the wavy cylinder to obtain a deeper understanding of the wavy cylinder flow characteristic. By using passive flow modification using three different wavelength models to alter the flow characteristics in the wake and compare them to the wake of straight cylinder. Furthermore, analyze the wake data using the POD methods to determine the energy distribution of the coherent structure in the wake.

Chapter 2
Experimental Setup

Wavy cylinders of three different wavelengths were used. The wavy cylinder was made from aluminum and protected by a coating of black enamel. The axial maximum diameter locations of the wavy cylinder are termed “nodes,” and the axial minimum diameter locations are termed “saddles”. The bottom of each wavy cylinder (the lowest 0.8 inch) is slightly different, and the tops were ended smoothly near a geometric node. The geometry of the wavy cylinder is shown in Figure 2.1. The geometry of the wavy cylinders used in the experiment are described by the following equation:

$$R_{local} = R_{mean} - A\cos(2\pi Z/\lambda) \quad (1)$$

Where R_{local} is the local diameter and R_{mean} is the mean diameter, in this case, 1.25 inch. *A* is the wavy cylinder surface amplitude and is 0.25 inch. The length of the wavy cylinder (Z) is 24 inch.

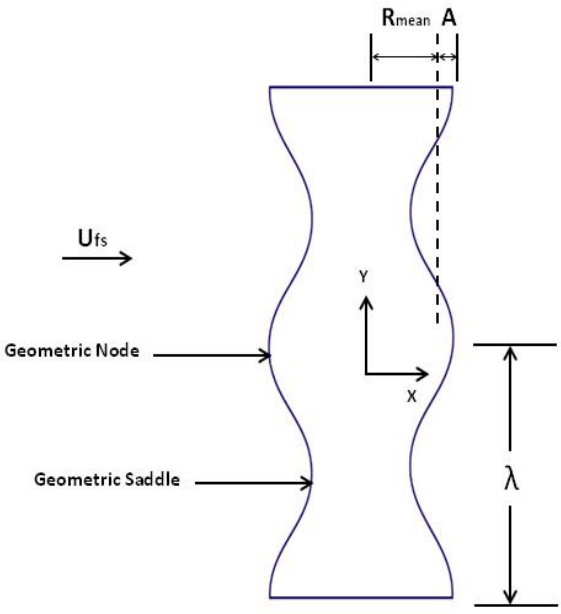

Figure 2.1: Coordinate system and terminology of the wavy cylinder.

Wavy cylinder	Model 1	Model 2	Model 3
The Minimum diameter D_{min} (inch)	2	2	2
The Maximum diameter D_{max} (inch)	3	3	3
Mean diameter D_{mean} (inch)	2.5	2.5	2.5
Wavelength/mean diameter (λ/D_{mean})	1.2	1.6	2.4
Amplitude (A)	0.25	0.25	0.25

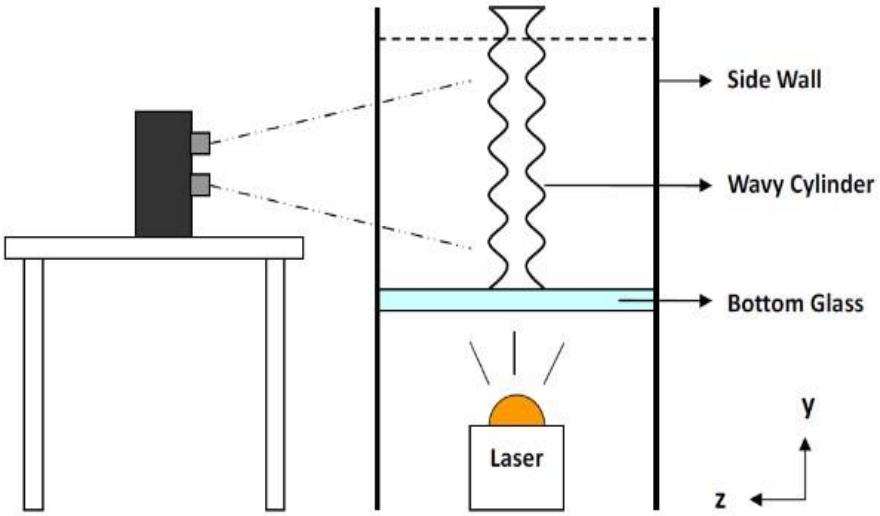

Figure 2.2: End view of the experiment setup

2.1 Description of water Tunnel

The experiments were conducted in the Tuskegee University water tunnel at two freestream velocities of 0.23 m/s and 0.31 m/s (Reynolds numbers of 15,000 and 20,000). The test section of the water tunnel is 15 inches wide, 20 inches deep and 60 inches long. The wavy cylinder was mounted vertically in the test section. A TSI Inc. three-dimensional Particle Image Velocimetry (PIV) V3V system consisting of three 4 mega-pixel image sensors arranged in a coplanar triangle pattern and pre-aligned to view a volumetric domain of 140×140×100 mm^3 was used for the research. The camera recorded 1,000 pairs of images from each three camera to generate the statistics.

2.2 Detail of V3V PIV

The Particle Image Velocimetry (PIV) is use Volumetric 3-component Velocimetry systems (V3V) made by TSI. It is double-frame double-exposure and three-dimensional three component (3D3C) systems. An Nd: YAG laser was used to illuminate the measured volume region. Determination of the flow velocity is based on measured individual particle displacements in the time between laser pulses and information from each aperture to obtain the location three-dimensional of the particles. Furthermore, the system is based on the Defocusing Digital Particle Image Velocimetry (DDPIV) and the optimized seed density per frame is between 50,000 and 100,000.

An Evergreen Quantel Twin model YAG200-15-QTL Nd: YAG laser was used to provide the volumetric illumination. The laser light beam was passed through two lenses to increase the light width. Using a pulse generator, the pulse repetition rate could be manipulated from 0 to 15 Hz at an energy level of 200 mJ per pulse.

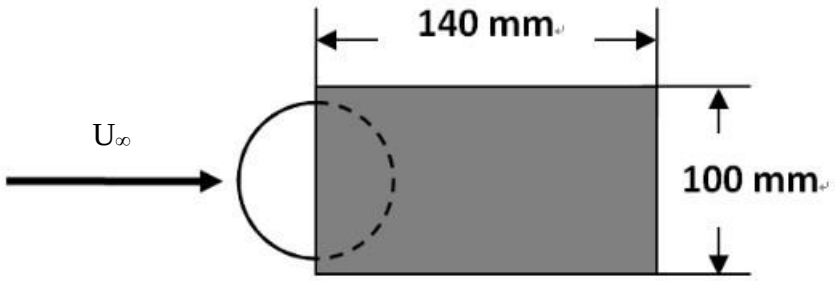

Figure 2.3: The field of laser illumination.

The images were captured using a model 630059 Powerview Plus series high-resolution CCD camera with a Nikon 50mm lens and fixed aperture of f16. The camera was designed to capture the particles' images from the illuminated flow field. The 630059 Model has a 2048×2408 array of light-sensitive pixels, each having a diameter of 7.4×7.4 μm. The frame rate of the CCD quantum was 16 frames/second. Moreover, the cameras were pre-aligned to view a volumetric domain of 140-height ×140-width ×100-depth mm^3, array in a coplanar triangle pattern. The distance between the water wall and camera was approximately 500 mm.

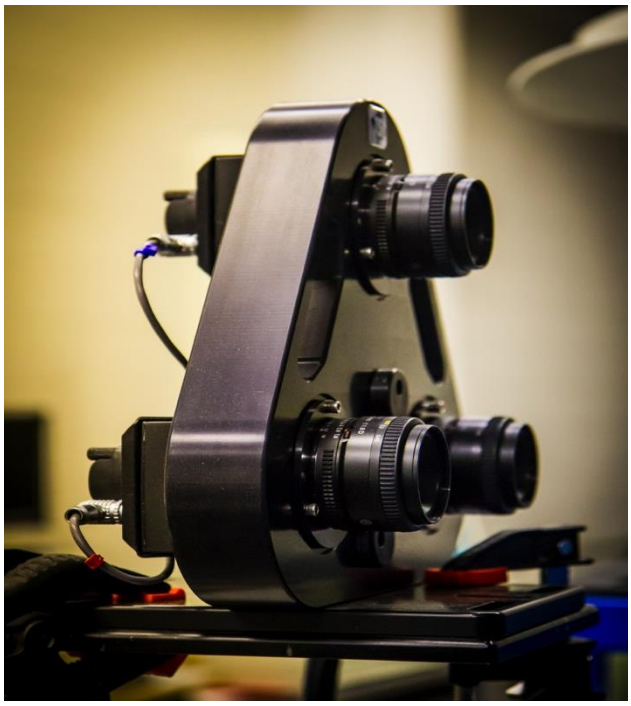

Figure 2.4: V3V camera system.

The Model 610035 synchronizer by TSI was used as an external trigger and connected to the laser and the PIV camera to control the flash lamps and Q-switches. The pulse delay time (delta T) between two frame was set 1,500 μs at Re = 15,000 and 1,100 μs at Re = 20,000. The two-frame double exposure was set at a 7.25 Hz capture rate.

The traverse system has 500 mm of travel and the lead screw each pitch is 1 mm per revolution. The traverse system was used during the calibration processes to move the calibration target to multiple depth positions.

The calibration target consisted of a 200×200 mm plate with precise grid of 5 mm vertical and horizontal spacing. The calibration target traversed 5mm in each plane in the spatial direction through the entire measurement volume. After the calibration process, the system showed the calibration graph that contained the camera signature, dewarping error, magnification and pinhole comparison information. Only the calibrations with the dewarping error value of less than 0.25 pixels were used. A calibration graph is show in Appendix C.

The model 10090-particle seeds by TSI were used. The average size of the polycrystalline particles was 55 μm, a density of 1.016G/CC and the refractive index of 1.52. Data was processed using the TSI software. Use two frames to tracking the particle and form the 3D flow field. The detail of the process procedure is shown in the Appendix D.

2.3 Timing setup

The timing setup is to set the parameters to capture the better image. In this experiment, the frame mode is set to the straddle mode to acquire two consecutive single exposure images. The pulse repeat rate (Hz) values are 7.25 Hz. In order to obtain the good 3D flow result, the optimized X-Y displacement is around 4~6 pixels. Hence, exposure time and laser pulse delay time is setting at 1100 and 1500 for Re = 20,000 and Re = 15,000. Delta T is to determine the pulse separation and is critical to set the proper value to matching the flow velocity.

2.4 Description of Proper Orthogonal Decomposition

The Proper Orthogonal Decomposition (POD) is a technique that uses mathematical methods to extract the coherent structure from turbulent flows and is very useful to describe the complex flow field with a low-dimensional model. There are two methods of POD: the classic POD and the snapshot POD. Using the toolbox in the Insight 4G software by TSI, a snapshot method was applied to calculate the eigenfuctions from the cross-correlation matrix. Two-dimensional slices of the flow at geometric nodes and saddles in the X-Z plane were analyzed to obtain the detail of the wake behind the wavy cylinder. Slices were taken on Y/D = 0 in X-Z plane on straight cylinder. The method of snapshots first arranged the sequence of

snapshots part of velocity data using the equation 2, where N is the number of snapshots (N = 1,000).

$$V_1^N = \{v_1, v_2, v_3 \dots \dots v_N\} \tag{2}$$

And then formed the matrix below

$$C = \frac{1}{N} V_1^N (V_1^N)^H \tag{3}$$

The equation below solves the eigenvalue problem then arranges the sloution by eigenvalue.

$$C\phi_j = \lambda_j \phi_j \tag{4}$$

Then the POD modes can be found from equation 5 by multiplying corresponding eigenvalues by each image and sum to get modes.

$$\alpha = \frac{\sum_{j=1}^{N} \phi_n v_N}{\left\| \sum_{j=1}^{N} \phi_n v_N \right\|} \tag{5}$$

The energy distribution decayed exponentially across the POD, and the energy above mode five was extremely small relative to mode one. Hence, the first mode or the highest energy mode can be regarded as a “dominant” flow characteristic and contains the most kinetic energy.

Chapter 3
Results and Discussion

The results compare three different wavy cylinder models to a straight cylinder and show the vorticity, velocity and Proper Orthogonal Decomposition (POD) in different planes. The velocity contour and vorticity contour plots are displayed in the X-Y plane (front view), X-Z plane (top view) and Y-Z plane (end view). Furthermore, the Proper Orthogonal Decomposition (POD) shows the vorticity contour from mode one to mode 25 and the energy distribution plots. The wavy cylinder and straight cylinder are located at the field of view of the right side and the flow direction is from right to the left.

3.1 Mean velocity

Contour plots of time averaged velocity are given in Figures 3.1 to Figure 3.14 for Reynolds number at 15,000 and 20,000. High magnitudes of velocity are colored red and low magnitudes of velocity are blue. The mean velocities were non-dimensionalized by the free stream velocity.

For straight cylinder contours, Figure 3.1a and Figure 3.8a show that at the Re = 15,000 and the Re = 20,000, the entire region is approximately a straight line with no distortion form one Karman vortex shedding cycle to the next and parallel to the straight cylinder axis. For Re = 15,000, the mean velocity displays the minimum and negative value at X/D = 1; this indicates a region of reversed flow. Downstream of X/D = 1, the mean velocity exhibits the gradual increase from a minimum value of -0.01 to approximately 0.18. For the same Reynolds number, the wavy cylinder with wavelength λ/D_{mean} = 1.2, the reverse flow region is located at X/D = 1 behind the geometric saddle and at X/D = 0.8 behind the geometric node. When λ/D_{mean} = 1.6 the reverse flow region moves to X/D = 1.7 behind the geometric saddle and at X/D = 1.5 behind the geometric node. When λ/D_{mean} = 2.4 the reverse flow region is located at X/D = 1.35 behind the geometric saddle and at X/D = 1.2 behind the geometric node. For Re = 20,000 the reverse flow region on wavelength λ/D_{mean} = 1.2, λ/D_{mean} = 1.6 and λ/D_{mean} = 2.4 are located slightly further to the downstream compared to at Re = 15,000.

Furthermore, Figure3.2 and Figure 3.9 contour plots show the near wake structure have sinusoidal shape along the spanwise direction and maintain the sinusoidal shape farther

downstream, and the flow expands behind the wavy cylinder relate to the geometric node and geometric saddle. From the results, it can be deduced that the wavy cylinder separation lines are not uniform and have a three-dimensional vortical structure. Behind the cylinder, the velocity at the geometric saddle at X/D = 0 is higher than the geometric node. Due to the geometric node having the bigger diameter than geometric saddle, it could obstruct from the approaching flow compared with the geometric saddle. Moreover, at the geometric saddle, high-speed flow over it interacts with the adjoining low-speed flow. Hence, the mean velocity falls off drastically near the saddle. The streamwise velocity behind the geometric node is very steep and the wake velocity recovery is more rapid than at the geometric saddle. Figure 3.7 and Figure 3.14 show the contour plane in the end view (YZ-plane) at X/D = 0.3. The plots demonstrate the velocity behind the geometric node is much more rapid than the geometric saddle. Also the streamline shown at the node is narrower than at the saddle. The result disagrees with Zhang [6], who exhibited that the flow over the wavy cylinder has a faster velocity after the geometric saddle than behind the geometric node.

Results presented in Figure 3.4 - 3.6 for Re = 15,000 and Figure 3.11 - 3.13 for Re = 20,000 exhibit the top-view velocity contour at the node plane, saddle plane, and mid-plane. The plot displays that the node plane has a narrower wake while the saddle plane has a wider wake. Due to the flow over the geometric node, the flow separation happens later than at the geometric saddle. Therefore, the entrainment of the main flow and three-dimensional vortex interaction it produces is a wider wake flow field in the saddle plane and a narrower wake flow field in the node plane.

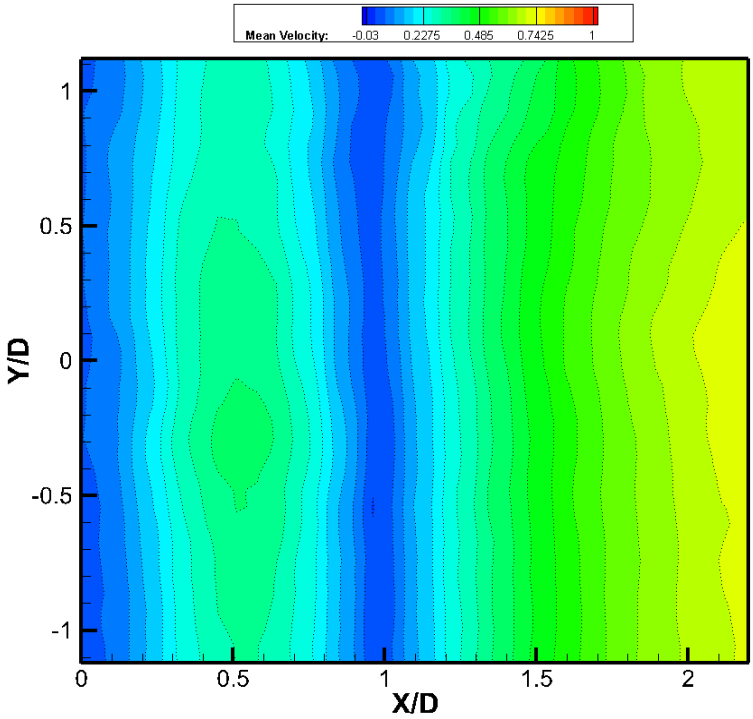

(a)

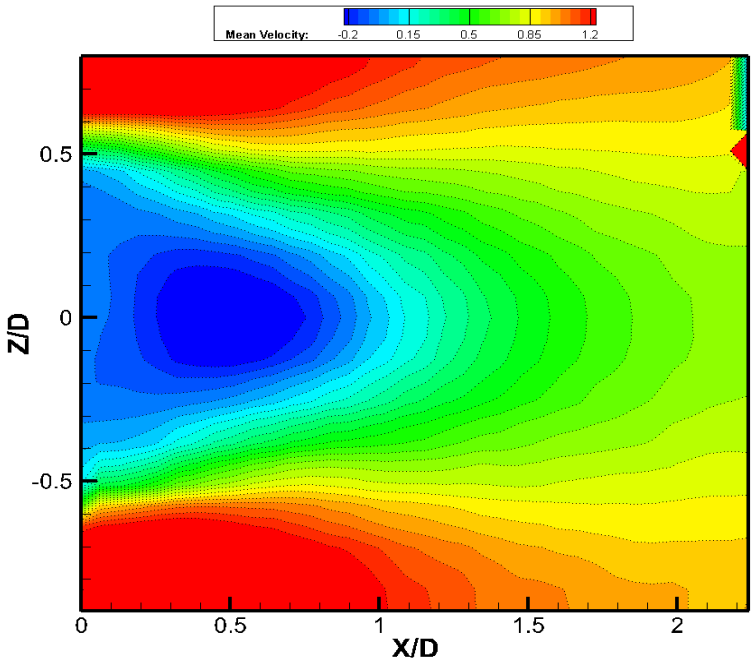

(b)

Figure 3.1: Straight cylinder velocity contour plots at Re = 15,000.
(a) XY plane, centerline (b) XZ plane

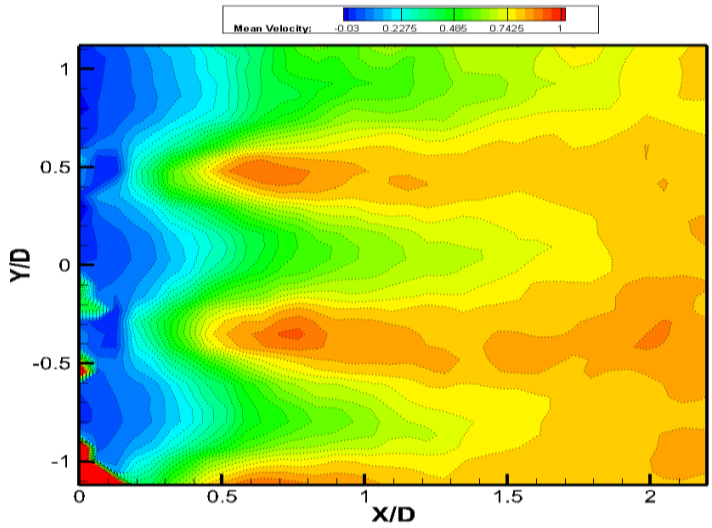

(a) λ/D_{mean} = 1.2

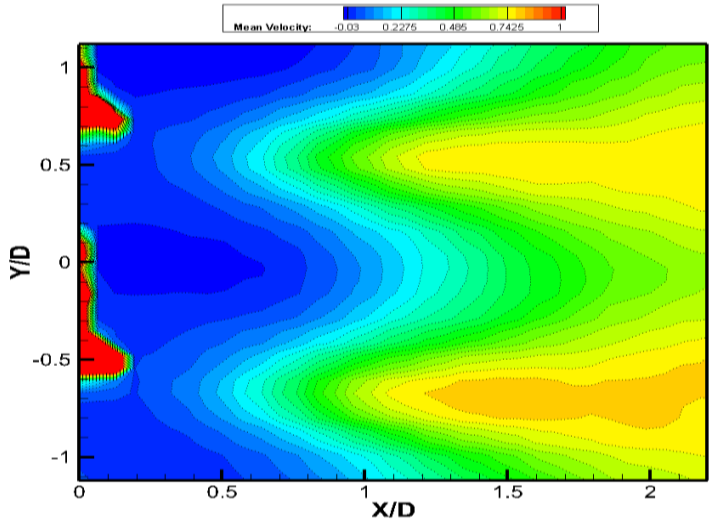

(b) λ/D_{mean} = 1.6

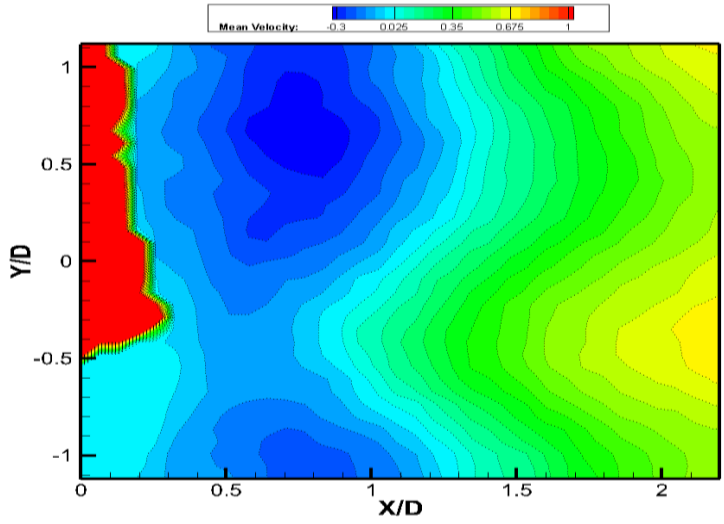

(c) λ/D_{mean} = 2.4

Figure 3.2: Velocity contour plots in the XY plane (Re = 15,000, Z/D = -0.45) (a) λ/D_{mean} = 1.2 (b) λ/D_{mean} = 1.6 (c) λ/D_{mean} = 2.4

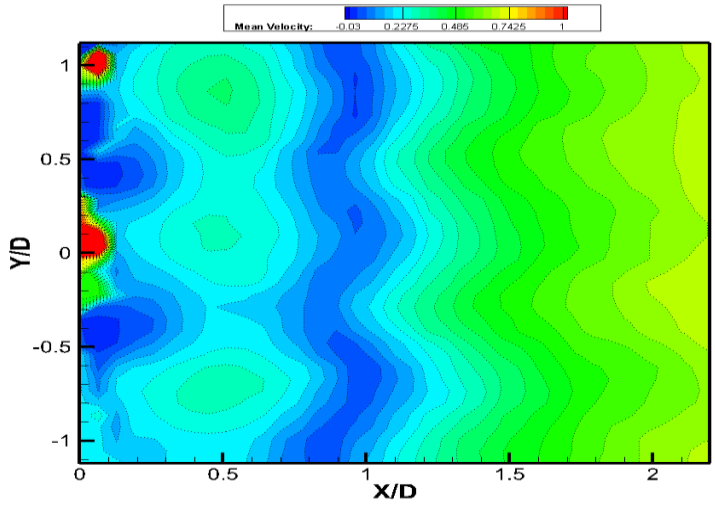

(a) λ/D_{mean} = 1.2

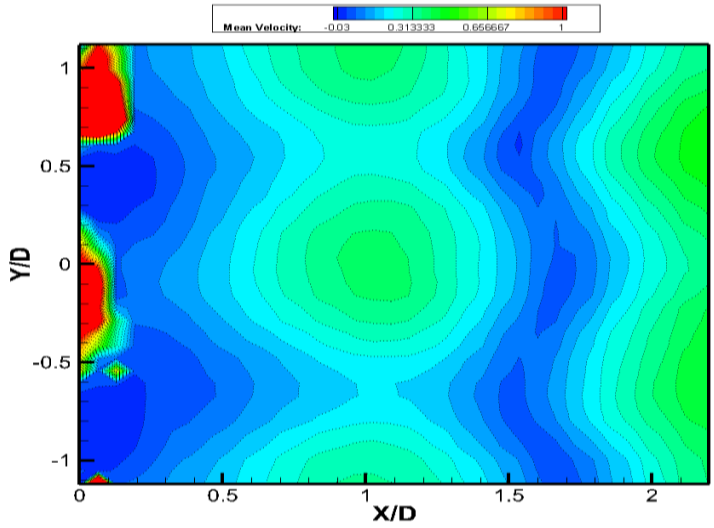

(b) λ/D_{mean} = 1.6

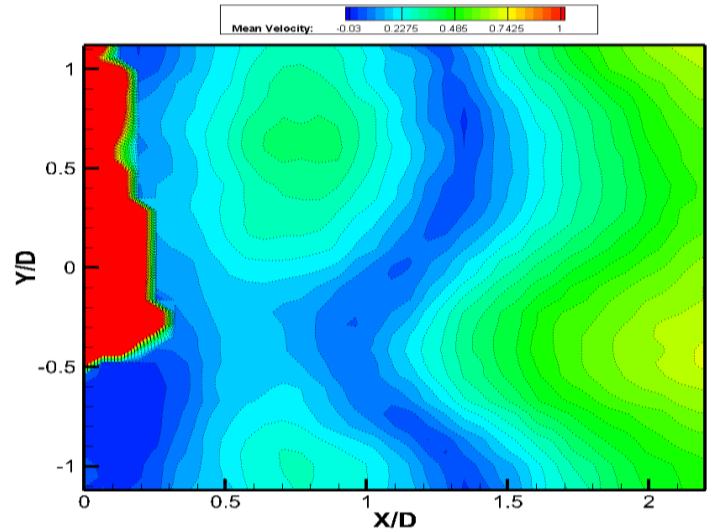

(c) λ/D_{mean} = 2.4

Figure 3.3: Velocity contour plots in the XY plane (Re = 15,000, centerline)
(a) λ/D_{mean} = 1.2 (b) λ/D_{mean} = 1.6 (c) λ/D_{mean} = 2.4

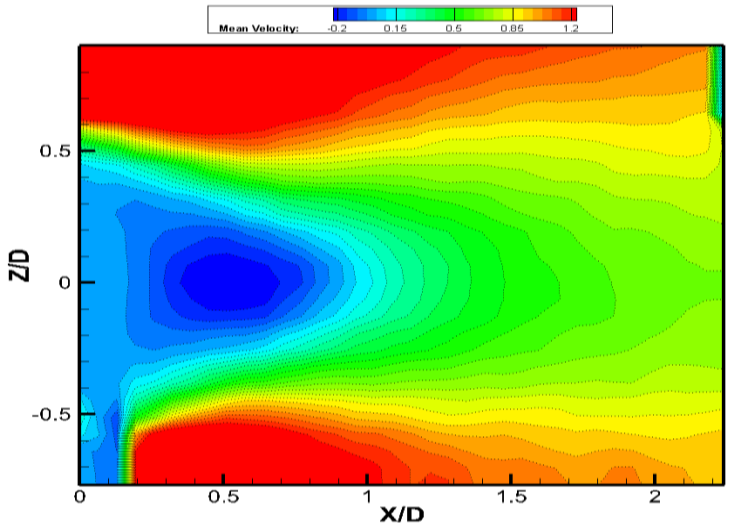

(a) λ/D_{mean} = 1.2

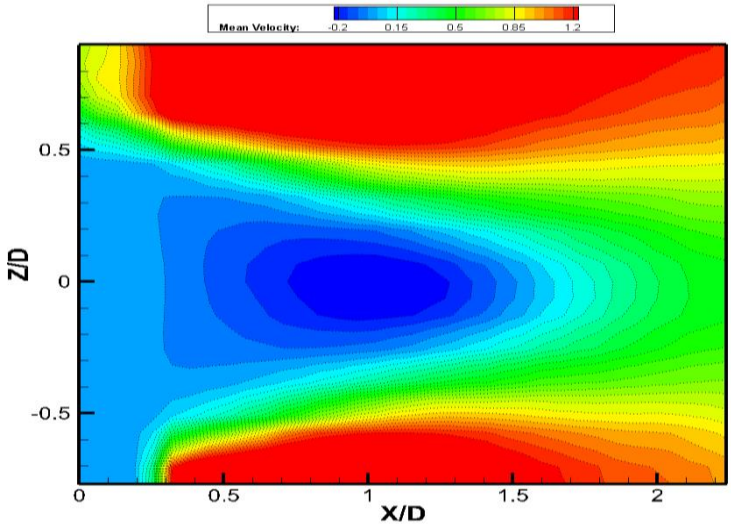

(b) λ/D_{mean} = 1.6

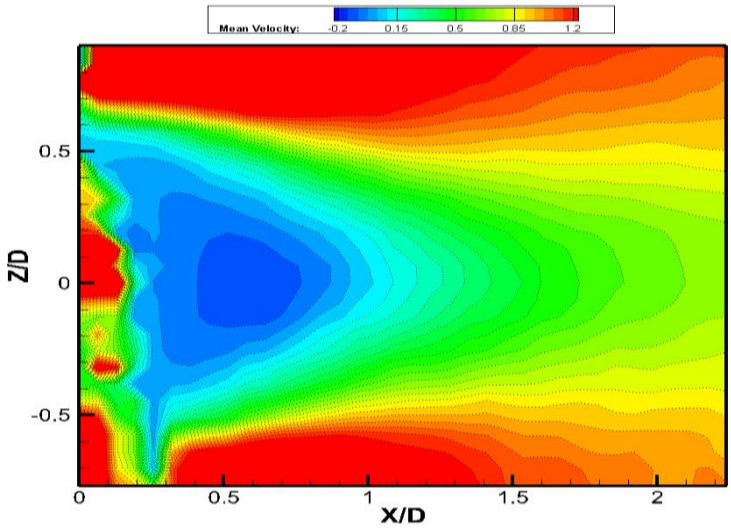

(c) λ/D_{mean} = 2.4

Figure 3.4: Velocity contour plots in the XZ-plane (Re = 15,000, Node plane) (a) λ/D_{mean} = 1.2 (b) λ/D_{mean} = 1.6 (c) λ/D_{mean} = 2.4

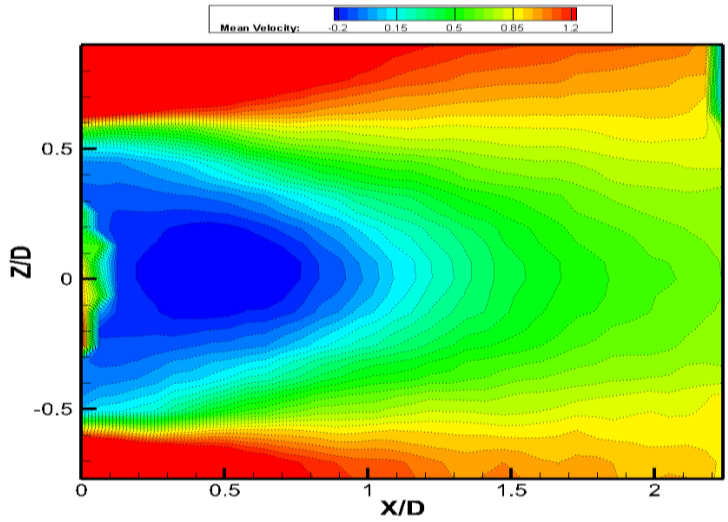

(a) λ/D_{mean} = 1.2

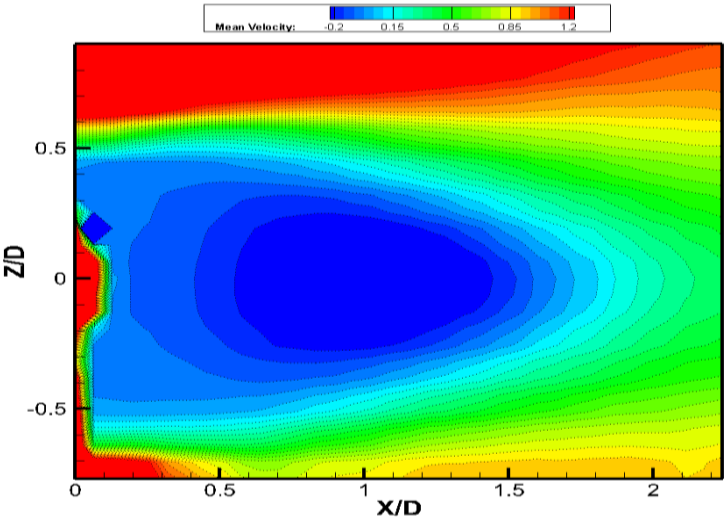

(b) λ/D_{mean} = 1.6

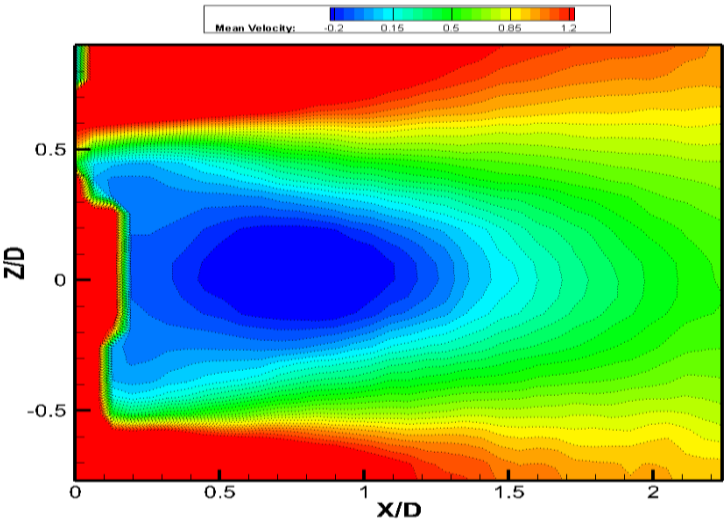

(c) λ/D_{mean} = 2.4

Figure 3.5: Velocity contour plots in the XZ-plane (Re = 15,000, Saddle plane) (a) λ/D_{mean} = 1.2 (b) λ/D_{mean} = 1.6 (c) λ/D_{mean} = 2.4

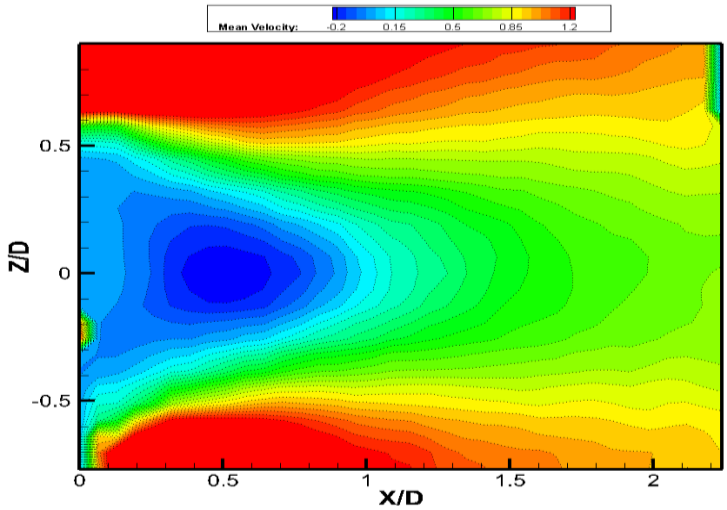

(a) λ/D_{mean} = 1.2

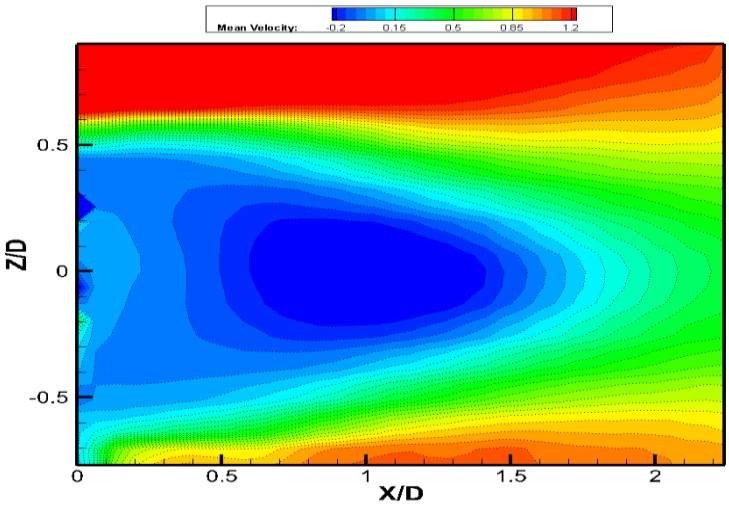

(b) λ/D_{mean} = 1.6

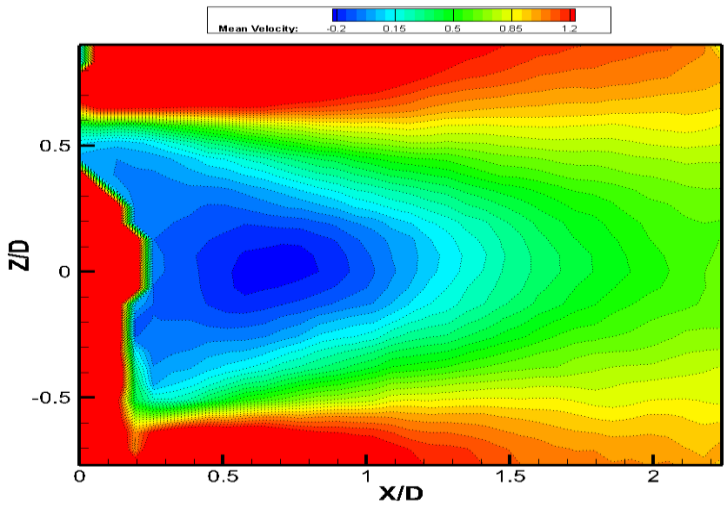

(a) λ/D_{mean} = 2.4

Figure 3.6: Velocity contour plots in the XZ-plane (Re = 15,000, Middle plane) (a) λ/D_{mean} = 1.2 (b) λ/D_{mean} = 1.6 (c) λ/D_{mean} = 2.4

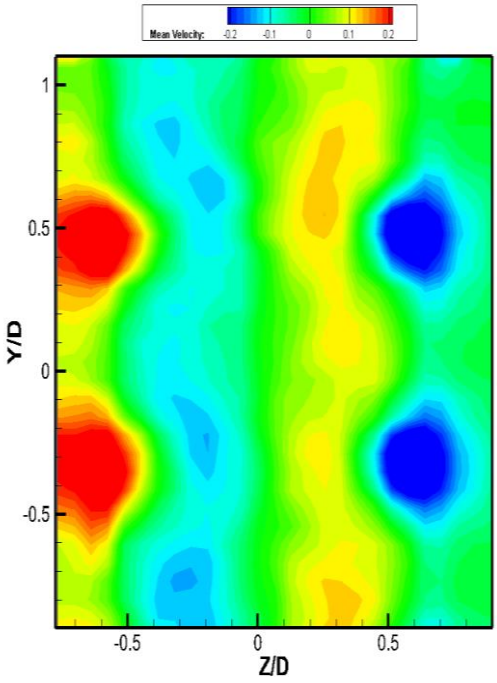

(a) λ/D_{mean} = 1.2

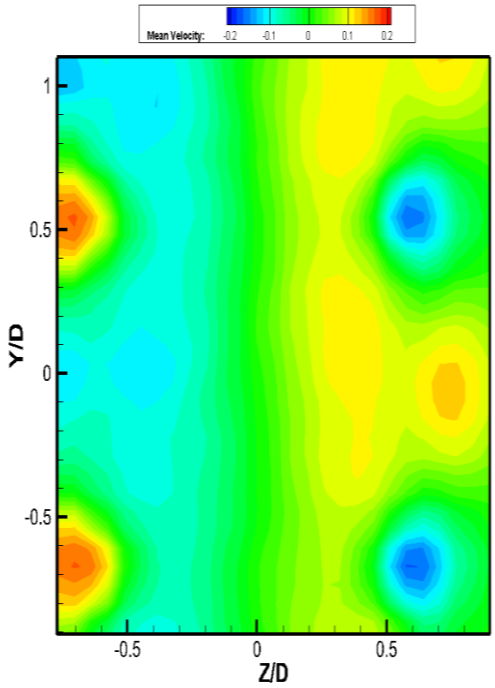

(b) λ/D_{mean} = 1.6

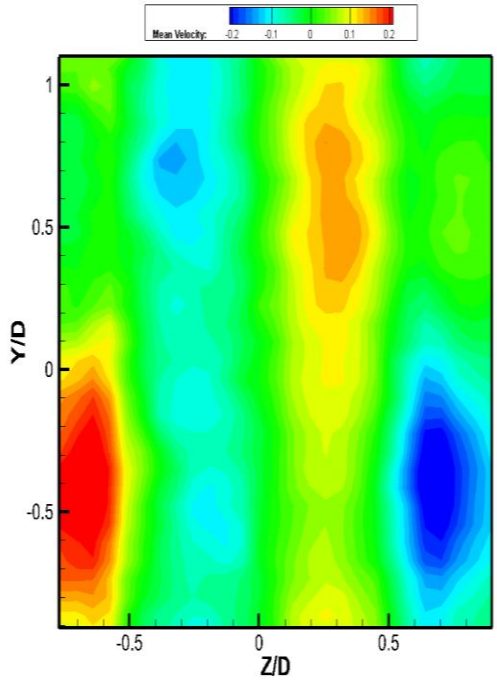

(c) λ/D_{mean} = 2.4

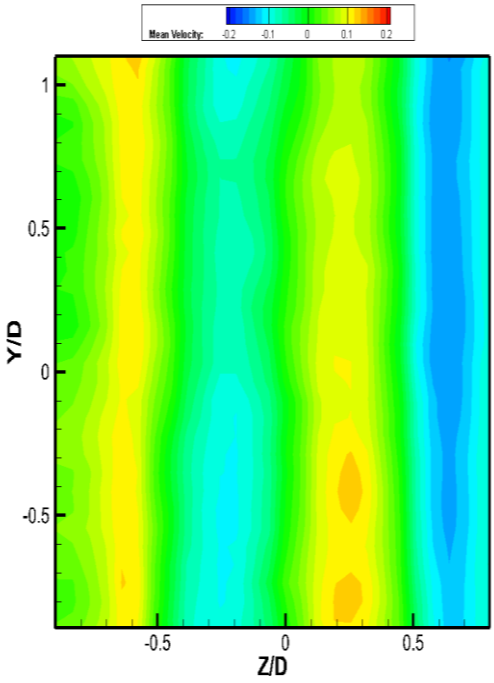

(d) Straight cylinder

Figure 3.7: Velocity contour plots in the YZ-plane (Re = 15,000, X/D = 0.3)
(a) λ/D_{mean} = 1.2 (b) λ/D_{mean} = 1.6 (c) λ/D_{mean} = 2.4 (d) Straight cylinder

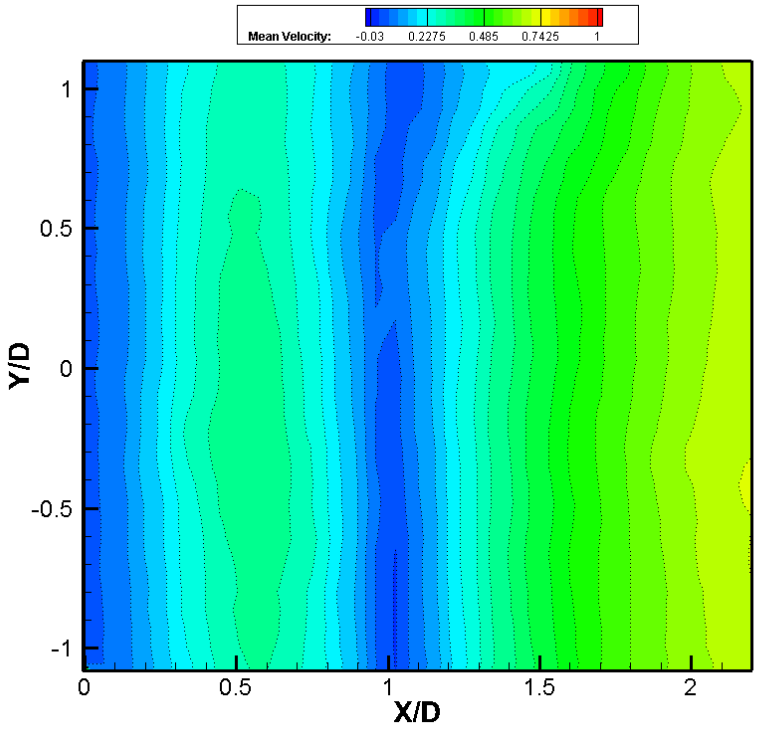

(a)

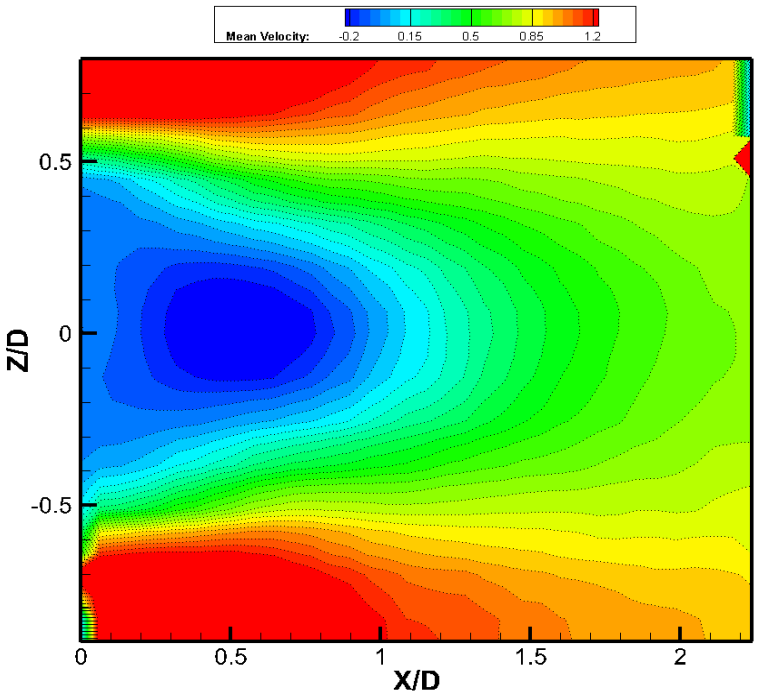

(b)

Figure 3.8: Straight cylinder velocity contour plots at Re = 20,000.
(a) XY plane, centerline (b) XZ plane

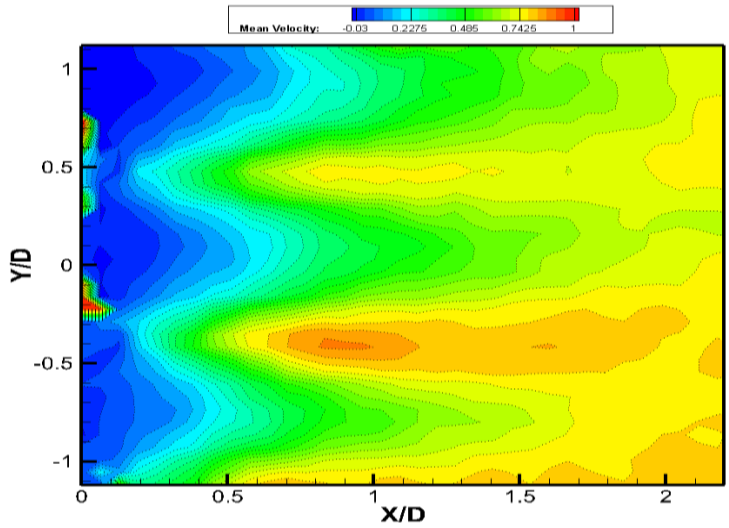

(a) λ/D_{mean} = 1.2

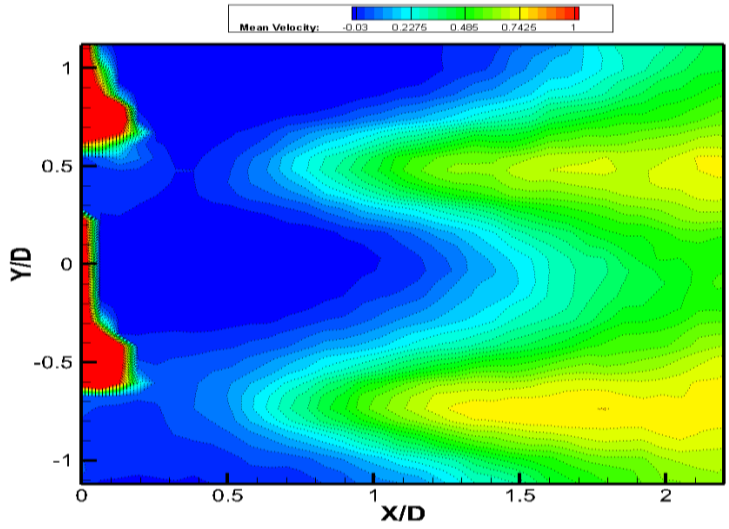

(b) λ/D_{mean} = 1.6

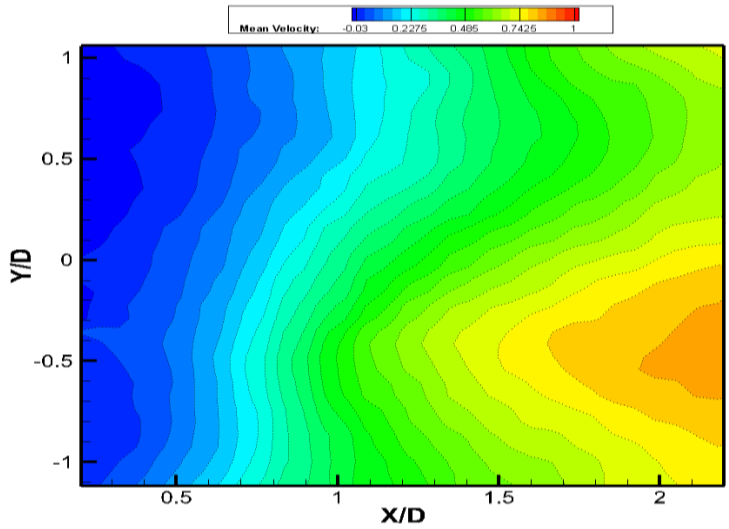

(c) λ/D_{mean} = 2.4

Figure 3.9: Velocity contour plots in the XY-plane (Re = 20,000, Z/D = -0.45) (a) λ/D_{mean} = 1.2 (b) λ/D_{mean} = 1.6 (c) λ/D_{mean} = 2.4

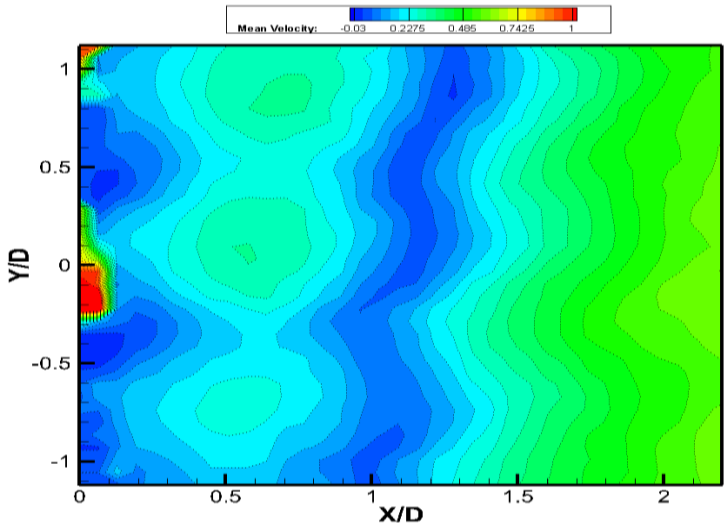

(a) λ/D_{mean} = 1.2

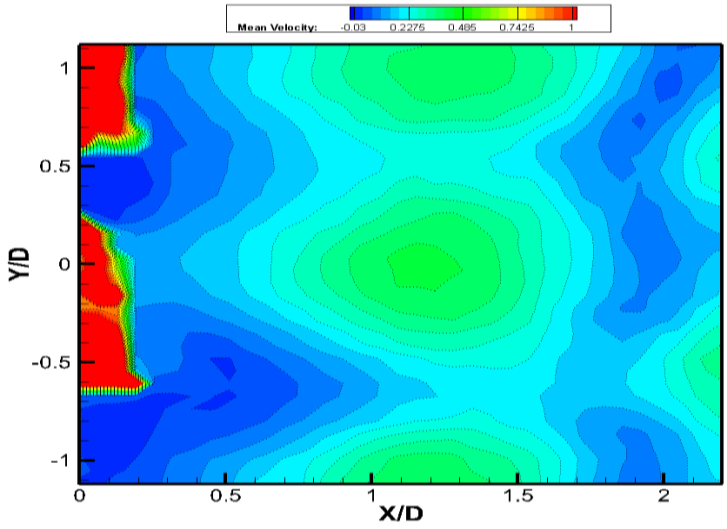

(b) λ/D_{mean} = 1.6

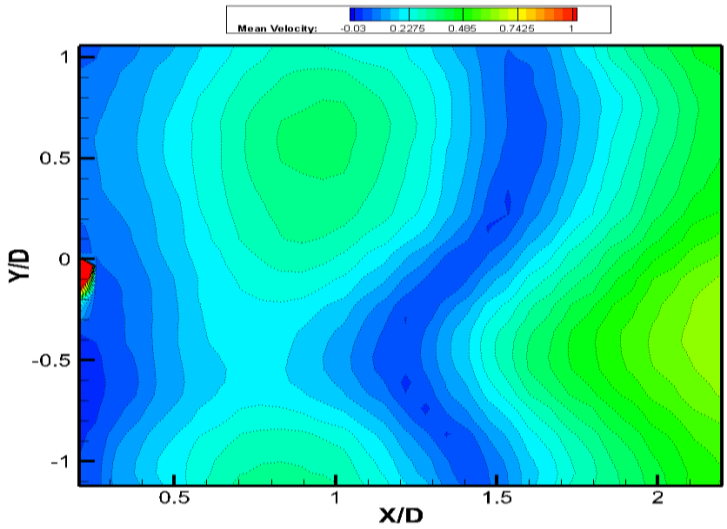

(b) λ/D_{mean} = 2.4

Figure 3.10: Velocity contour plots in the XY-plane (Re = 20,000, centerline) (a) λ/D_{mean} = 1.2 (b) λ/D_{mean} = 1.6 (c) λ/D_{mean} = 2.4

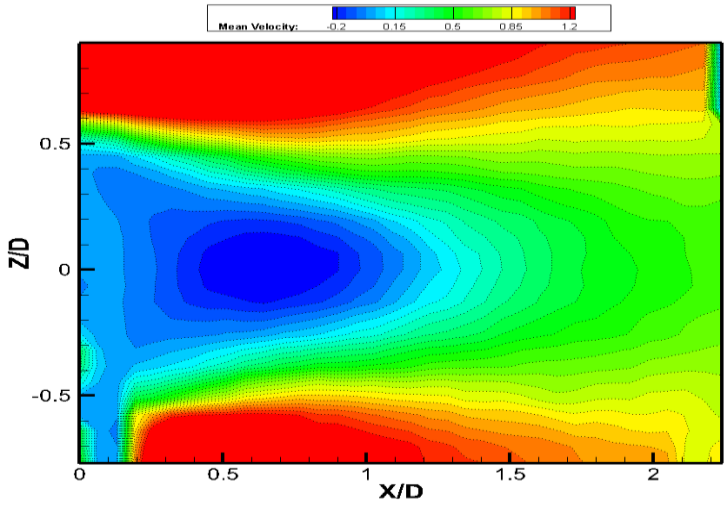

(a) λ/D_{mean} = 1.2

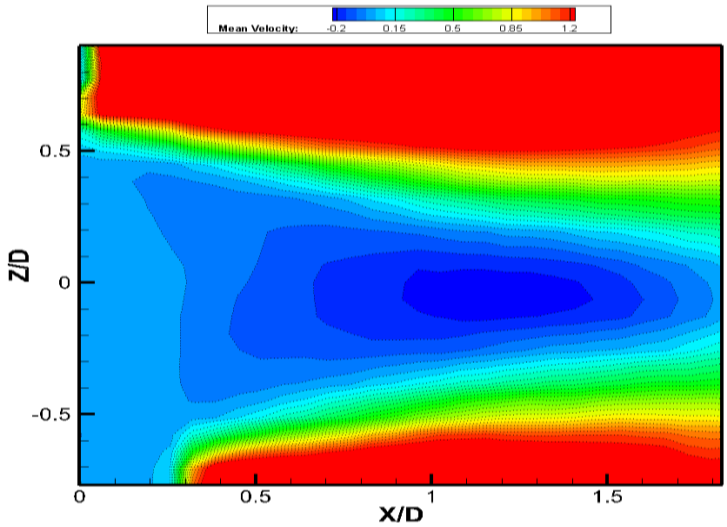

(b) λ/D_{mean} = 1.6

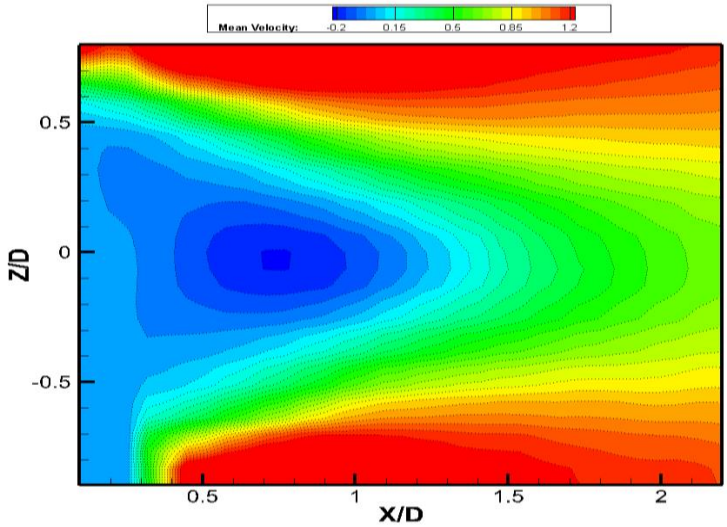

(c) λ/D_{mean} = 2.4

Figure 3.11: Velocity contour plots in the XZ-plane (Re = 20,000, Node plane) (a) λ/D_{mean} = 1.2 (b) λ/D_{mean} = 1.6 (c) λ/D_{mean} = 2.4

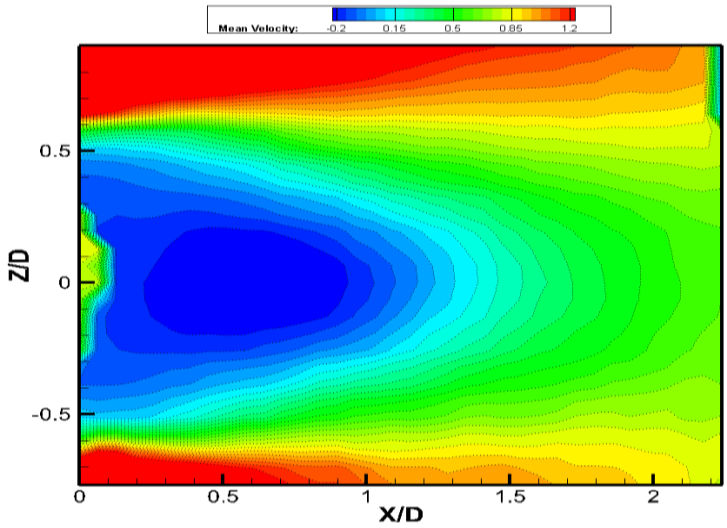

(a) λ/D_{mean} = 1.2

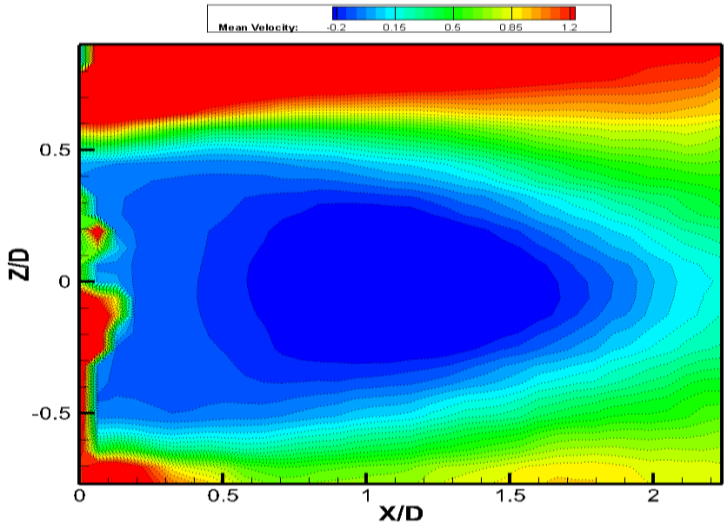

(b) λ/D_{mean} = 1.6

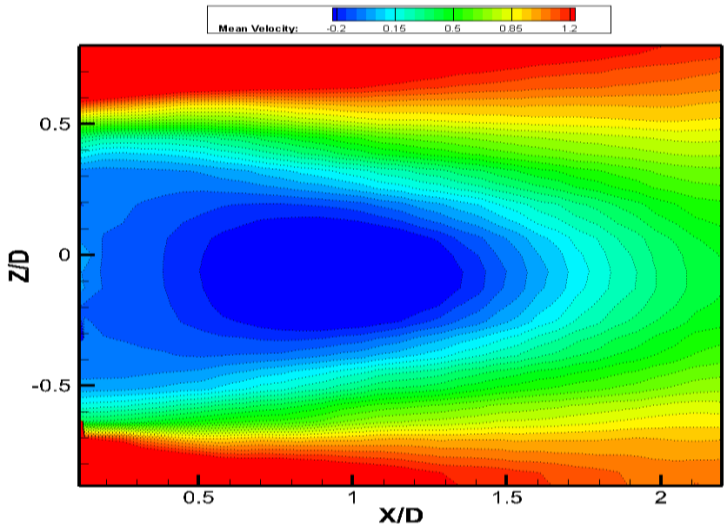

(c) λ/D_{mean} = 2.4

Figure 3.12: Velocity contour plots in the XZ-plane (Re = 20,000, Saddle plane) (a) λ/D_{mean} = 1.2 (b) λ/D_{mean} = 1.6 (c) λ/D_{mean} = 2.4

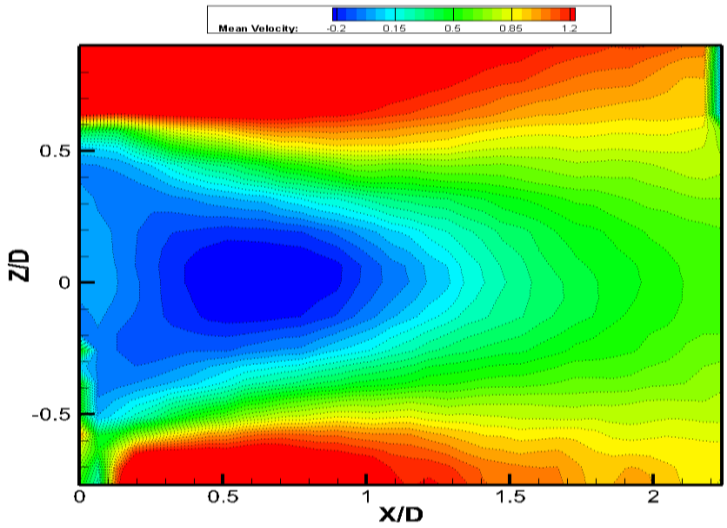

(a) λ/D_{mean} = 1.2

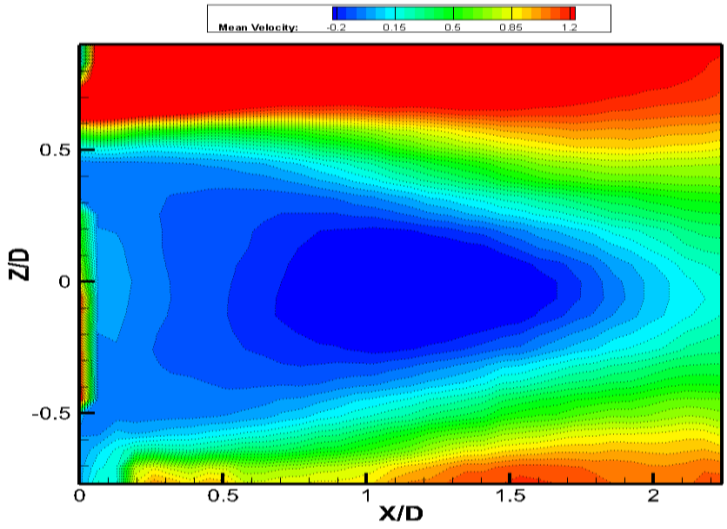

(b) λ/D_{mean} = 1.6

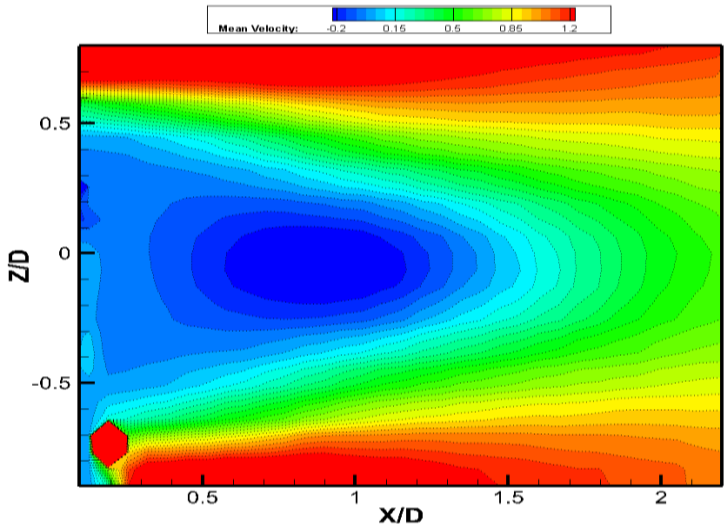

(c) λ/D_{mean} = 2.4

Figure 3.13: Velocity contour plots in the XZ-plane (Re = 20,000, Middle plane) (a) λ/D_{mean} = 1.2 (b) λ/D_{mean} = 1.6 (c) λ/D_{mean} = 2.4

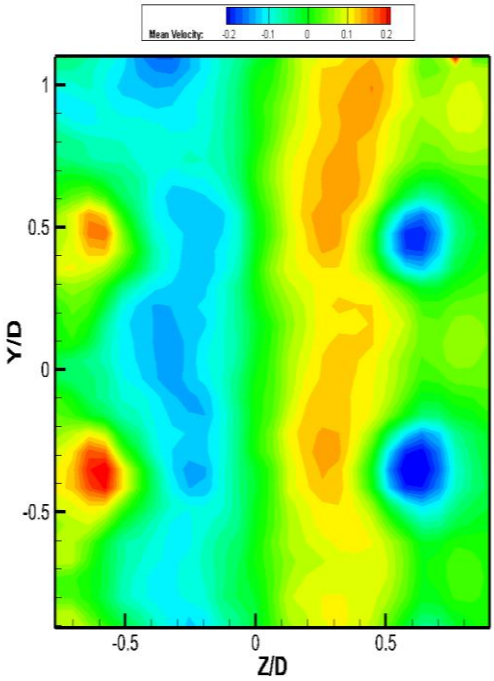

(a) λ/D_{mean} = 1.2

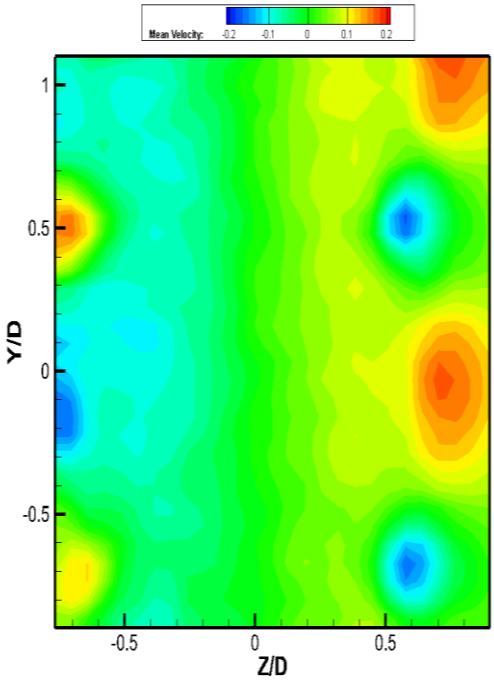

(b) λ/D_{mean} = 1.6

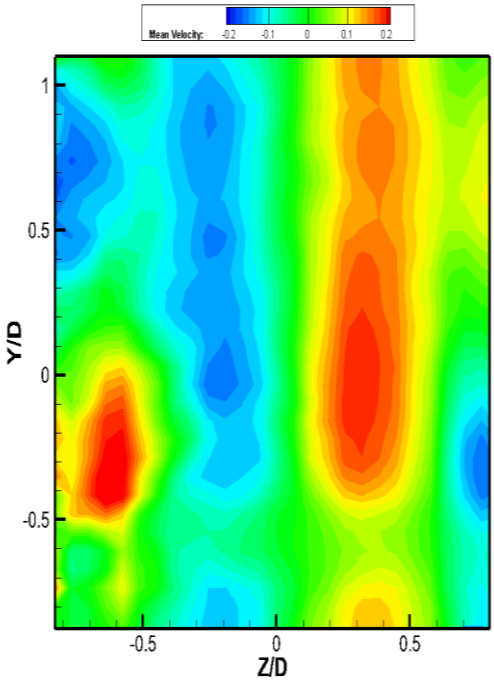

(c) λ/D_{mean} = 2.4

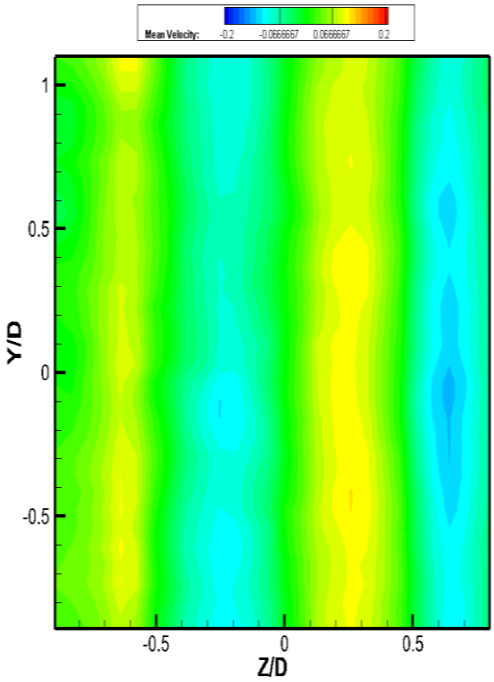

(d)Straight cylinder

Figure 3.14: Velocity contour plots in the YZ-plane (Re = 20,000, X/D = 0.3)
(a) λ/D_{mean} = 1.2 (b) λ/D_{mean} = 1.6 (c) λ/D_{mean} = 2.4 (d) Straight cylinder

3.2 Vorticity

Contour plots of time-average vorticity are given in Figures 3.15 - 3.27 for Re = 15,000 and Re = 20,000. The vorticity was calculated from the following equation:

$$\begin{bmatrix}\omega_x\\ \omega_y\\ \omega_z\end{bmatrix} = \begin{bmatrix}\frac{\partial w}{\partial y} - \frac{\partial v}{\partial z}\\ \frac{\partial u}{\partial z} - \frac{\partial w}{\partial x}\\ \frac{\partial v}{\partial x} - \frac{\partial u}{\partial y}\end{bmatrix} \times \frac{D_{mean}}{U_\infty} \quad (6)$$

3.2.1 Top view (X-Z plane)

Figure 3.15a exhibits the straight cylinder vorticity contour plot in front view at Z/D = 0 at the centerline at Re = 15,000. The flow field did not show a streamwise vortex behind the straight cylinder. This is due to the fact that around the straight cylinder the second vortices in the flow are not located at fixed spanwise positions, even though they are locked spatially in the streamwise direction [6][30]. Hence, in the wake behind the straight cylinder the vortex structure cannot be recognized. Figure 3.15b displays vorticity contour at the top view (X-Z plane). The vorticity was seen to have a maximum value after the straight cylinder along the shear layers on top of the straight cylinder and the bottom. The greatest values occur at X/D = 0 to X/D = 0.4, and begin decreasing at X/D = 0.5 as the vortices travelled downstream. Moreover, At Re = 20,000 as Figure 3.22a shows, the vorticity contour did not show a streamwise vortex behind the straight cylinder. Figure 3.22b shows the greatest vorticity occurs at X/D = 0 to X/D = 0.5 and begins to decay at X/D = 0.6. At X/D = 1.9 the straight cylinder at Re = 20,000 has stronger vortices downstream, in contrast at Re = 15,000 the vorticity was not found on the wavy cylinder.

Figure 3.18 to Figure 3.20 display the vorticity contour plots in the X-Z plane at the node position, saddle position and middle position for Re = 15,000 of the wavy cylinders with the wavelength λ/D_{mean} = 1.2, λ/D_{mean} = 1.6 and λ/D_{mean} = 2.4 in. Figures 3.25 to 3.27 show the velocity contours at for Re = 20,000. Figure 3.18 displays the flow over the geometric node at Re = 15,000. Along the shear layer the vorticity has the highest value on the top and the

bottome of the straight cylinder. For the wavy cylinder with wavelength λ/D_{mean} = 1.2, the lowest vorticity value behind the geometric node, for λ/D_{mean} = 1.6 the vorticity exhibits the greatest value and travelled farther along the downstream compared to λ/D_{mean} = 1.2 and λ/D_{mean} = 2.4. This indicated the vortex formation length behind the λ/D_{mean} = 1.6 wavy cylinder is longer. Moreover, all three models displays the narrower wake behind the geometric node, this is due to the fact that separation location on the geometric node is later than the geometric saddle. For Re = 20,000 in Figure 3.25 the λ/D_{mean} = 1.6 also reveals the greatest vorticity value behind the geometric node and travelled farter downstream. This indicated the free shear layer separated from the wavy cylinder and travelled farther downstream, then made the three dimensional redistribution of vortex occur to be stable; moreover, the free shear layer behind the near wake of the wavy cylinder will not interact. Therefore, suppress the formation of Karman vortex. In Figure 3.19 and Figure 3.26 at Re = 15,000 and Re = 20,000, both figures display the wake behind the geometric has a wider wake compared to the geometric node due to the separation occurring earlier. Spanwise vortices at the three different wavelength cylinders have a greater value than straight cylinder, either in geometric node or geometric saddle at Re = 15,000 and Re = 20,000.

3.2.2 Front view (X-Y plane) and End View (Y-Z plane)

Figures 3.16 and 3.23 display the front view (XY-plane) of the surface of the wavy cylinder (Z/D = -0.45) at Re = 15,000 and Re = 20,000. The vorticity appears at location X/D = 0 to X/D = 0.2 above the geometric node, due to the high shear adjacent flow entrainment than forward to the geometric node. Moreover, behind the geometric node the streamwise vortices (secondary vortices or ribs) occur., This is attributed to the separation which happened at the geometric saddle and the boundary layer rolling up, and the formation the streamwise vortices structurally close to the geometric node. At the wavelength λ/D_{mean} = 1.2, the streamwise vortices developed immediately behind the geometric node. In contrast, at the wavelength λ/D_{mean} = 1.6, the streamwise vortices developed further downstream. As a result, the streamwise vortices are strengthened downstream, and the spanwise vortex development is suppressed or delayed behind the geometric node, and the wake width is affected by the separated boundary layer (shown in Figure s3.18 and 3.25).

Figures 3.21 and 3.28 exhibit the end view (YZ plane) with the wavelength λ/D_{mean} = 1.2, λ/D_{mean} = 1.6 and λ/D_{mean} = 2.4 at Re = 15,000 and Re = 20,000. The vorticity contour plots clearly display pairs of counter-rotating vortices with positive and negative streamwise vortices behind the geometric node at the wavelength λ/D_{mean} = 1.2 and λ/D_{mean} = 1.6. In

contrast, at the wavelength λ/D_{mean} = 2.4 it only reveals the single streamwise vortex at the top of the geometric node and the bottom. This vorticity distribution agrees with the result in the XY plane shown in Figure 3.16 and Figure 3.23. This indicates the separated boundary layer developed by the streamwise vortices, and at the suppression of large-scale vortices at geometric nodes. Furthermore, the spanwise spacing of pairs of streamwise vortices behind the geometric node (shown in Figure3.21a, b and Figure 3.28a, b) did not correlate to the wavy cylinder geometries. For Re = 15,000 and Re = 20,000 Figure 3.21 and Figure 3.28 display at the X/D= 0.3 the wavelength is λ/D_{mean} = 2.4 have the greatest vorticity value behind the geometric node than the wavelength λ/D_{mean} = 1.2, than the wavelength λ/D_{mean} = 1.6. This is due to the streamwise vortices formed near the geometric node at wavelength λ/D_{mean} = 1.2 and λ/D_{mean} = 2.4, and the streamwise vortices formed the further downstream at the wavelength λ/D_{mean} = 1.6. Appendix E exhibits the three-dimensional flow field.

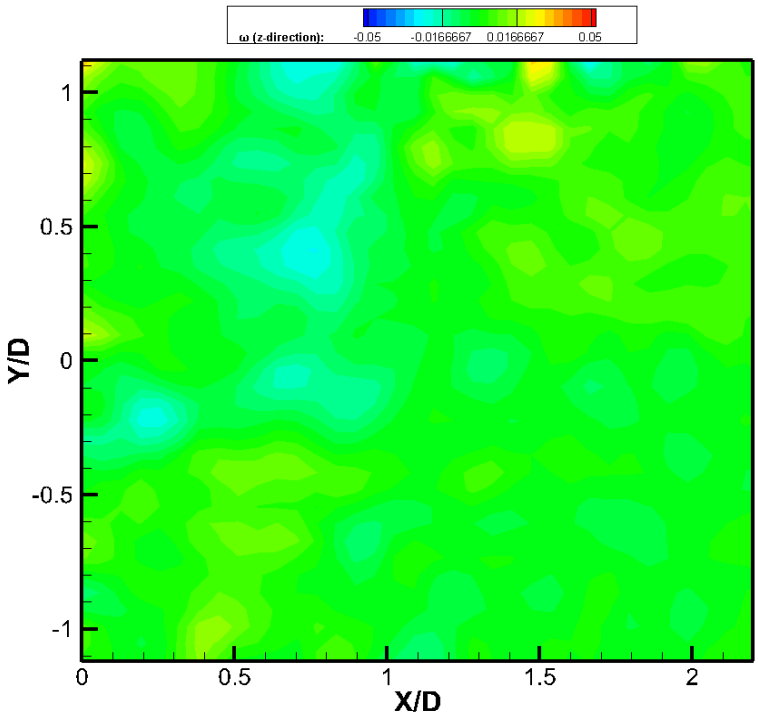

(a)

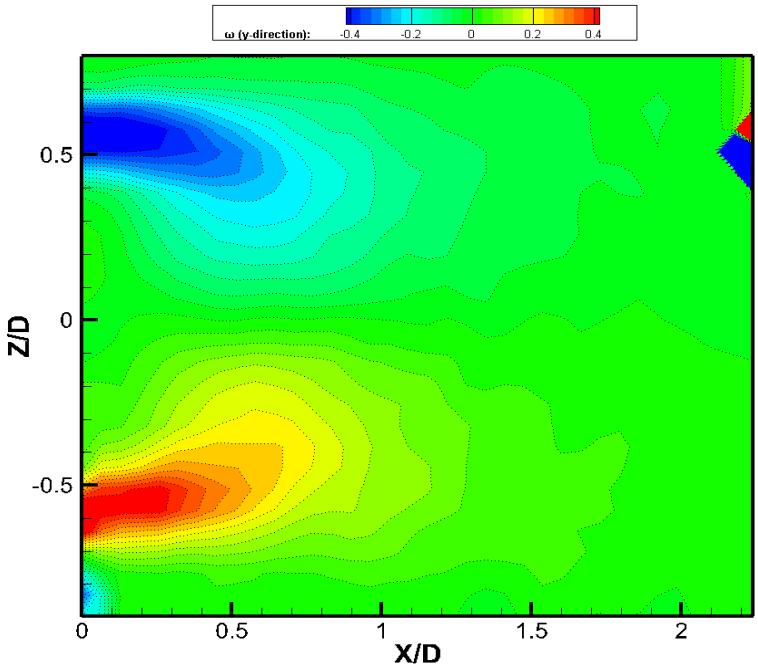

(b)

Figure 3.15: Straight cylinder vorticity contour plots at Re = 15,000.
(a) XY plane, Z/D = 0 (b) XZ plane

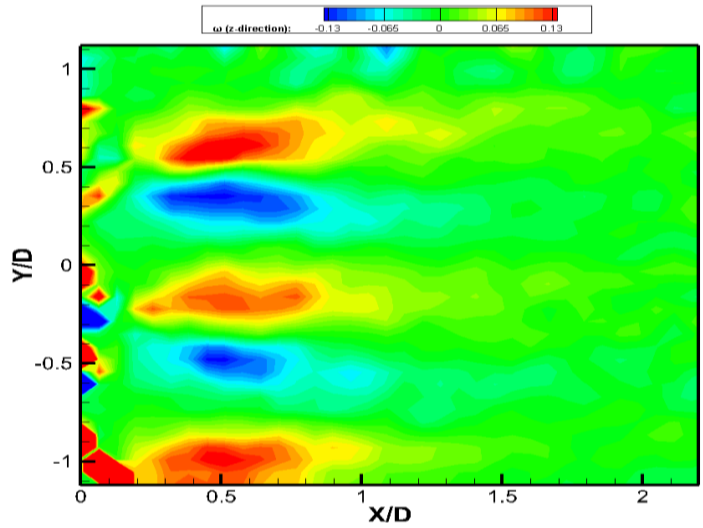

(a) λ/D_{mean} = 1.2

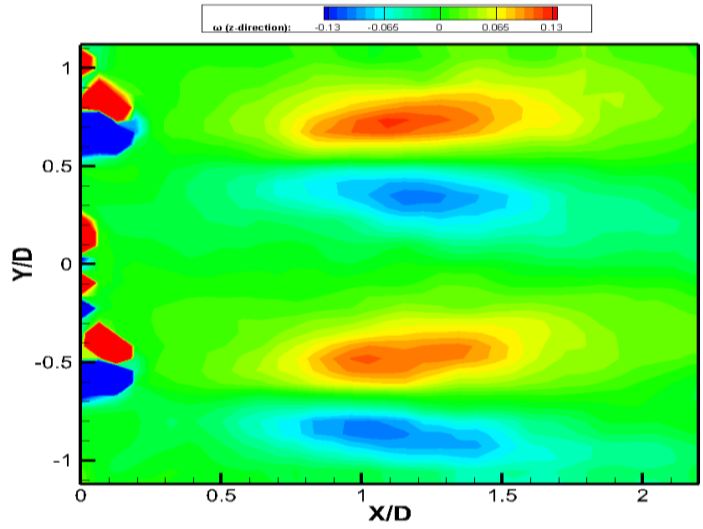

(b) λ/D_{mean} = 1.6

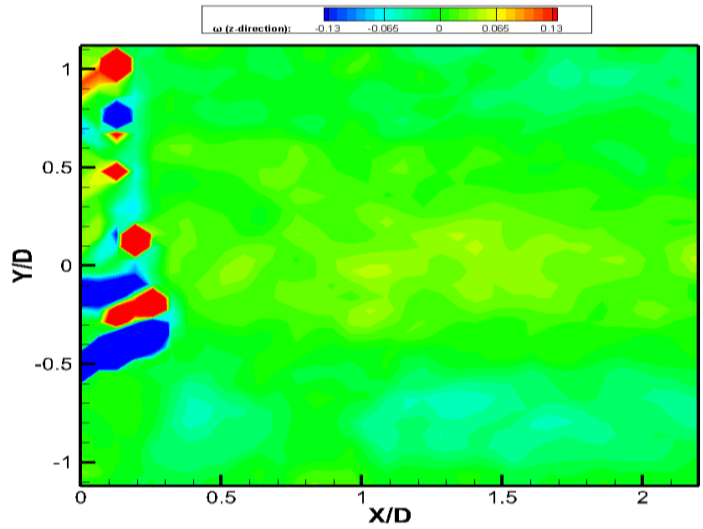

(c) λ/D_{mean} = 2.4

Figure 3.16: Vorticity contour plots in the XY-plane (Re = 15,000, Z/D = -0.45) (a) λ/D_{mean} = 1.2 (b) λ/D_{mean} = 1.6 (c) λ/D_{mean} = 2.4

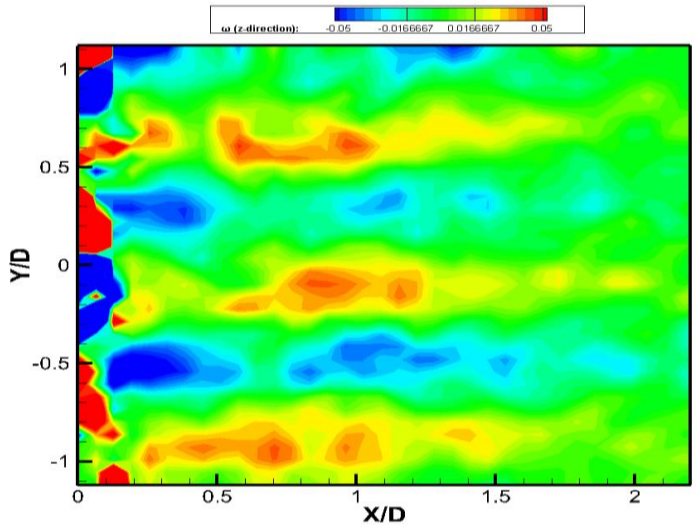

(a) λ/D_{mean} = 1.2

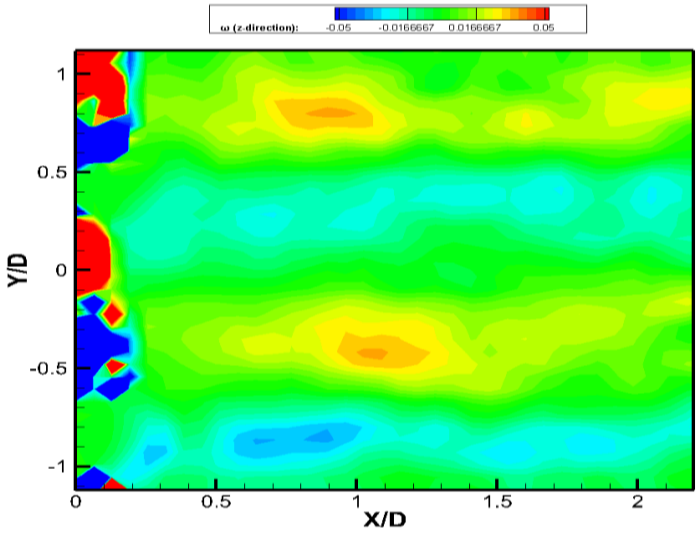

(b) λ/D_{mean} = 1.6

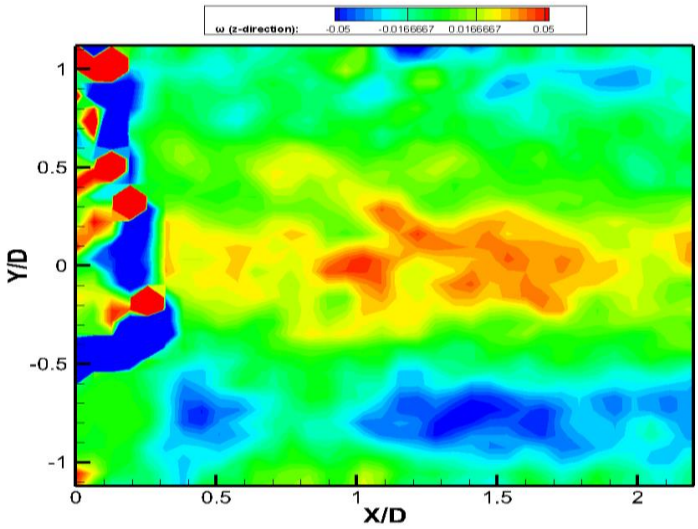

(c) λ/D_{mean} = 2.4

Figure 3.17: Vorticity contour plots in the XY-plane (Re = 15,000, centerline)
(a) λ/D_{mean} = 1.2 (b) λ/D_{mean} = 1.6 (c) λ/D_{mean} = 2.4

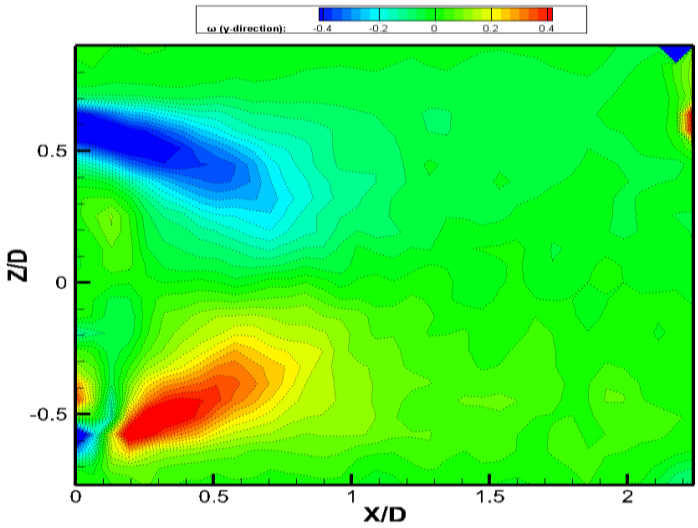

(a) λ/D_{mean} = 1.2

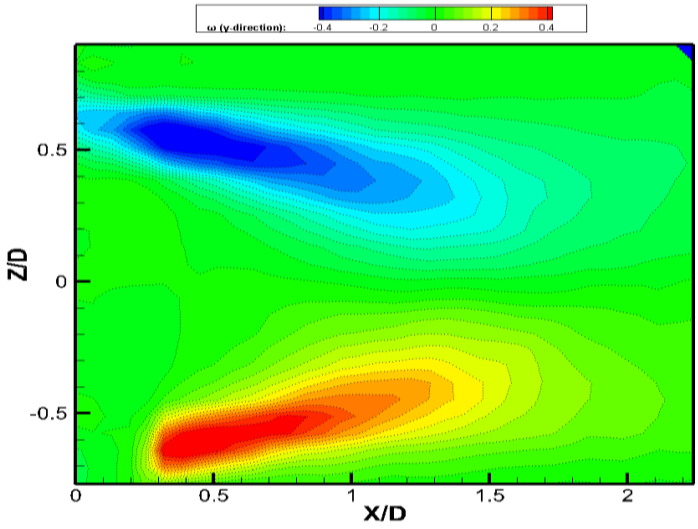

(b) λ/D_{mean} = 1.6

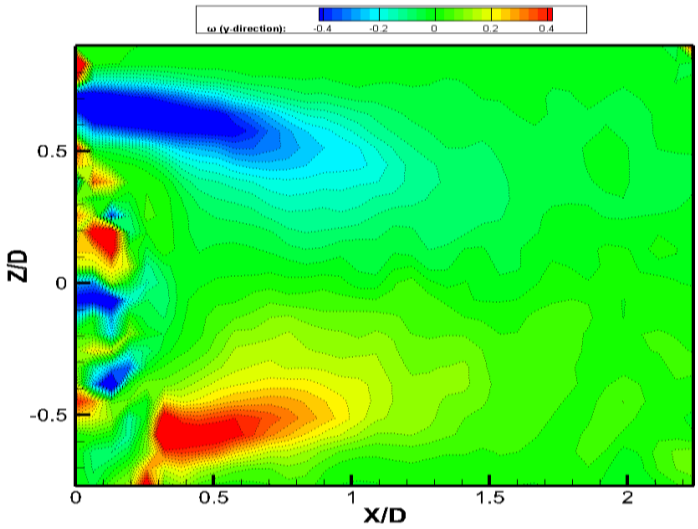

(c) λ/D_{mean} = 2.4

Figure 3.18: Vorticity contour plots in the XZ-plane (Re = 15,000, Node plane)
(a) λ/D_{mean} = 1.2 (b) λ/D_{mean} = 1.6 (c) λ/D_{mean} = 2.4

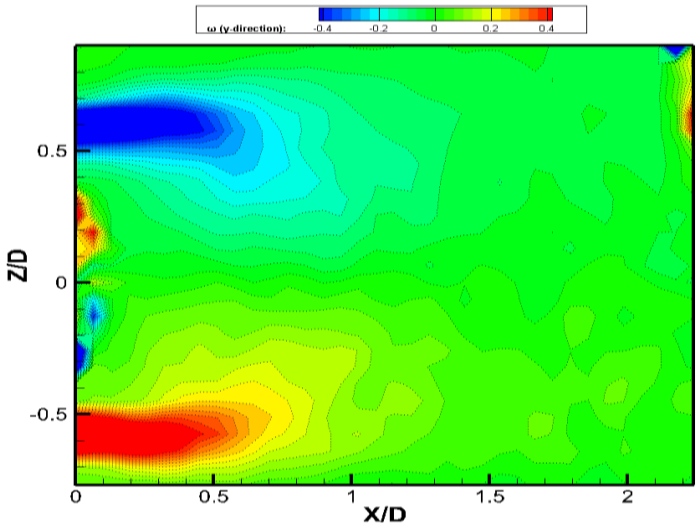

(a) λ/D_{mean} = 1.2

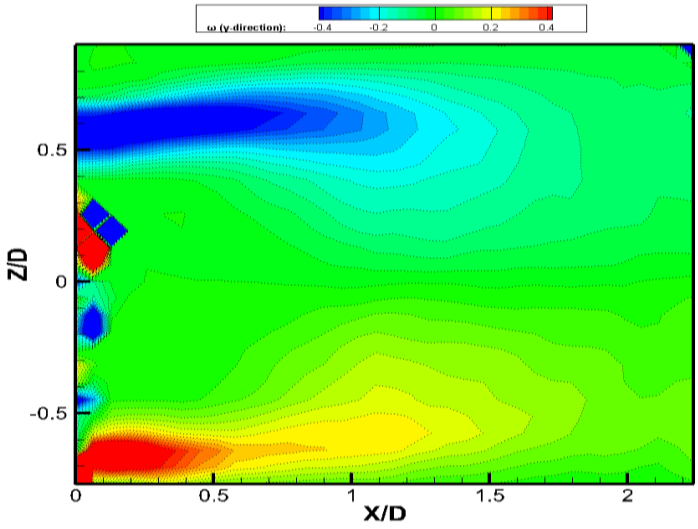

(b) λ/D_{mean} = 1.6

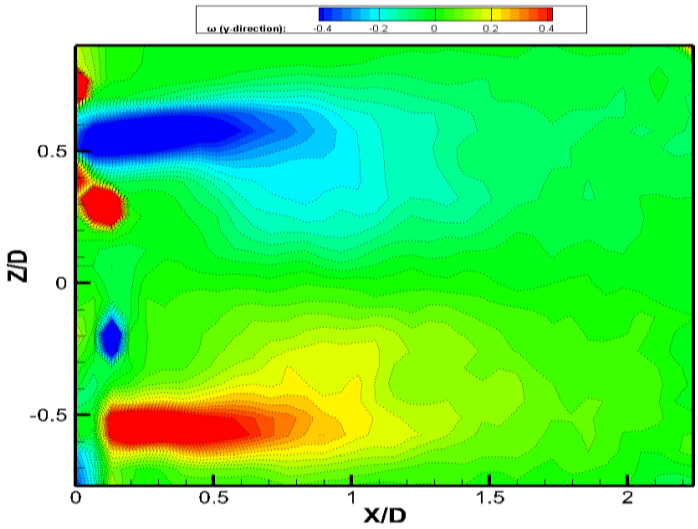

(c) λ/D_{mean} = 2.4

Figure 3.19: Vorticity contour plots in the XZ-plane (Re = 15,000, Saddle plane) (a) λ/D_{mean} = 1.2 (b) λ/D_{mean} = 1.6 (c) λ/D_{mean} = 2.4

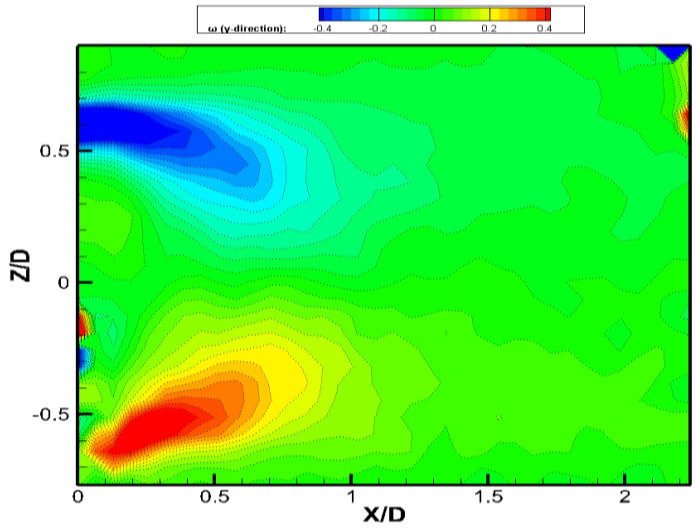

(a) λ/D_{mean} = 1.2

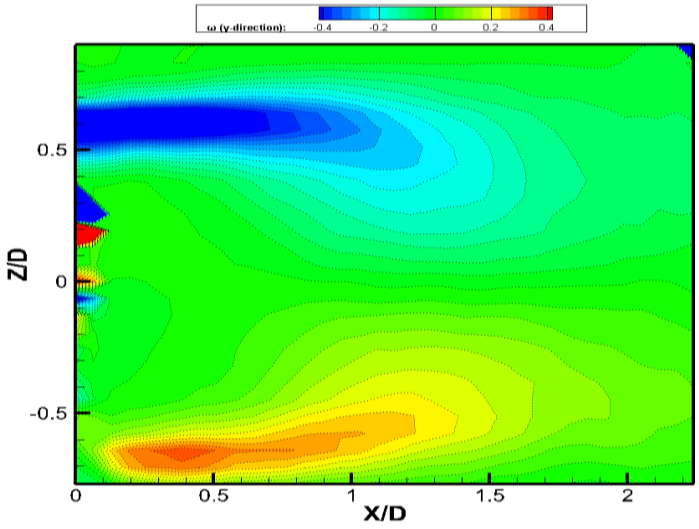

(b) λ/D_{mean} = 1.6

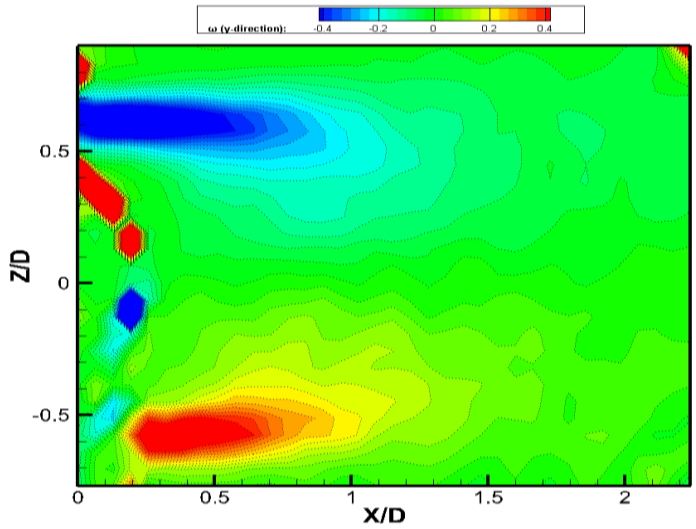

(a) λ/D_{mean} = 2.4

Figure 3.20: Vorticity contour plots in the XZ-plane (Re = 15,000, Middle plane)
(a) λ/D_{mean} = 1.2 (b) λ/D_{mean} = 1.6 (c) λ/D_{mean} = 2.4

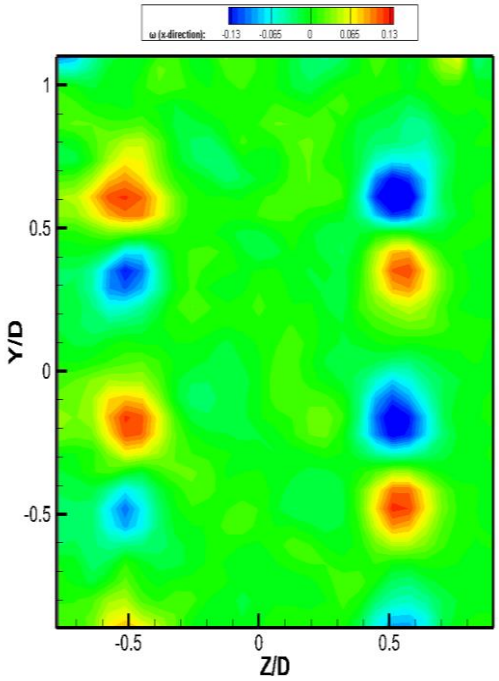

(a) λ/D_{mean} = 1.2

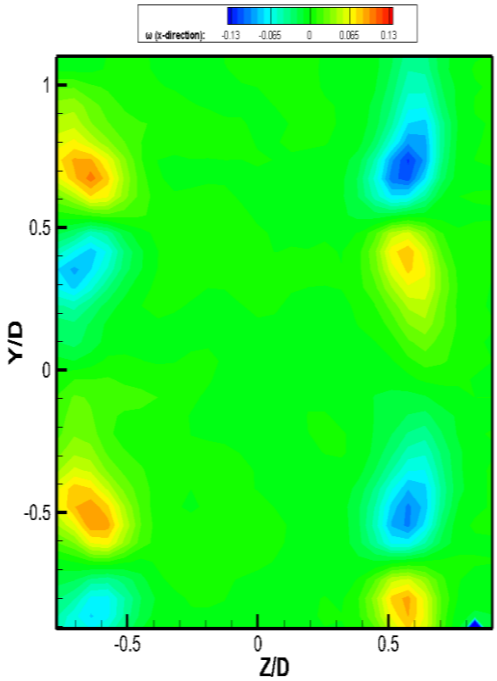

(b) λ/D_{mean} = 1.6

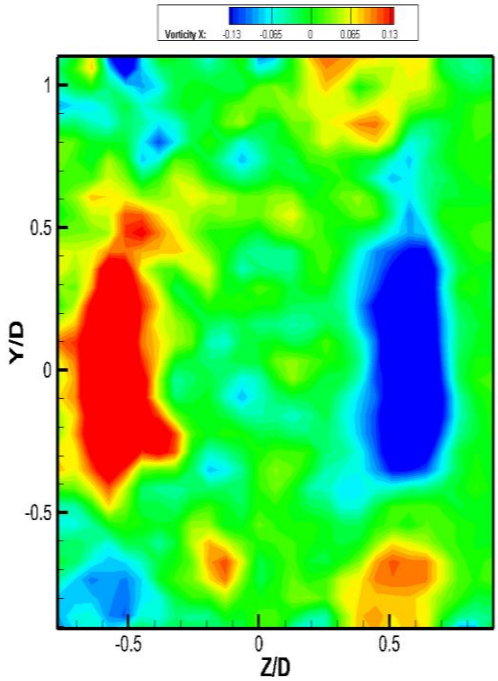

(c) λ/D_{mean} = 2.4

Figure 3.21: Vorticity contour plots in the YZ-plane (Re = 15,000, X/D = 0.3)
(a) λ/D_{mean} = 1.2 (b) λ/D_{mean} = 1.6 (c) λ/D_{mean} = 2.4

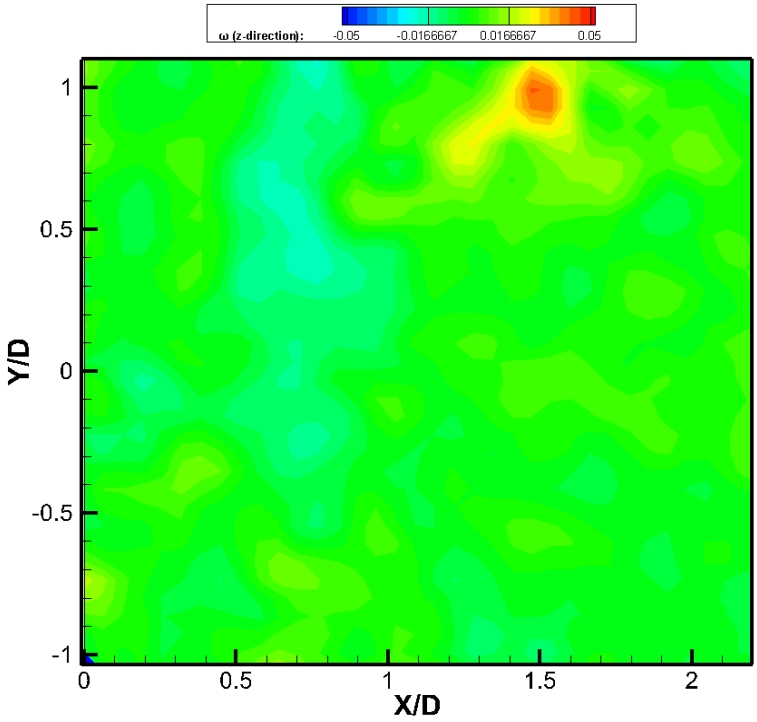

(a)

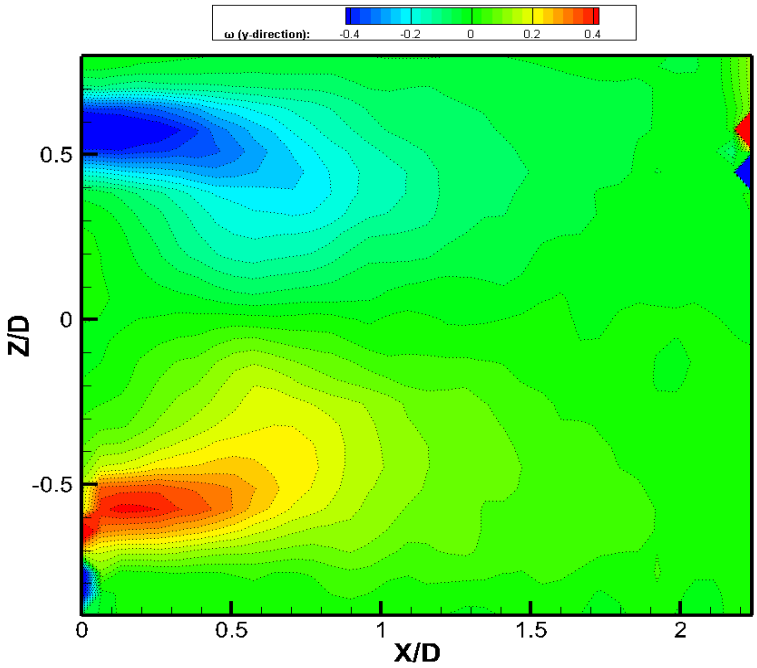

(b)

Figure 3.22: Straight cylinder vorticity contour plots at Re =20,000.
(a) XY plane, Z/D = 0 (b) XZ plane

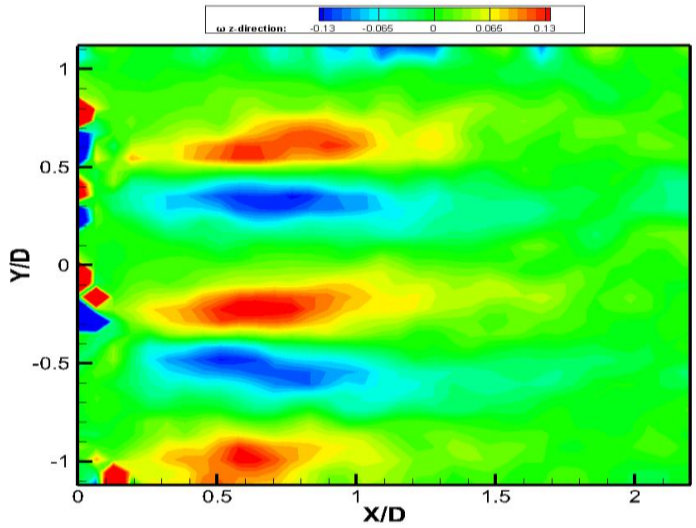

(a) λ/D_{mean} = 1.2

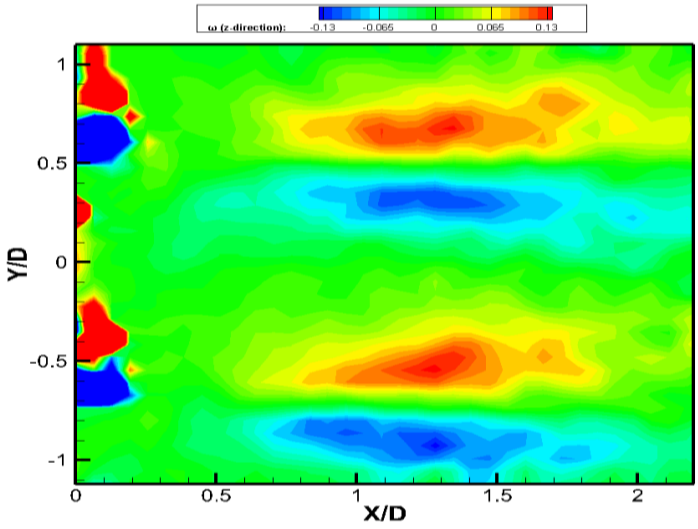

(b) λ/D_{mean} = 1.6

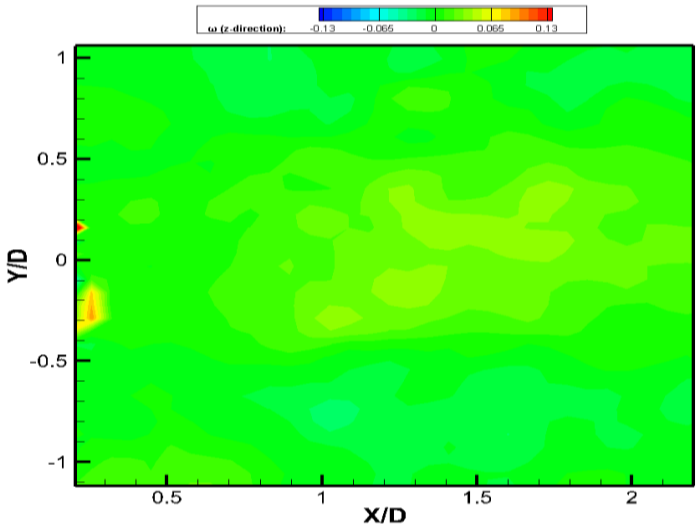

(c) λ/D_{mean} = 2.4

Figure 3.23: Vorticity contour plots in the XY-plane (Re = 20,000, Z/D = -0.45) (a) λ/D_{mean} = 1.2 (b) λ/D_{mean} = 1.6 (c) λ/D_{mean} = 2.4

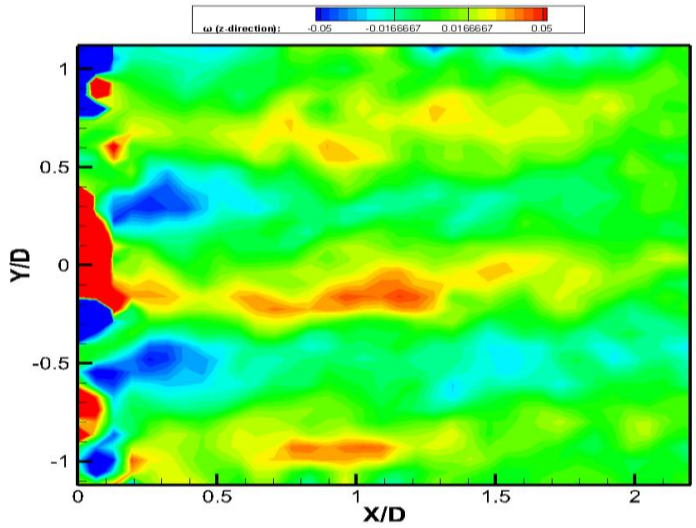

(a) λ/D_{mean} = 1.2

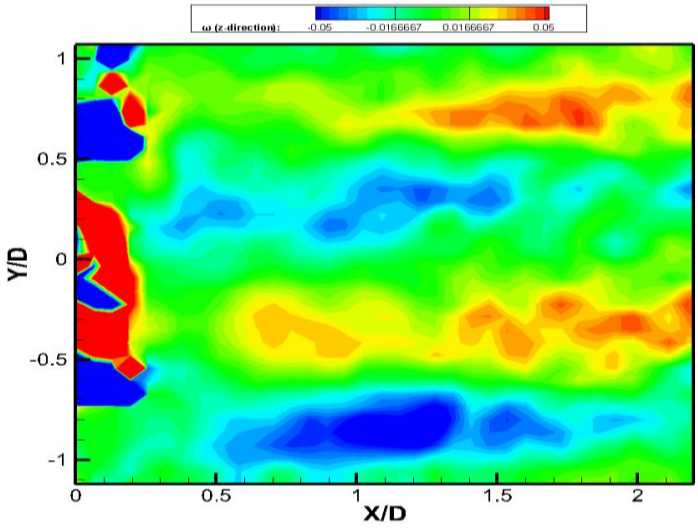

(b) λ/D_{mean} = 1.6

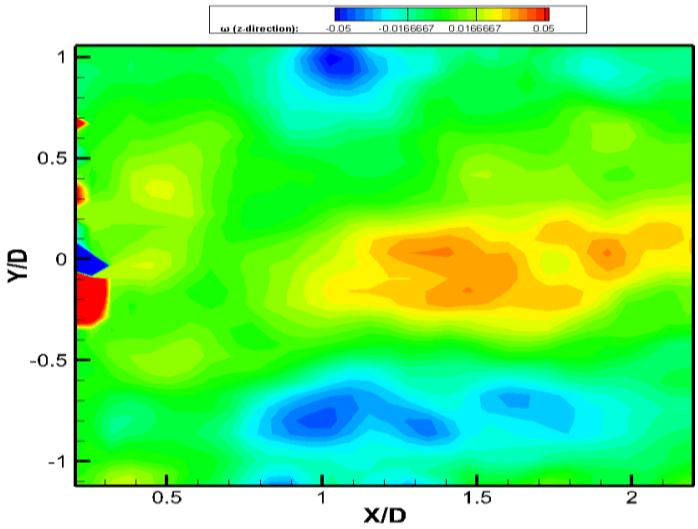

(c) λ/D_{mean} = 2.4

Figure 3.24: Vorticity contour plots in the XY-plane (Re = 20,000, centerline)
(a) λ/D_{mean} = 1.2 (b) λ/D_{mean} = 1.6 (c) λ/D_{mean} = 2.4

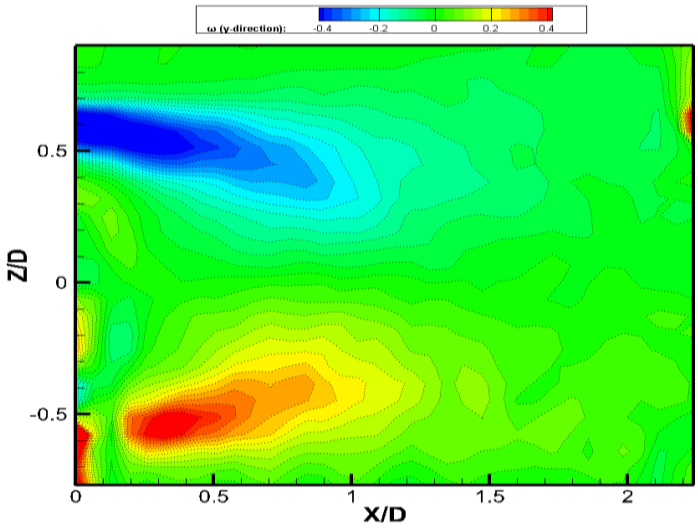

(a) λ/D_{mean} = 1.2

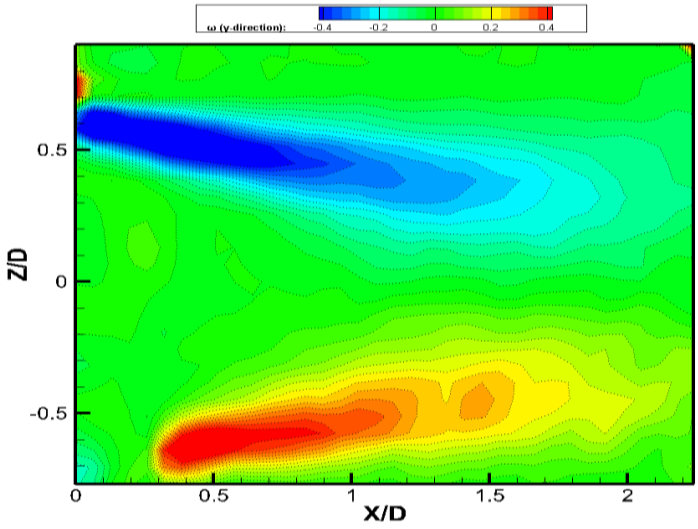

(b) λ/D_{mean} = 1.6

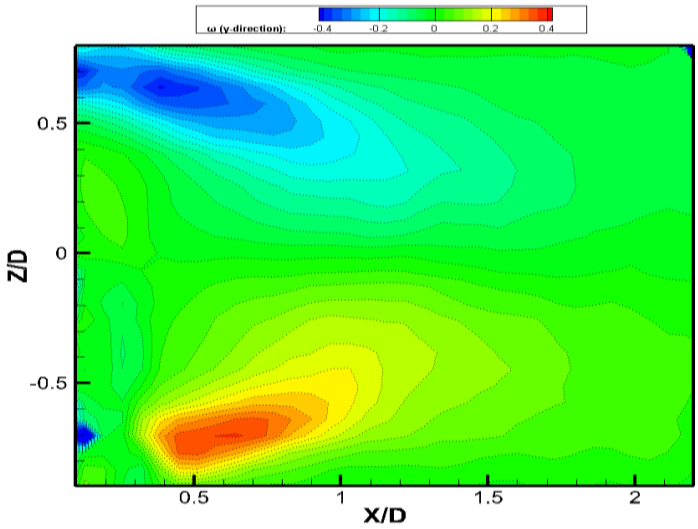

(c) λ/D_{mean} = 2.4

Figure 3.25: Vorticity contour plots in the XZ-plane (Re = 20,000, Node plane)
(a) λ/D_{mean} = 1.2 (b) λ/D_{mean} = 1.6 (c) λ/D_{mean} = 2.4

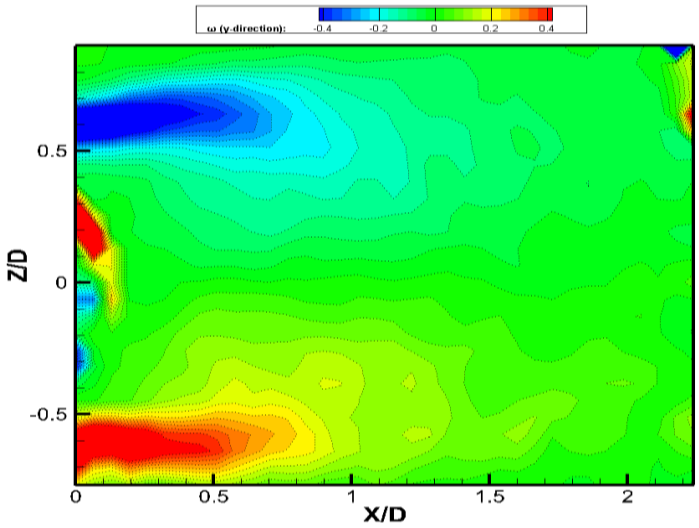

(a) λ/D_{mean} = 1.2

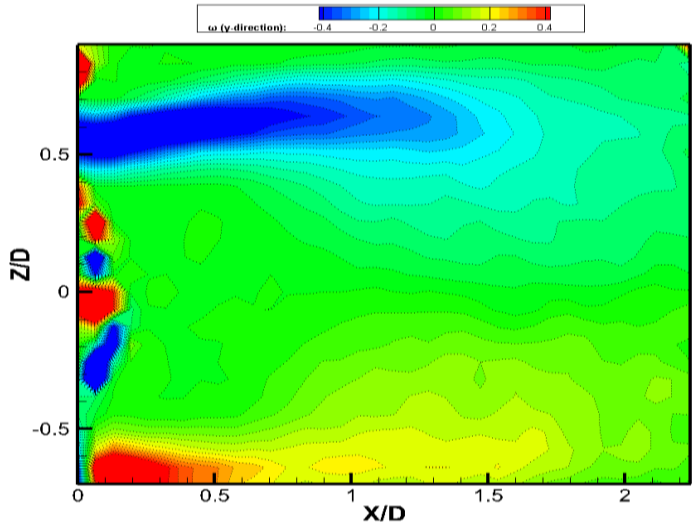

(b) λ/D_{mean} = 1.6

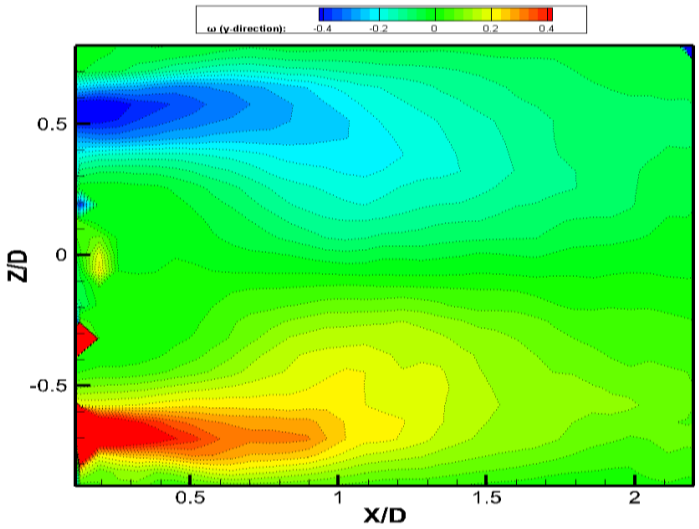

(c) λ/D_{mean} = 2.4

Figure 3.26: Vorticity contour plots in the XZ-plane (Re = 20,000, Saddle plane) (a) λ/D_{mean} = 1.2 (b) λ/D_{mean} = 1.6 (c) λ/D_{mean} = 2.4

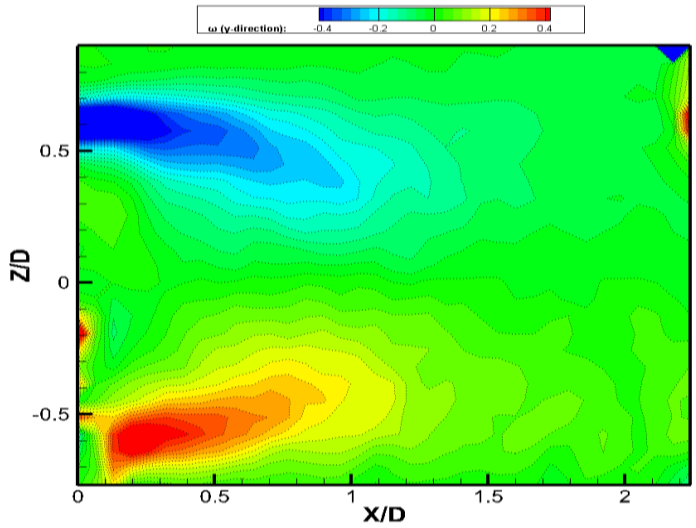

(a) λ/D_{mean} = 1.2

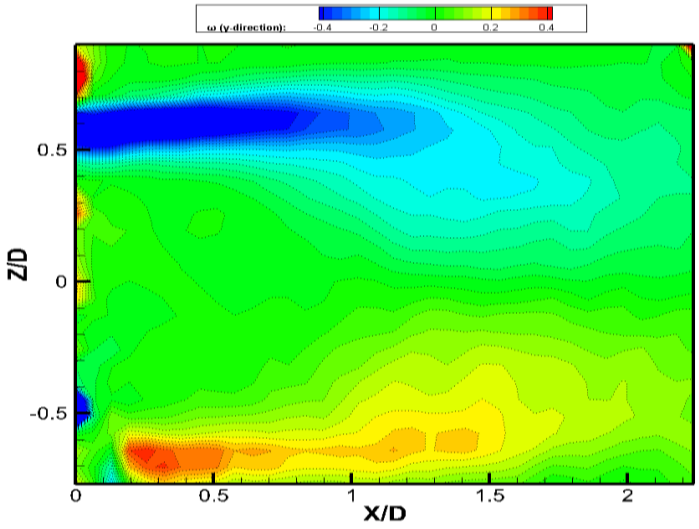

(b) λ/D_{mean} = 1.6

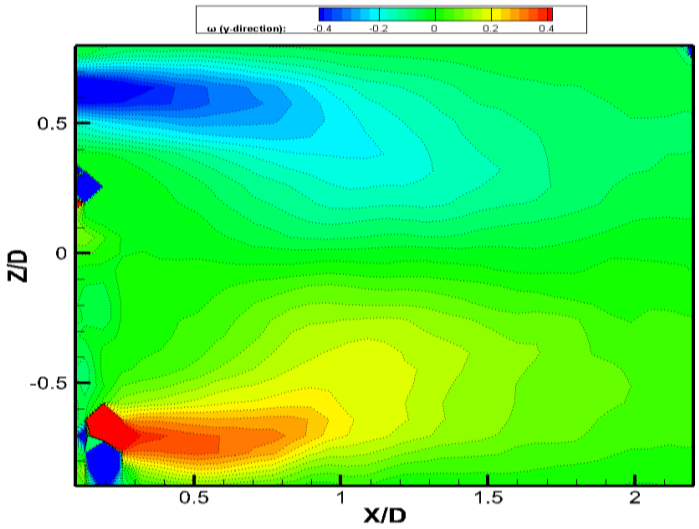

(c) λ/D_{mean} = 2.4

Figure 3.27: Vorticity contour plots in the XZ-plane (Re = 20,000, Middle plane) (a) λ/D_{mean} = 1.2 (b) λ/D_{mean} = 1.6 (c) λ/D_{mean} = 2.4

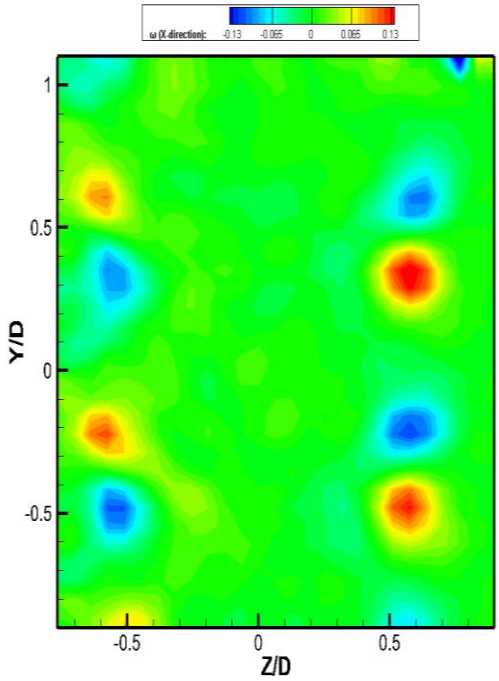

(a) λ/D_{mean} = 1.2

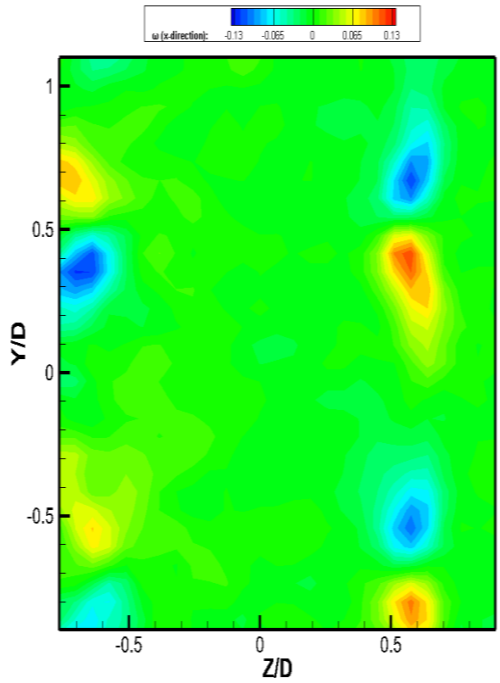

(b) λ/D_{mean} = 1.6

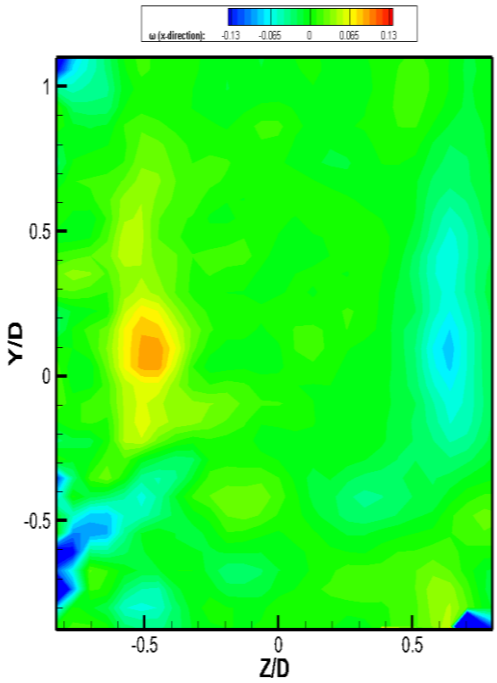

(c) λ/D_{mean} = 2.4

Figure 3.28: Vorticity contour plots in the YZ-plane (Re = 20,000, X/D = 0.3) (a) λ/D_{mean} = 1.2 (b) λ/D_{mean} = 1.6 (c) λ/D_{mean} = 2.4

3.3 Proper orthogonal decomposition modal

The energy distribution plots in Figure 3.43 and Figure 3.44 display how the energy across the POD modes was dropped down exponentially after the five modes, the energy is very small compared to mode 1 and mode 2. As a result, the first two modes can be seen as a dominant flow characteristic and when the mode number increase will shown more eddy and smaller scale vortices in the flow field.

In straight cylinder case, Figure 3.29 and Figure 3.30 show that mode 1 for Re = 15,000 and Re = 20,000 have the highest energy and the vortex formation length is located approximately at the X/D = 0.96 at Re = 15,000 and X/D = 1 at Re = 20,000. Mode 2 and mode 3 exhibit the shear layer on the top of the straight cylinder and the bottom and shedding behind the cylinder. Mode 5 and mode 6 display the vortex shedding periodically on the top and the bottom due to the shear layers interaction. In the mode 5 vortex at the location X/D = 1.7 exhibits that the vortex shedding from the top of the cylinder is cut off from the further supply, then flow to further downstream became a free vortex this phenomena are caused by Karman vortex.

In wavy cylinder case at Re = 15,000, Figure 3.31 shows the cylinder with wavelength λ/D_{mean} = 1.2. Mode 1 shows the vortex located at X/D = 0.9 behind the geometric node and at X/D = 1.1 behind the geometric saddle. Mode 2 and mode 3 displays the shear layer on the top and the bottom of the geometric node and geometric saddle. Mode 4 to mode 6 exhibits the periodic alternative vortex shedding behind the geometric node and geometric saddle. In wavelength λ/D_{mean} = 1.6 (Figure 3.33) vortex formation length shows X/D = 1.1 behind geometric node and X/D = 1.3 behind geometric saddle at mode 1. At Wavelength λ/D_{mean} = 2.4 exhibits (Figure3.35) X/D = 1 behind geometric node and X/D = 1.3 behind geometric saddle at mode 1. At mode 3 the contour plot clearly shows that behind the node the wake is narrower and behind saddle have wake is wider. For Re = 20,000, the wavelength λ/D_{mean} = 1.2 shows the vortex formation length behind geometric node is X/D = 1.05 and X/D = 1, at λ/D_{mean} = 1.6 exhibit X/D = 1.5 behind the node and X/D = 1.35 behind the saddle, at λ/D_{mean} = 2.4 X/D = 1.2 behind node and X/D = 1.3 behind the saddle. For the wavelength λ/D_{mean} = 1.2, λ/D_{mean} = 1.6 and λ/D_{mean} = 2.4 at Re = 15,000 and Re = 20,000, the contour plot displays the similar flow characteristics behind the geometric node and geometric saddle. However, the vortex formation length behind the geometric saddle is shorter than the vortex formation length behind the geometric node at wavelength $/D_{mean}$ = 1.6. The result agrees with the mean velocity contour plots in that wavy cylinders have a longer overall vortex

formation lengths compared to the straight cylinder. Elongated vortex formation length behind the wavy cylinder indicated lower drag and less vibration.

Figure 3.43 and Figure 3.44 display the POD energy distribution plot at Re = 15,000 and Re = 20,000. For Re =15,000 the wavelength λ/D_{mean} = 1.6 shows the lowest energy behind the geometric saddle, behind the geometric node the cylinder show the lowest energy and wavelength λ/D_{mean} = 1.2 shows the highest energy behind the geometric saddle and geometric node. For Re = 20,000, the wavelength λ/D_{mean} = 1.6 exhibits the lowest energy behind the geometric node and geometric saddle compared to straight cylinder and other wavy models. This indicated the wavy geometry created the three-dimensional wake and when the boundary layer separated from the geometric saddle and toward to the geometric node then rolling up to developed the streamwise vortices between the geometric saddle and geometric node. The streamwise vortices play a crucial role that suppress the free shear layer to roll up, thus suppress the spanwise vortex to developed into mature vortex or developed into mature at a further downstream location.

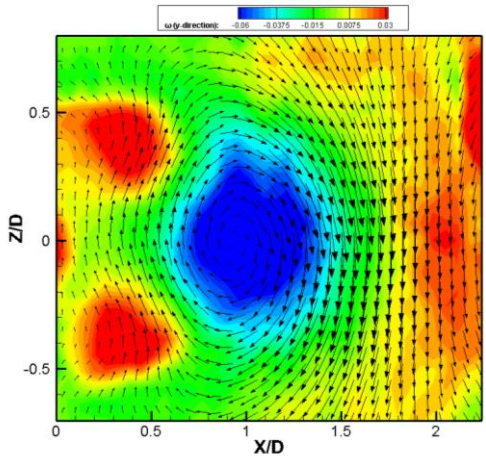

(a) Mode 1

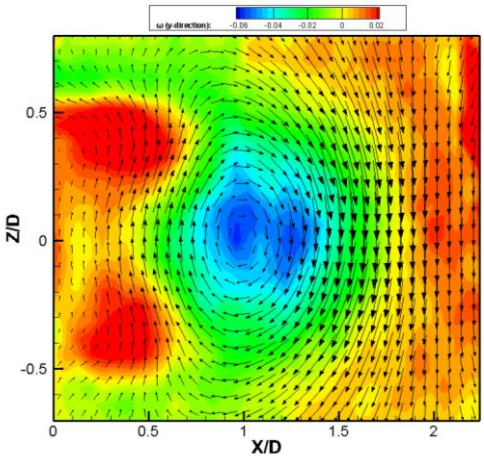

(a) Mode 1

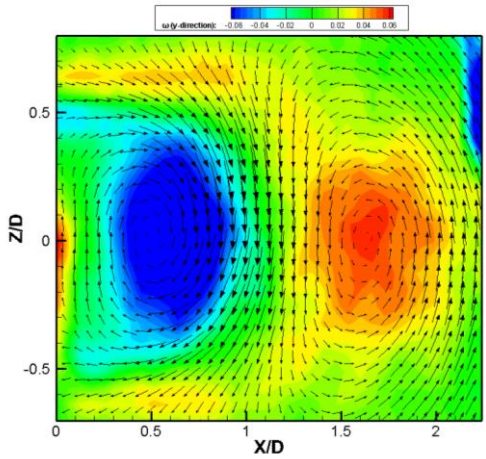

(b) Mode 2

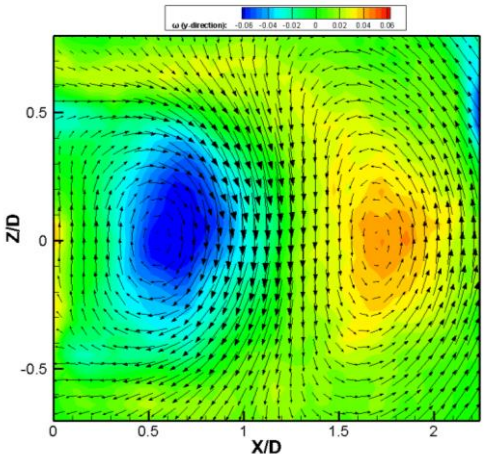

(b) Mode 2

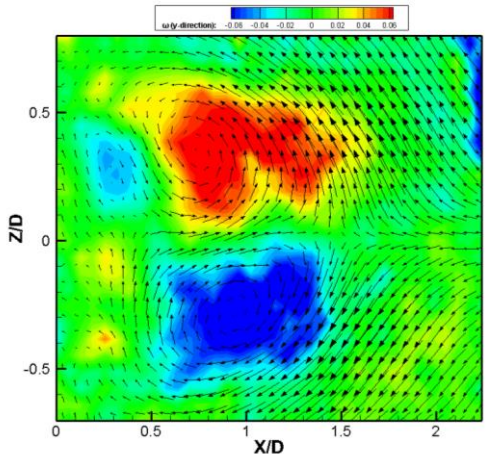

(c) Mode 3

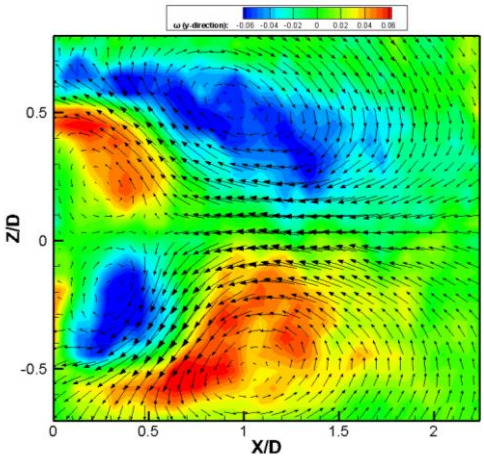

(b) Mode 3

Figure 3.29: Straight cylinder POD vorticity contour plots at XZ plane

(a) (b) (c) Re = 15,000. (d) (e) (f) Re = 20,000

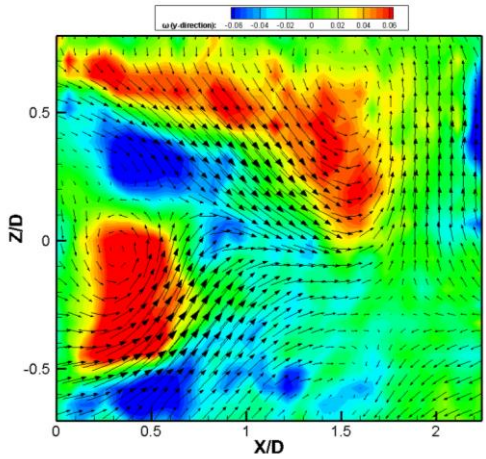

(a) Mode 4

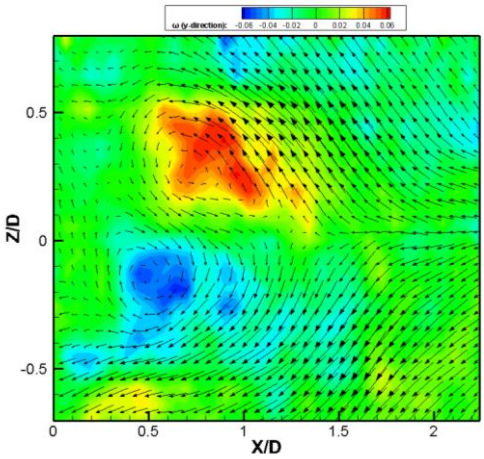

(a) Mode 4

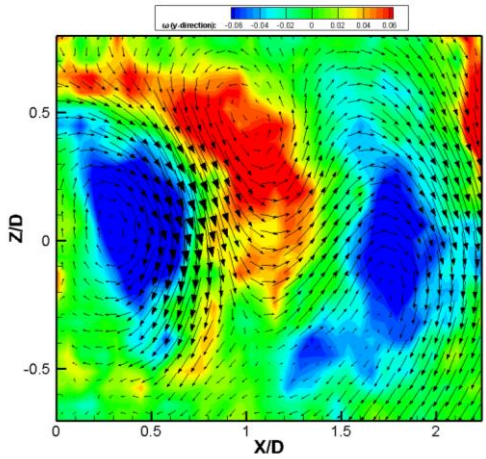

(b) Mode 5

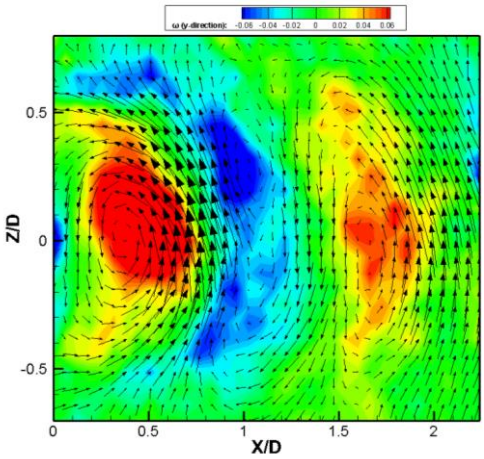

(b) Mode 5

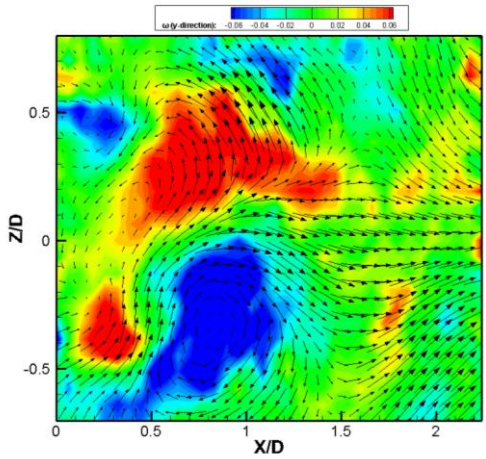

(c) Mode 6

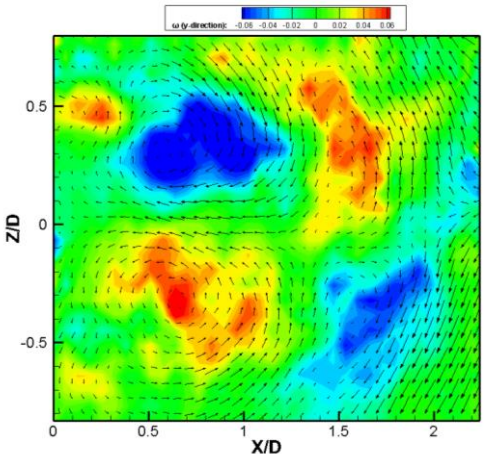

(b) Mode 6

Figure 3.30: Straight cylinder POD vorticity contour plots at XZ plane

(a) (b) (c) Re = 15,000. (d) (e) (f) Re = 20,000

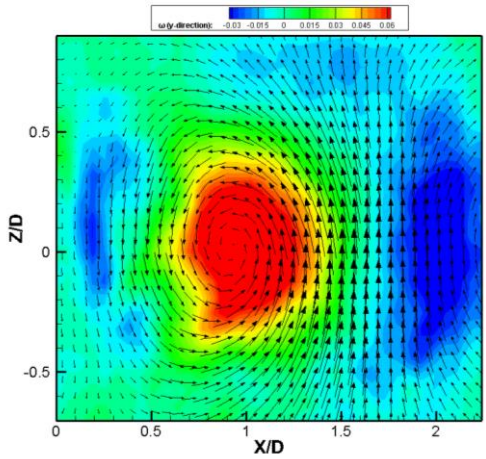

(a) Mode 1, node

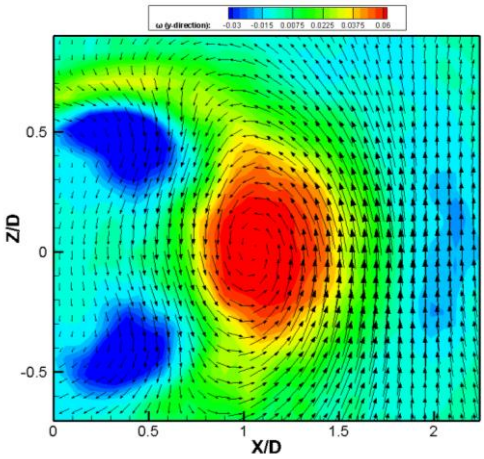

(e) Mode 1, saddle

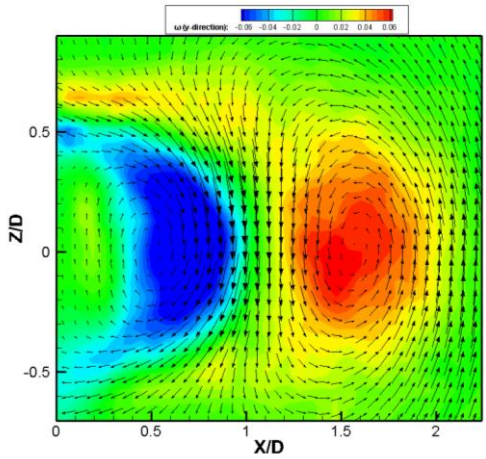

(b) Mode 2, node

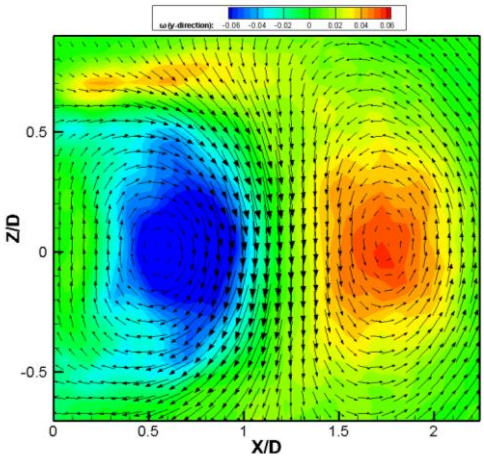

(f) Mode 2, saddle

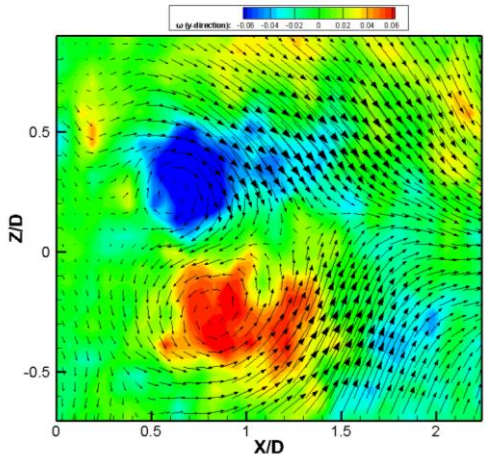

(c) Mode 3,node

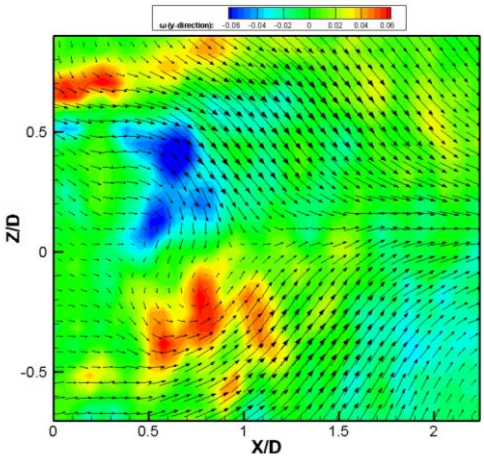

(f) Mode 3, saddle

Figure 3.31: POD vorticity contour plots at XZ plane (Re = 15,000, λ/D_{mean} = 1.2)
(a) (b) (c) Node plane. (d) (e) (f) Saddle plane

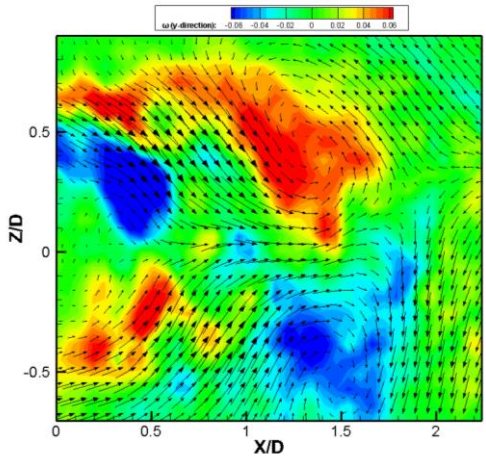

(a) Mode 4, node

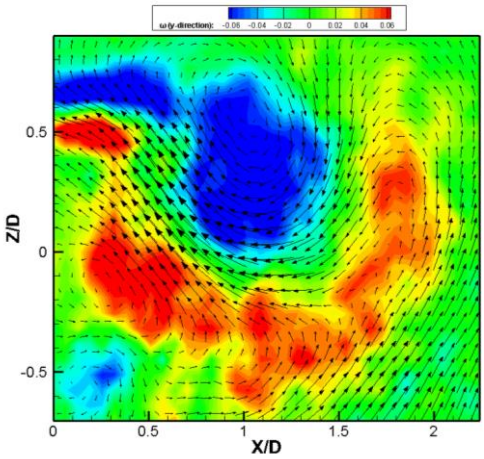

(d) Mode 4, saddle

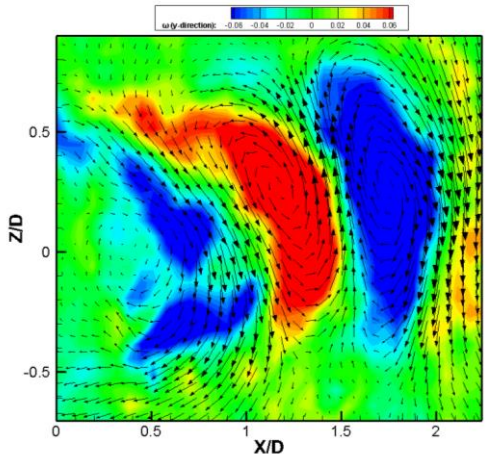

(b) Mode 5, node

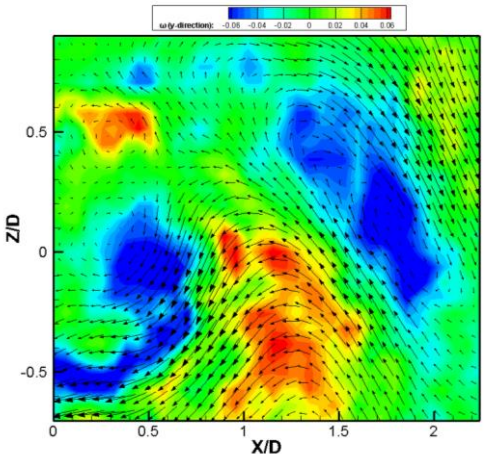

(f) Mode 5, saddle

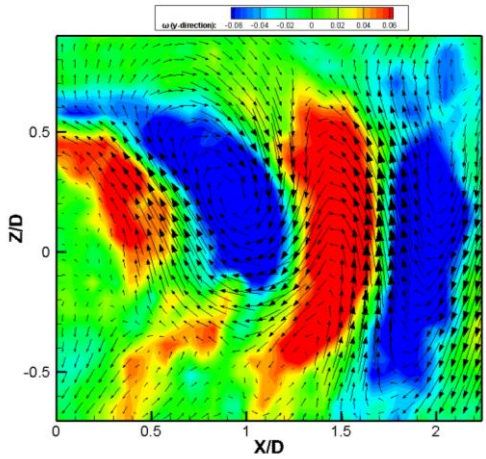

(c) Mode 6, node

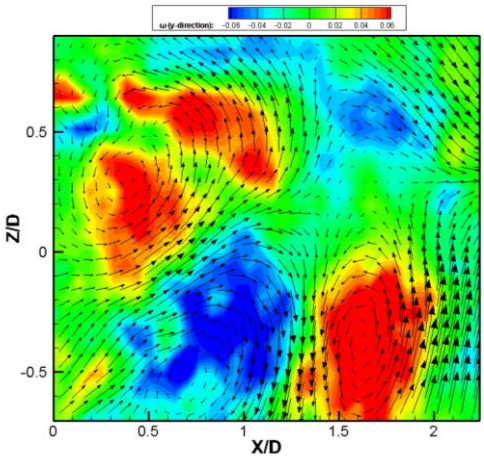

(f) Mode 6, saddle

Figure 3.32: POD vorticity contour plots at XZ plane (Re = 15,000, λ/D_{mean} = 1.2)
(a) (b) (c) Node plane. (d) (e) (f) Saddle plane

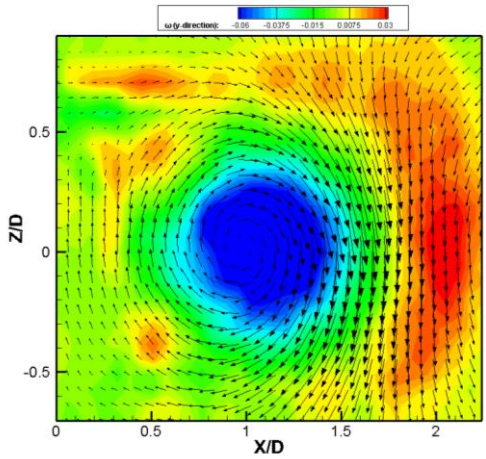

(a) Mode 1, node

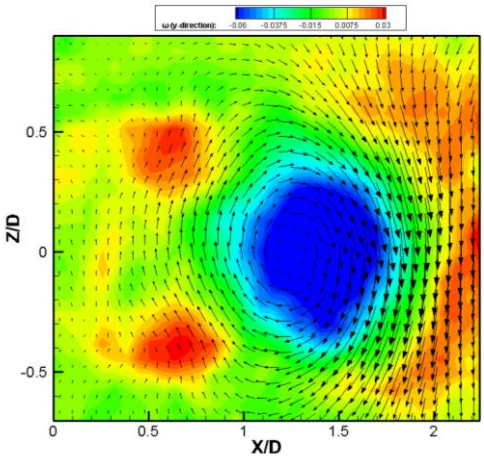

(a) Mode 1, saddle

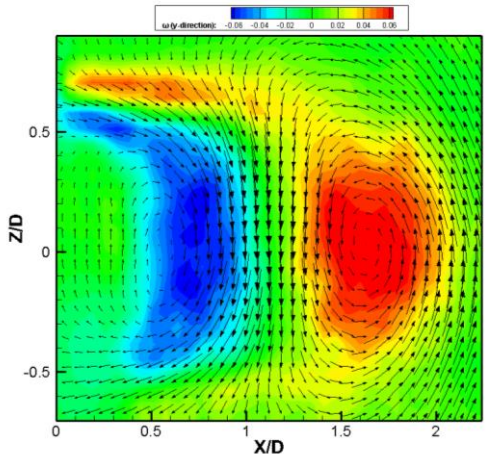

(b) Mode 2, node

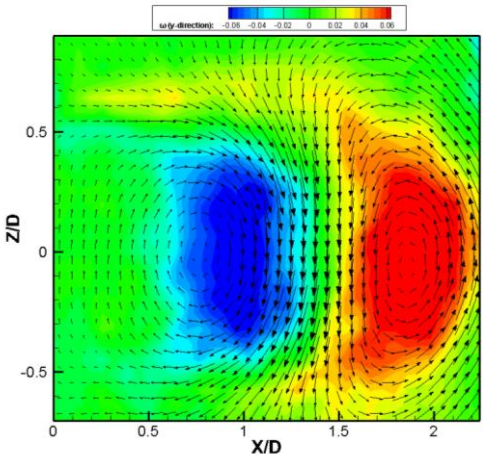

(b) Mode 2, saddle

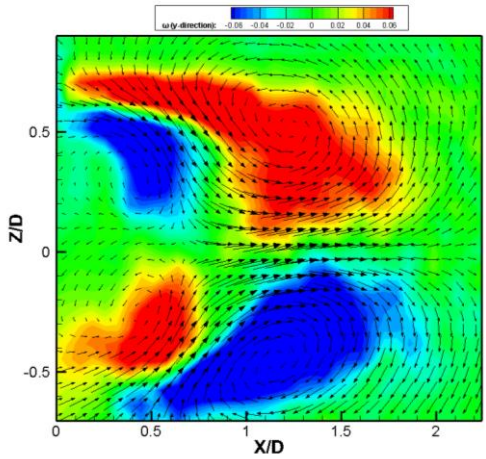

(c) Mode 3,node

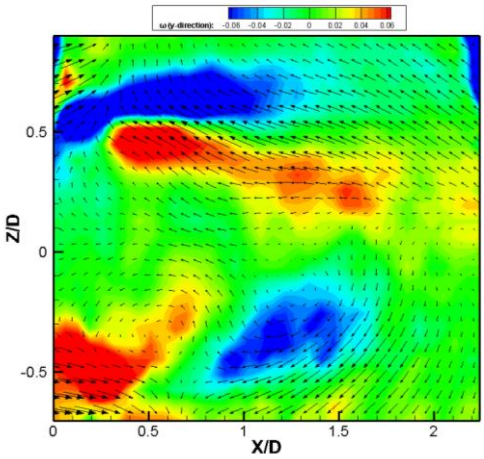

(c) Mode 3, saddle

Figure 3.33: POD vorticity contour plots at XZ plane (Re = 15,000, λ/D_{mean} = 1.6)
(a) (b) (c) Node plane. (d) (e) (f) Saddle plane

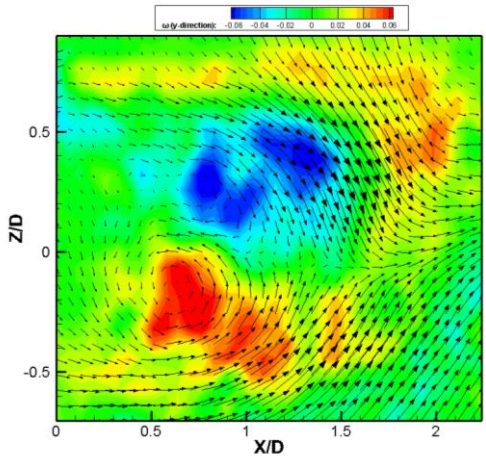

(a) Mode 4, node

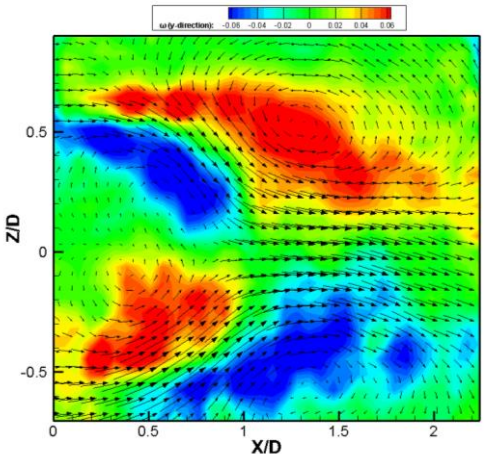

(d) Mode 4, saddle

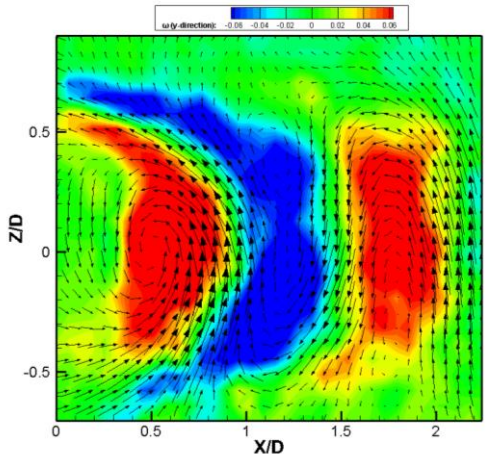

(b) Mode 5, node

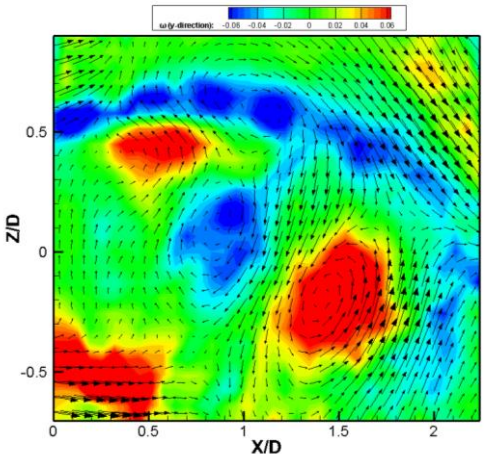

(f) Mode 5, saddle

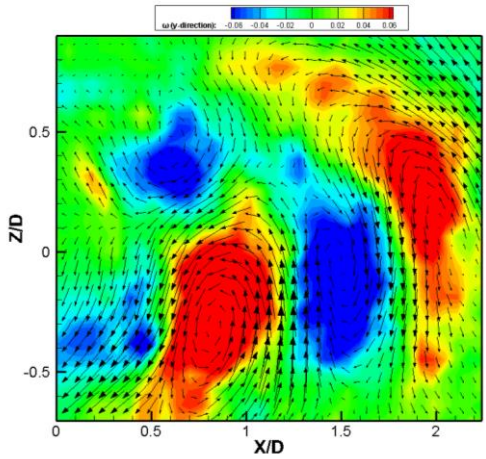

(c) Mode 6, node

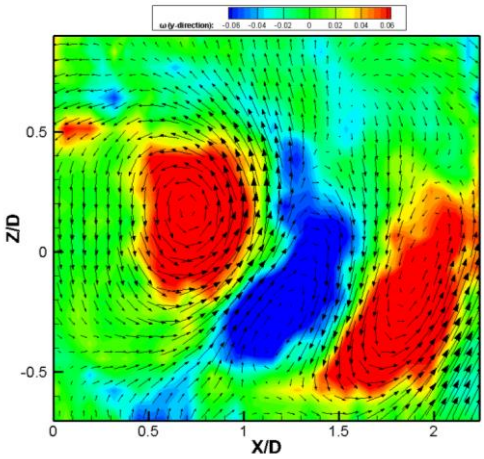

(f) Mode 6, saddle

Figure 3.34: POD vorticity contour plots at XZ plane (Re = 15,000, λ/D_{mean} = 1.6)
(a) (b) (c) Node plane. (d) (e) (f) Saddle plane

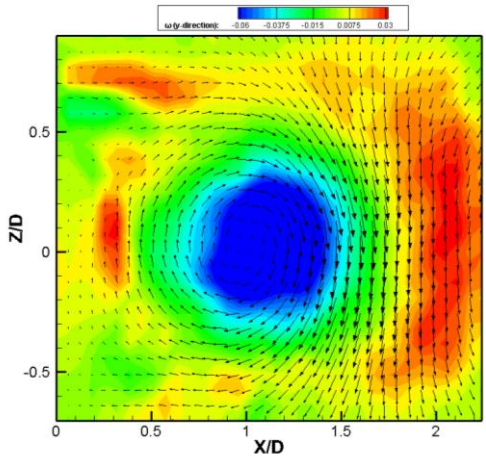

(a) Mode 1, node

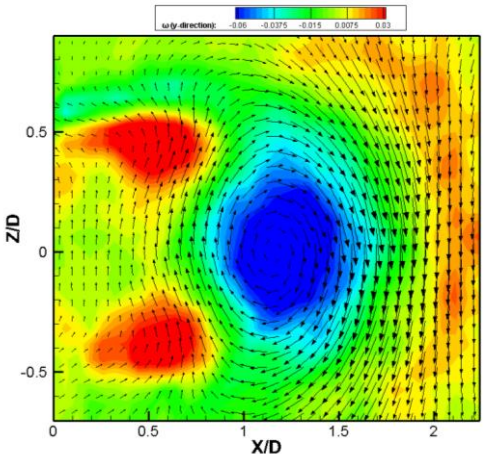

(e) Mode 1, saddle

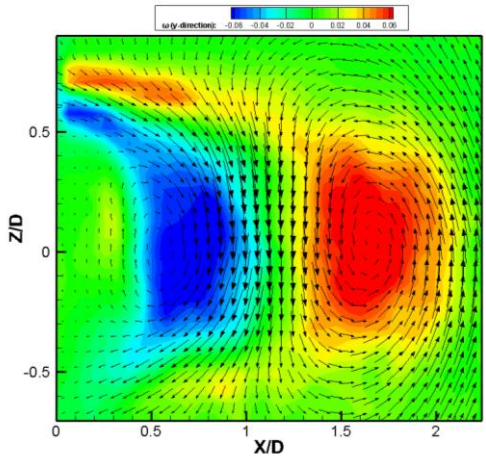

(b) Mode 2, node

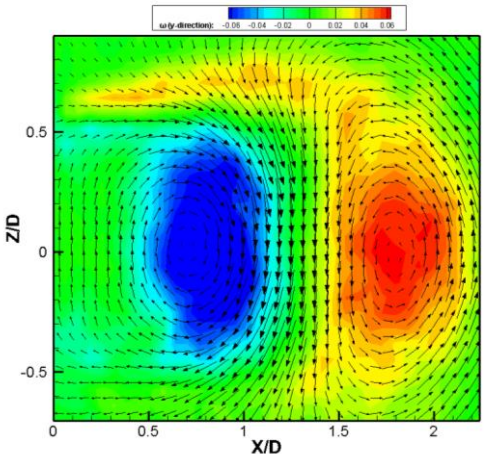

(f) Mode 2, saddle

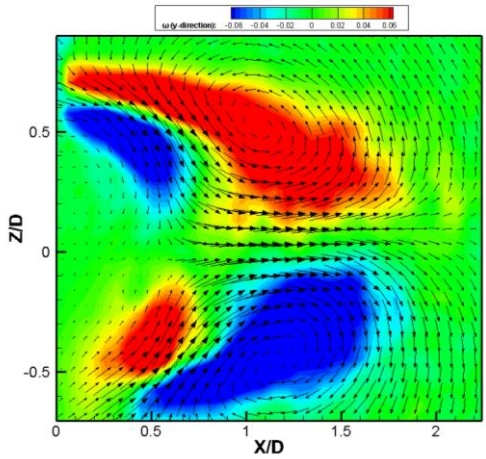

(c) Mode 3,node

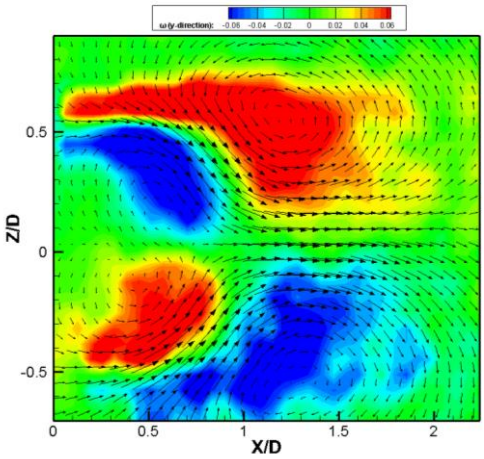

(f) Mode 3, saddle

Figure 3.35: POD vorticity contour plots at XZ plane (Re = 15,000, λ/D_{mean} = 2.4)

(a) (b) (c) Node plane. (d) (e) (f) Saddle plane

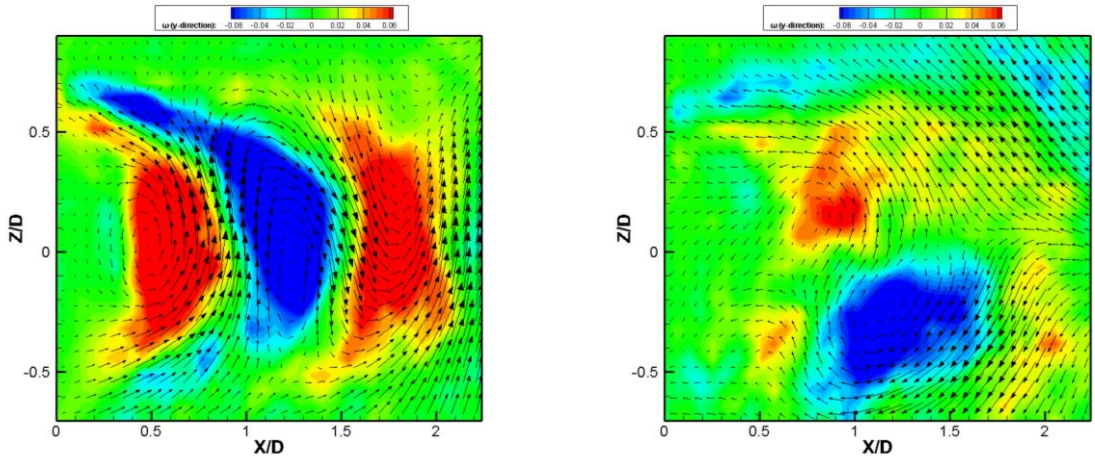

(a) Mode 4, node (d) Mode 4, saddle

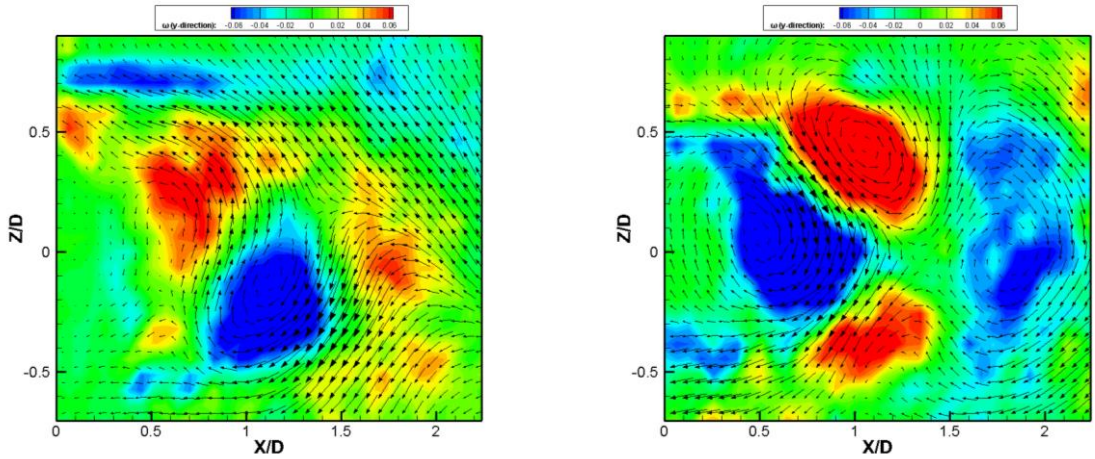

(b) Mode 5, node (e) Mode 5, saddle

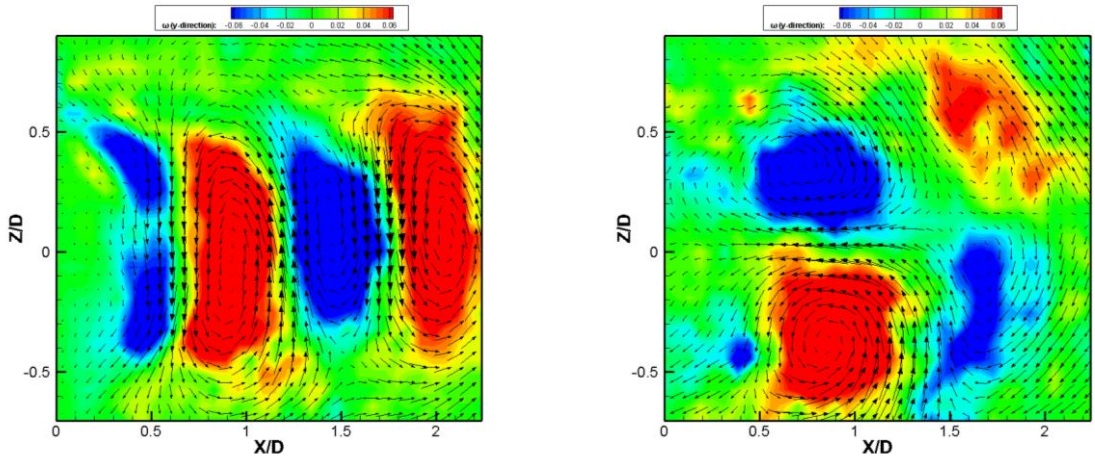

(c) Mode 6, node (f) Mode 6, saddle

Figure 3.36: POD vorticity contour plots at XZ plane (Re = 15,000, λ/D_{mean} = 2.4)
(a) (b) (c) Node plane. (d) (e) (f) Saddle plane

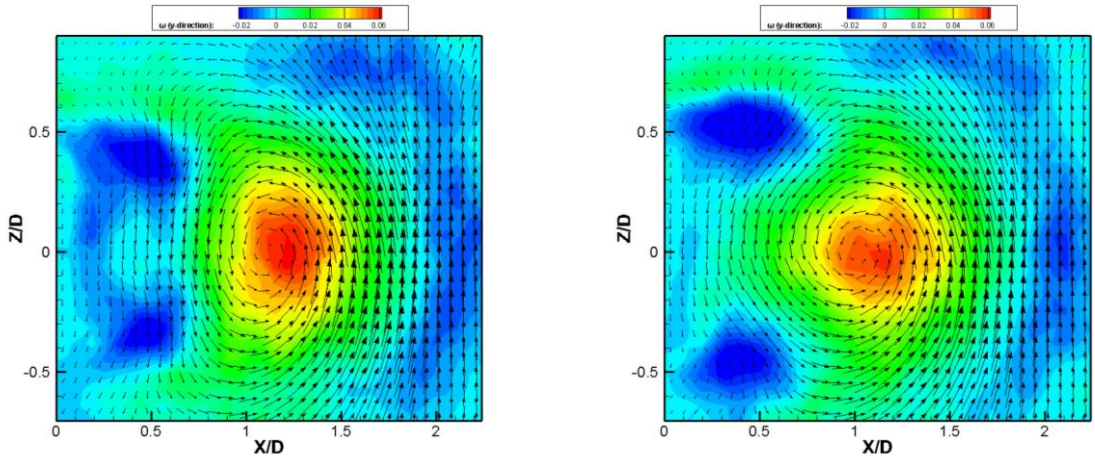

(a) Mode 1, node (d) Mode 1, saddle

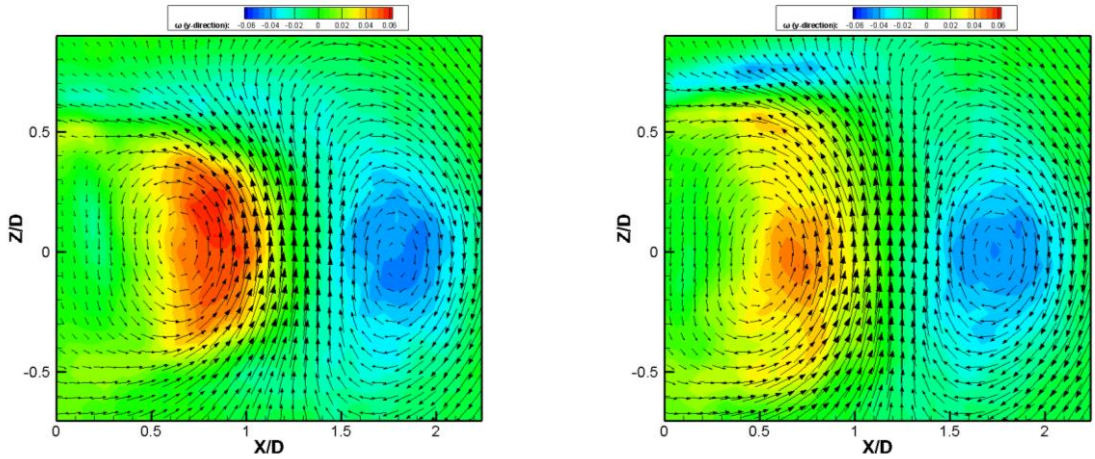

(b) Mode 2, node (e) Mode 2, saddle

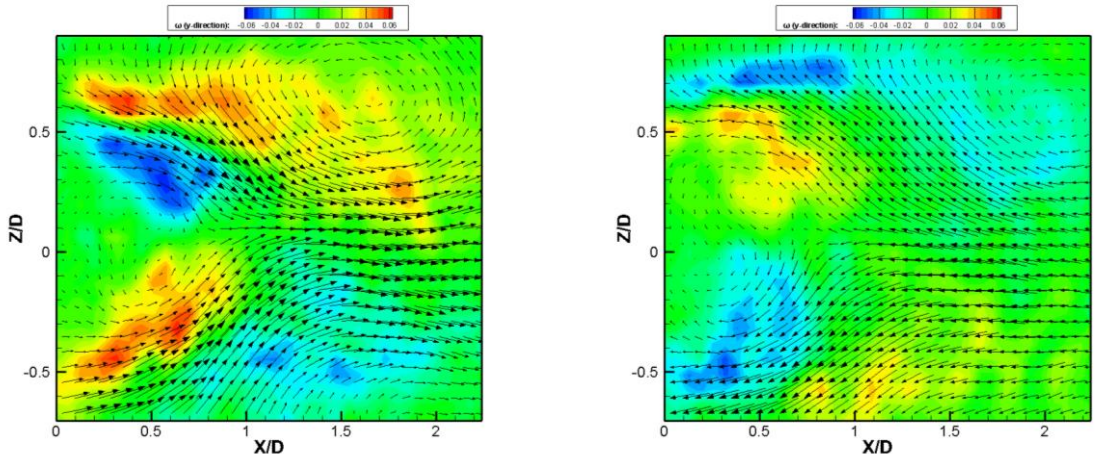

(c) Mode 3, node (f) Mode 3, saddle

Figure 3.37: POD vorticity contour plots at XZ plane (Re = 20,000, λ/D_{mean} = 1.2)
(a) (b) (c) Node plane. (d) (e) (f) Saddle plane

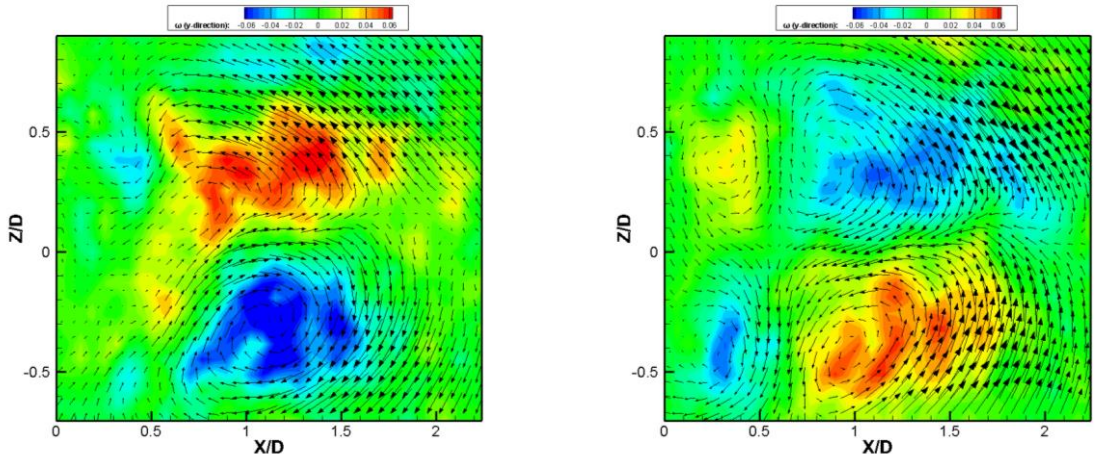

(a) Mode 4, node (d) Mode 4, saddle

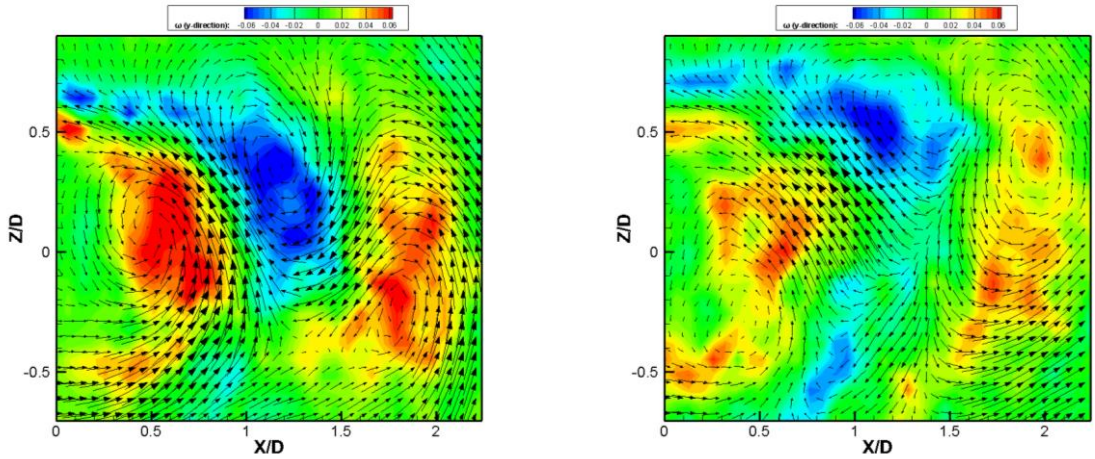

(b) Mode 5, node (e) Mode 5, saddle

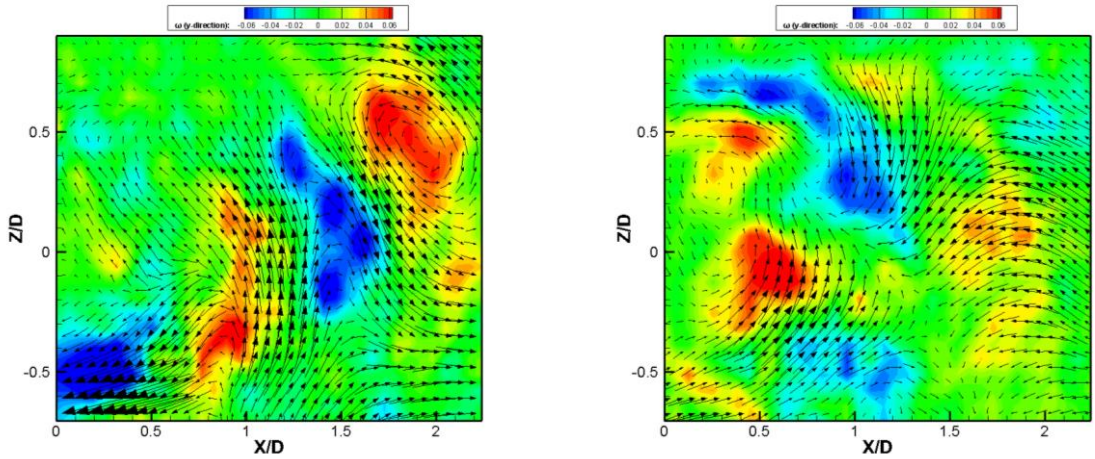

(c) Mode 6, node (f) Mode 6, saddle

Figure 3.38: POD vorticity contour plots at XZ plane (Re = 20,000, λ/D_{mean} = 1.2)
(a) (b) (c) Node plane. (d) (e) (f) Saddle plane

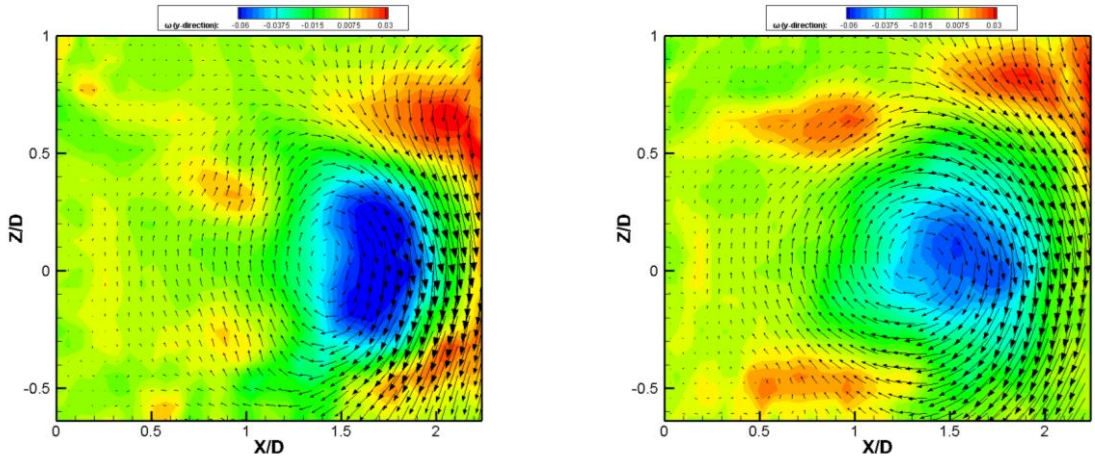

(a) Mode 1, node

(d) Mode 1, saddle

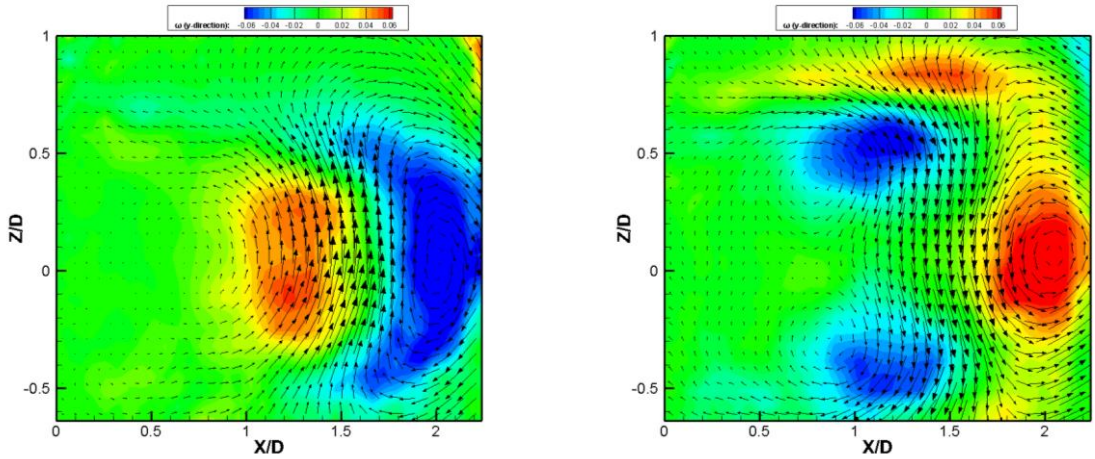

(b) Mode 2, node

(e) Mode 2, saddle

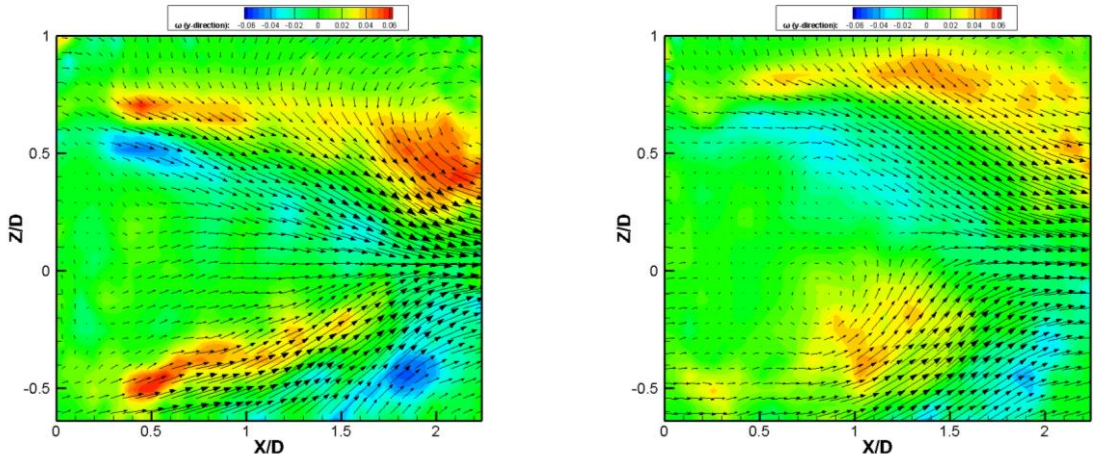

(c) Mode 3, node

(f) Mode 3, saddle

Figure 3.39: POD vorticity contour plots at XZ plane (Re = 20,000, λ/D_{mean} = 1.6)

(a) (b) (c) Node plane. (d) (e) (f) Saddle plane

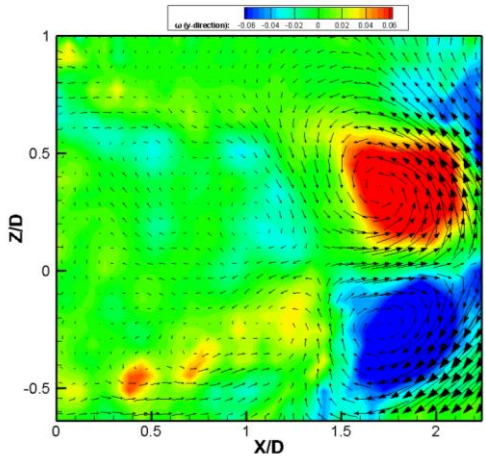

(a) Mode 4, node

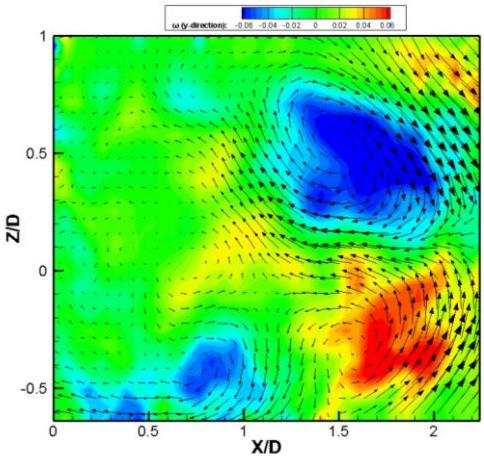

(d) Mode 4, saddle

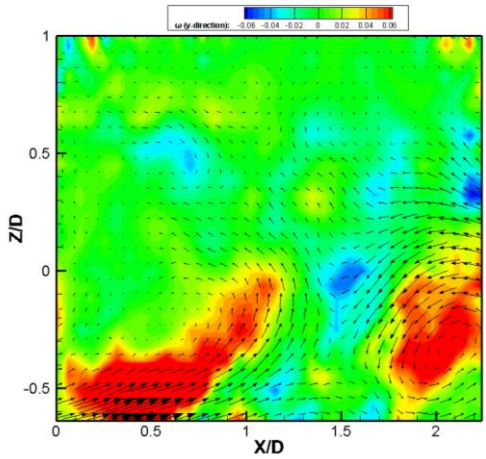

(b) Mode 5, node

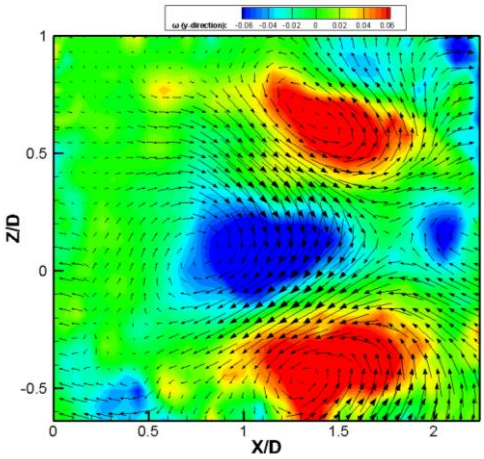

(e) Mode 5, saddle

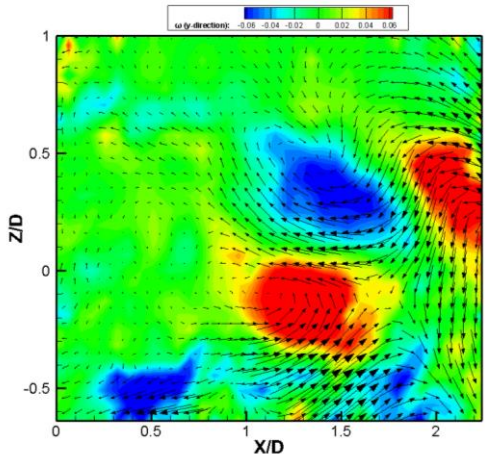

(c) Mode 6, node

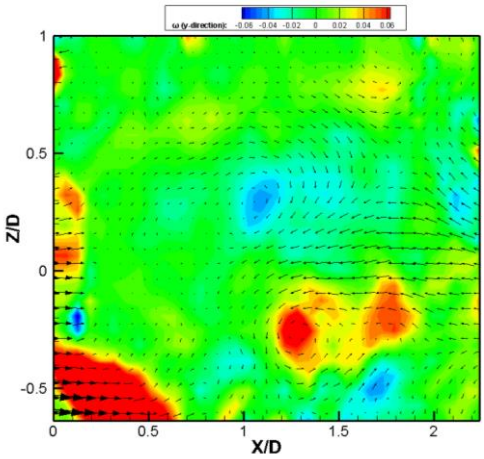

(f) Mode 6, saddle

Figure 3.40: POD vorticity contour plots at XZ plane (Re = 20,000, λ/D_{mean} = 1.6)
(a) (b) (c) Node plane. (d) (e) (f) Saddle plane

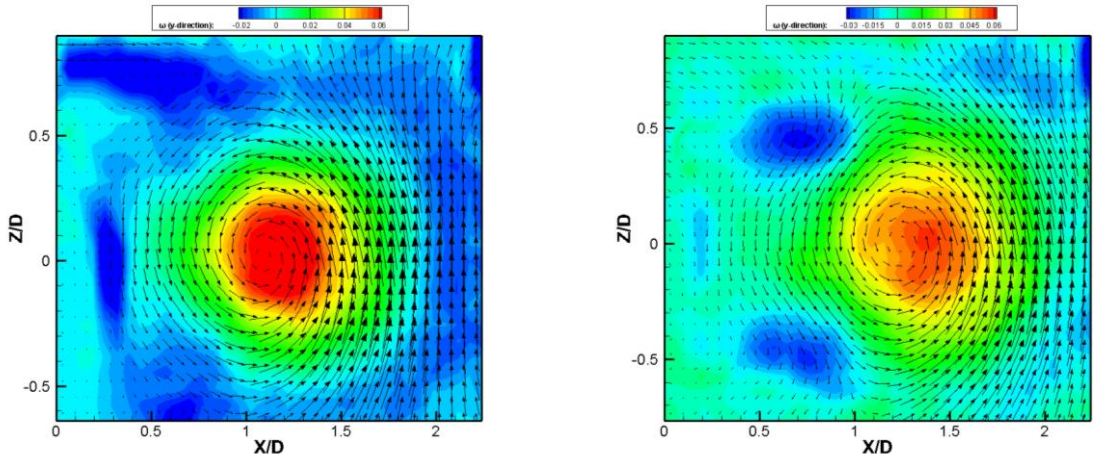

(a) Mode 1, node (d) Mode 1, saddle

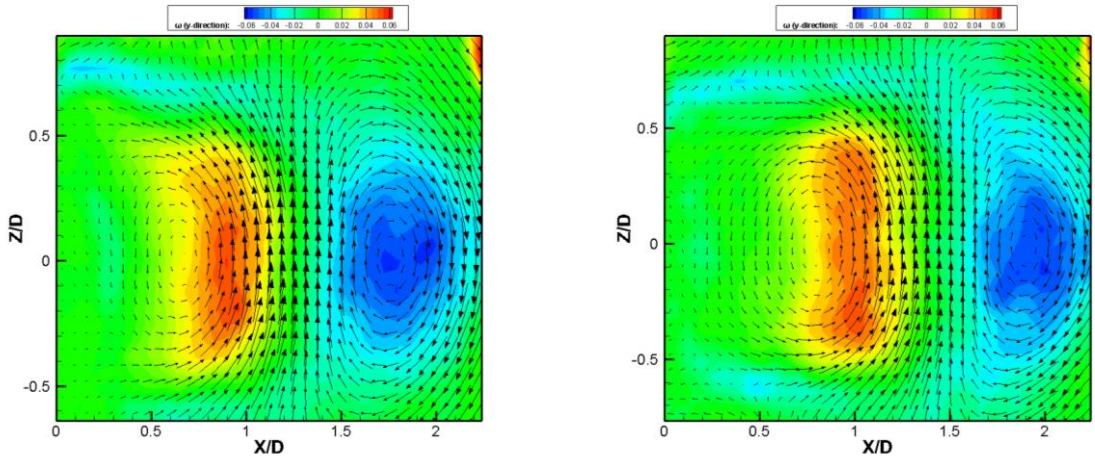

(b) Mode 2, node (e) Mode 2, saddle

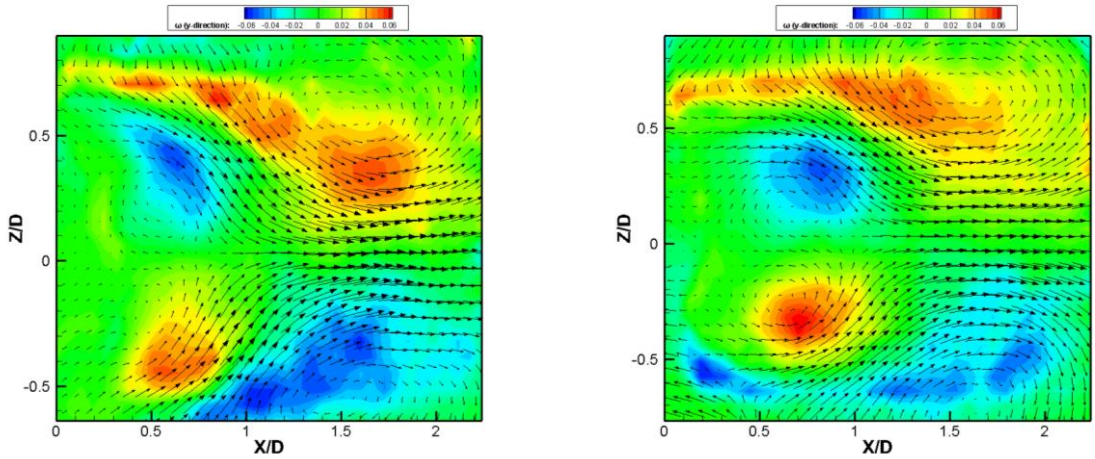

(c) Mode 3, node (f) Mode 3, saddle

Figure 3.41: POD vorticity contour plots at XZ plane (Re = 20,000, λ/D_{mean} = 2.4)
(a) (b) (c) Node plane. (d) (e) (f) Saddle plane

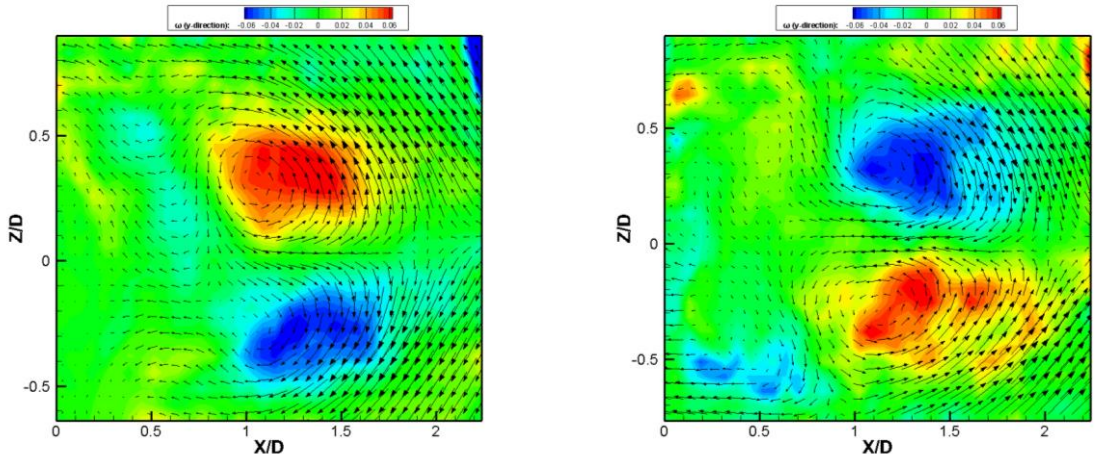

(a) Mode 4, node

(d) Mode 4, saddle

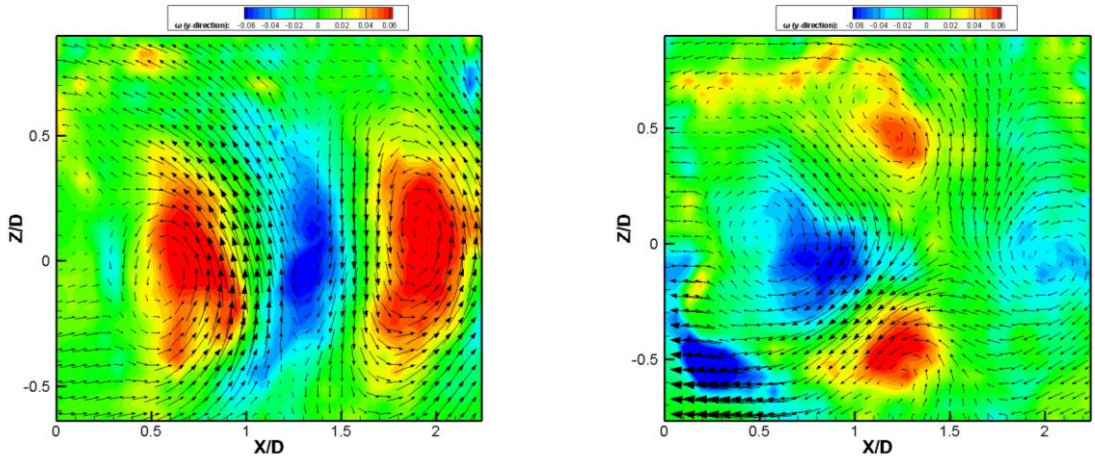

(b) Mode 5, node

(e) Mode 5, saddle

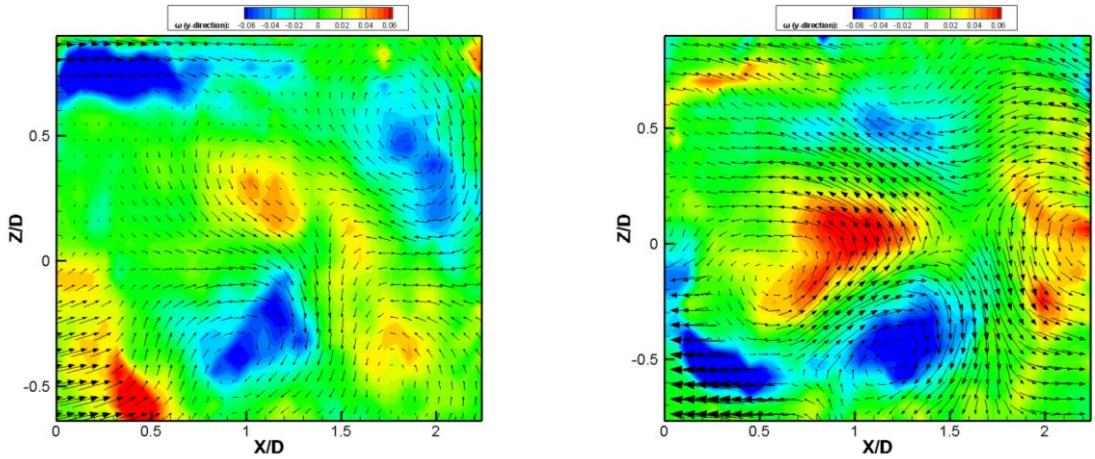

(c) Mode 6, node

(f) Mode 6, saddle

Figure 3.42: POD vorticity contour plots at XZ plane (Re = 20,000, λ/D_{mean} = 2.4)

(a) (b) (c) Node plane. (d) (e) (f) Saddle plane

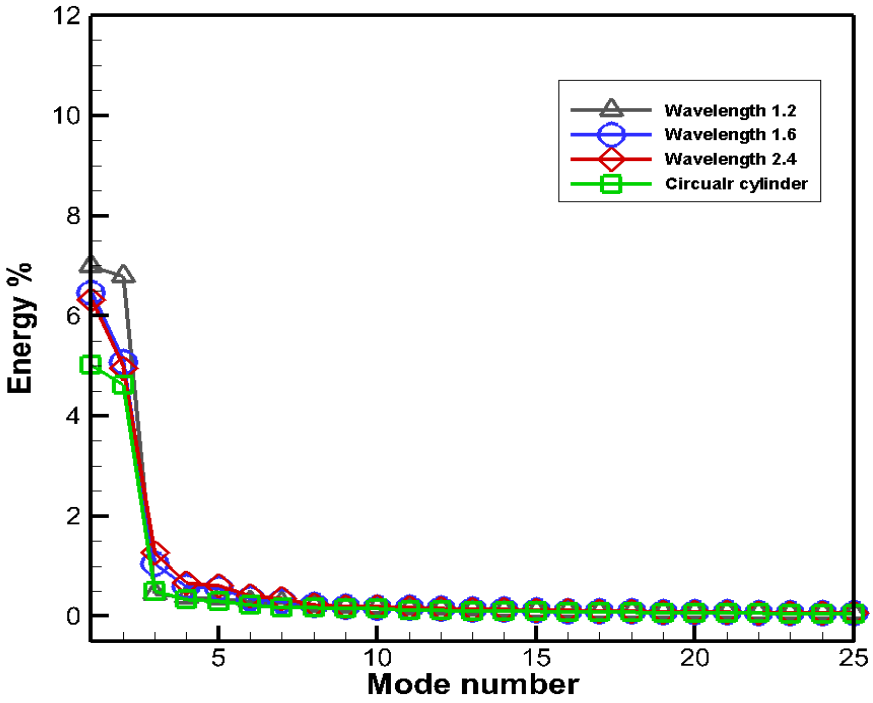

(a) Node

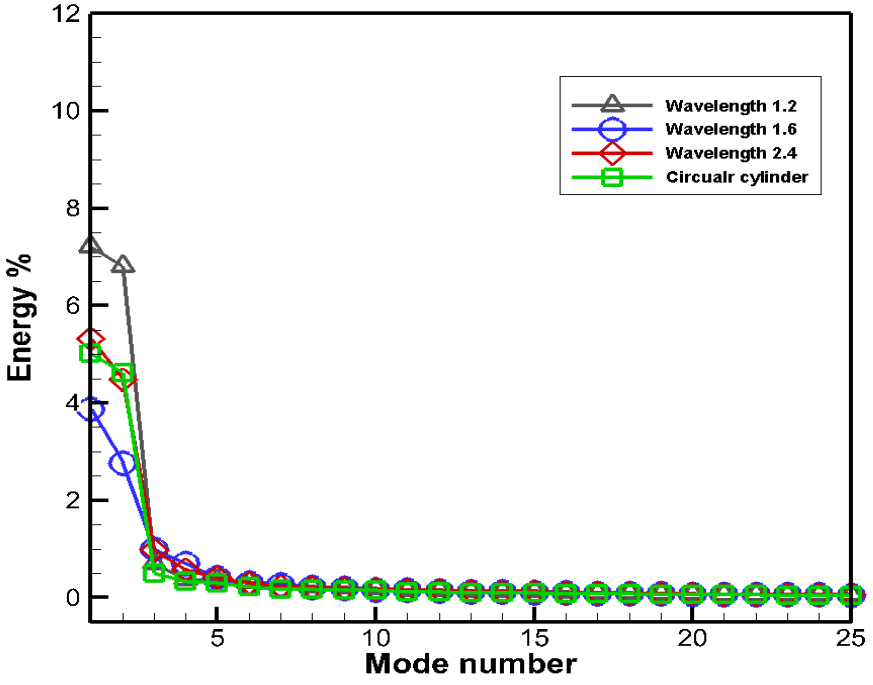

(b) Saddle

Figure 3.43: POD energy distribution plot in different wavelength and straight cylinder at Re = 15,000 (a) Node (b) Saddle

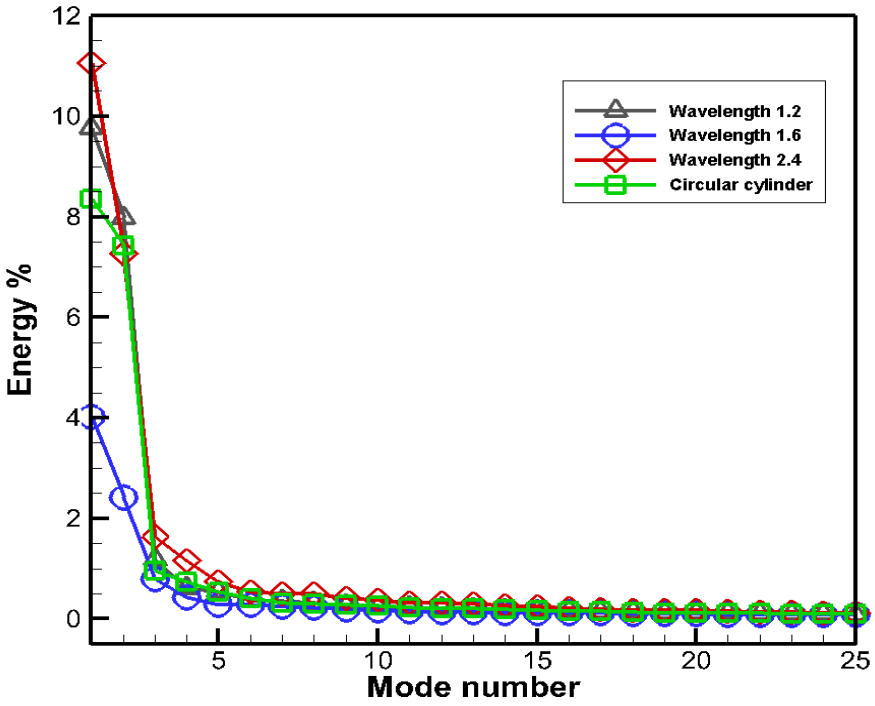

(a) Node

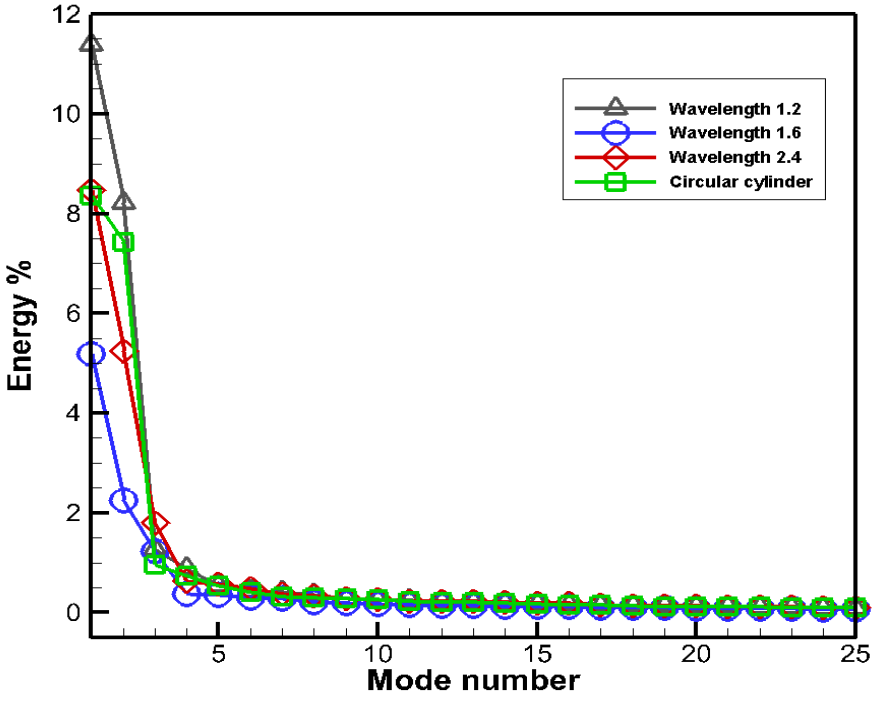

(b) Saddle

Figure 3.44: POD energy distribution plot in different wavelength and straight cylinder at Re = 20,000 (a) Node (b) Saddle

Chapter 4
Conclusions

In this research, the three-dimensional volumetric PIV showed the flow characteristic over the three different wavelength cylinders and straight cylinder. The results displayed that the wake behind the geometric saddle is wider than the wake behind the geometric node, which has a narrower wake due to the different separation line along the spanwise direction. The velocity contour plots also show the sinuous variation velocity along the spanwise direction due to the boundary separating earlier at the geometric saddle and later at the geometric node. Moreover, the recovery speed behind the geometric node is faster than the geometric saddle indicating the Karman vortex formation region. Furthermore, the results clearly show that the wavy geometry will have very unique and significant streamwise vortices formation behind the geometric node when it flows past the wavy cylinder. This is attributed to the different separation line. The boundary layer separates from the geometric saddle and toward the node, then 2D vortices roll up into the streamwise vortex (3D vortex structure) between the geometric node and saddle. The streamwise vortices will diffuse and decay along the downstream, λ/D_{mean} = 1.6 shows the stronger streamwise vortices. Moreover, the streamwise vortices behind the wavy cylinder are different fom the straight cylinder. These unique streamwise vortices play a very important role in eliminating developed Karman vortices by preventing the free shear layer interaction in the near wake behind the wavy cylinder. The streamwise vortices elongated the vortex formation length and are attributed to the free shear layer, and did not form into mature spanwise vortices in the near wake behind the wavy cylinder and delayed the formation into mature spanwise vortex further downstream. The streamwise vortices clearly show a pair of counter-rotating vortices behind the geometric node at the shorter wavelength λ/D_{mean} = 1.2 and λ/D_{mean} = 1.6. However, at wavelength λ/D_{mean} = 2.4 only display a single streamwise vortices on the top and the bottom of geometric node was observed. Furthermore, the spanwise spacing of the streamwise vortices behind the geometric node did not correlate to the cylinder spanwise waviness.

The POD showing the energy distribution at Re = 20,000, the wavelength λ/D_{mean} = 1.6 displays the minimum energy at the geometric node and geometric saddle compared to the straight cylinder and wavelength λ/D_{mean} = 1.2 and λ/D_{mean} = 2.4. This indicated the wavy geometry created the unique flow which effectively suppressed the formation of spanwise vortices and turned into developed the small-scale vortices. Also, the energy behind the geometric saddle is higher than the geometric node; this is attributed to the separated

boundary layers behind the saddles containing a higher level of shear layer turbulence and greater circulation than behind the geometric node the separated boundary layer, which is entrained into the streamwise vortices. POD analysis of the cylinder with wavelength λ/D_{mean} = 1.6 shows less energy at Re = 20,000 and the least overall energy at Re =15,000 this indicated contain less kinect energy at this certain wavelength. Also, mode 5 and mode 6 displays break the large-scale vortex to small-scale structure. The POD shows the overall vortex formation length behind the three different wavelengths wavy cylinders is longer compared to the straight cylinder. The elongated vortex formation length indicated has reduced drag and vibration.

Reference

[1] Zdravkovich, M.M., "Flow around circular cylinders," *Oxford University Press,* 1997.

[2] B. Mutlu Sumer, and Jorgen Fredsoe, " Hydrodynamics around cylinder structures," *World Scientific Pub Co Inc*., 2006

[3] Bearman, P. W., "Vortex shedding from oscillation bluff bodies," *Annual Review of Fluids Mechanics,* Vol. 16, 1984, pp. 195-222.

[4] Dyke, M. Van, "An album of fluid motion," *The Parabolic Press, Stanford, CA,* 1982.

[5] Gerrard, J. H., " The mechanics of the formation of vortices behind bluff bodies," *Journal of Fluids Mechanics,* Vol. 25, 1966, pp. 401-413.

[6] Zhang, W., Dai, C. and Lee, S. J., "PIV measurements of the near-wake behind a sinusoidal cylinder. *Exps. Fluids.* Vol. 38, 2005, pp. 824-832.

[7] Lee, S. J., and Nguyen, A.T., "Experimental investigation on wake behind a wavy cylinder having sinusoidal cross-sectional area variation," *Fluids Dyn. Res.* Vol. 39, 2007, pp. 292-304.

[8] Lam, K. and Lin, Y. F., " Effects of a wavelength and amplitude of a wavy cylinder in cross-flow at Reynolds numbers," *J. Fluids Mech*. Vol. 620, 2008, pp. 195-220.

[9] Ahmed, A and Bays-Muchmore, B., "Transverse flow over a wavy cylinder," *Physics of Fluids* A 4, 1992

[10] Darker, R. M. and Sherwin, S. J., " Flow past a square-section cylinder with a wavy stagnation face," *J. Fluids Mech.* Vol. 426, pp. 263-295, 2001

[11] Lam, K., Wang, F. H., Li, J. Y., and So, R. M. C., "Experimental investigation of the mean and fluctuating forces of wavy cylinder in a cross-flow," *J. Fluids Struct.* Vol. 19, 2004a, pp. 321-334.

[12] Lam, K., Wang, F. H., and So, R. M. C., "Three-dimensional nature of vortices in the near wake of a wavy cylinder," *J. Fluids Struct.* Vol. 19, 2004b, pp. 815-833.

[13] Gerrard, J.H., "vortex-Induced vibrations," *Annual Review of Fluid Mechanics,* Vol.36, 2004, pp.413-455.

[14] Bloor, M. S., "The transition to turbulent in the wake of circular cylinder," *Journal of Fluid Mechanics,* Vol.19, 1964, pp.290-304.

[15] Batchelor, G. K., "An introduction to fluid dynamics," *Cambridge University Press,* 1967

[16] Blevins, R.D., "Flow-Induced vibration 2nd edition," *Krieger publishing*, 1994

[17] Owen, J. C. and Bearman, P. W., "Passive control of VIV with drag reduction," *J. Fluids Struct*, Vol. 15, 2001, pp. 597-605.

[18] Nakamura, H. and Igarashi, T., "Reductions in drag and fluctuating forces for a circular cylinder by attaching cylindrical rings," *Journal of Fluid Science and Technology*, Vol.2, No.1, 2007, pp. 12-22.

[19] Liu, Y. Z., Shi, L. L. and Yu, J., "TR-PIV measurement of the wake behind a grooved cylinder at low Reynolds number," *J. Fluids Struct*, Vol. 27, 2011, pp.394-407.

[20] Shao, C. P., Wang, J. P. and Wei, Q. D., "Visualization study on suppression of vortex shedding from a cylinder," *Journal of Visualization*, Vol.10, No.1, 2007, pp.57-64.

[21] Ahmed, A., Khan, M. J., and Bays-Muchmore, B., "Experimental investigation of a three dimensional bluff body wake," *AIAA Journal*, Vol. 31, 1993, pp.559-563.

[22] Bearman, P. W., and Tombazis, N., "The effects of three-dimensional imposed disturbances on bluff body near wake flows," *Journal of Wind Engineering and Industrial Aerodynamics*, Vol. 49, 1993, pp.339-350.

[23] Tombazis, N., and Bearman, P. W., "A study of three-dimensional aspects of vortex shedding from a bluff body with a mild geometric disturbance," *Journal of Fluids Mechanics*, Vol. 330, 1997, pp. 85-112.

[24] Bearman, P. W., and Owen, J. C., "Reduction of bluff-body drag and suppression of vortex shedding by the introduction of wavy separation lines," *J. Fluids Struct*, Vol.12, 1998, pp. 123-130.

[25] Darker, R. M. and Sherwin, S. J., "Flow past a bluff body cylinder with a wavy stagnation face," *J. Fluids Struct*. Vol. 15, 2001, pp. 587-596.

[26] Owen, J. C., Szewczyk, A. A., and Bearman, P. W., "suppression of Karman vortex shedding. *Phys. Fluids*, Vol. 12, S9, 2000

[27] Kim, J., and Choi, H., "Distributed forcing of flow over a circular cylinder," *Physics of Fluid*, Vol.17, 2005, pp. 033-103.

[28] Keser, H., Unal, M. Fevzi and Bearman, P. W., "Simulation of wake from circular cylinder with spanwise sinusoidal waviness," *Proc. Second Intl Conf. Vortex Methods*, Istanbul, Turkey, 2001, pp.131-137.

[29] Lin, Z., "Force reduction of flow around sinusoidal wavy cylinder," *Journal of Hydrodynamics*, Vol. 21, Issue 3, 2009, pp. 308-315.

[30] Wu J, Sheridan J, Welsh MC, "Velocity perturbations induced by the longitudinal vortices in a cylinder wake," *J Fluids Eng.* 118, 1996, pp. 531-536.

[31] Anindya Chatterjee, "An introduction to the proper orthogonal decomposition," *Current Science, Vol. 78, No.7, 2000*

[32] Stamatios Pothos, Dan Troolin, Wing L., Ragan M., "V3V-Volumetric three-component velocimetry for 3D flow measurements main principle, theory and applications," *Termotehnica*, 2009

[33] Troolin, D. and Longmire, E. "Volumetric velocity measurements of vortex rings from inclined exits," *Exp. Fluids*, 48, 2010, pp. 409-420.

Appendix A

Uncertainty Analysis

The accuracy of the V3V measurement is highly related to the precisely to determining the velocity and particle locations. Velocity accuracy depends on spatial accuracy of particles and timing accuracy [32]. The Nd: YAG laser is utilized and the timing uncertainty is down to 1 ns and the uncertainty is negligible. For particle location the uncertainty of the location in X and Y direction are 20 micron and in Z direction are 80 micron (Dan Troolin, TSI Incorporated)) [33], when particle displacements of 1~8 pixels for both X and Y (1 mm).

In PIV are used to measure the particles displacement to measure the velocity of the fluid. Therefore, the result of velocity by PIV measurement can be expressed as,

$$U = \frac{\Delta X}{K \Delta T} \tag{7}$$

where ΔX is the particle displacement, ΔT is the laser pulse separation time (1100 μs) and K is the magnification (K=0.083692 at reference plane). The particle displacement uncertainty is given by the equation below,

$$\delta \Delta X = \sqrt{[(\varepsilon_1)^2+(\varepsilon_2)^2+(\varepsilon_3)^2]}\Delta X \tag{8}$$

where the uncertainty ε are due to the motion particle loss, in general available from manufacture specification. The advances Gaussian fit algorithm finding the sub-pixel accuracy δΔX = 0.1 pixel. Thus, the velocity uncertainty is obtain from the equation below with the root sum of squares,

$$\delta U = \sqrt{\left\{\left(\frac{\Delta X \delta \Delta X}{K \Delta T}\right)^2 + \left(\frac{\Delta X \delta K}{K^2 \Delta T}\right)^2 + \left(\frac{\Delta X \delta \Delta T}{K \Delta T^2}\right)^2\right\}} \tag{9}$$

the δΔT and δK are represent the uncertainty in the pulse separation time and the uncertainty in the spatial magnification. The uncertainty in the pulse separation δΔT is approximate 1 ns, thus is negligible. The maximum error in the peak finding algorithm δΔX show that the uncertainties in the magnification and the pulse separation are lower. Hence, the uncertainty in the velocity is reduced to

$$\delta U = U_{max}\left(\frac{\delta \Delta X}{\Delta X_{max}}\right) \tag{10}$$

As a result, from the equation above shows the velocity uncertainty in the X direction is 2.17%, in Y direction is 2.17%, and in Z direction is 8.69%.

Appendix B

Water Tunnel Speed Calibration Curve

Figure B.1 shows the water tunnel speed calibration curve, the calibration is by using the V3V camera.

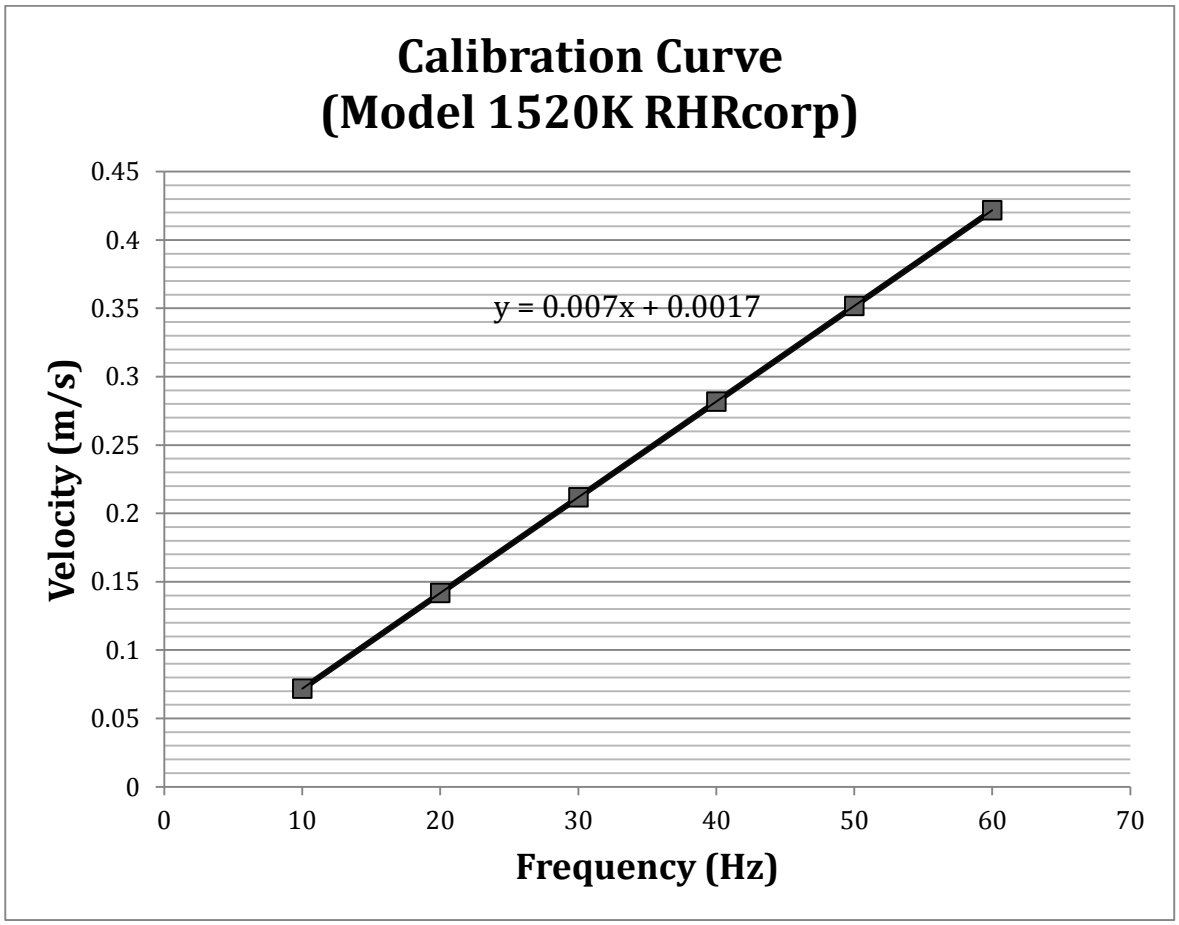

Figure B.1: Water tunnel calibration curve

Appendix C

PIV Multi Plane Calibration Graph

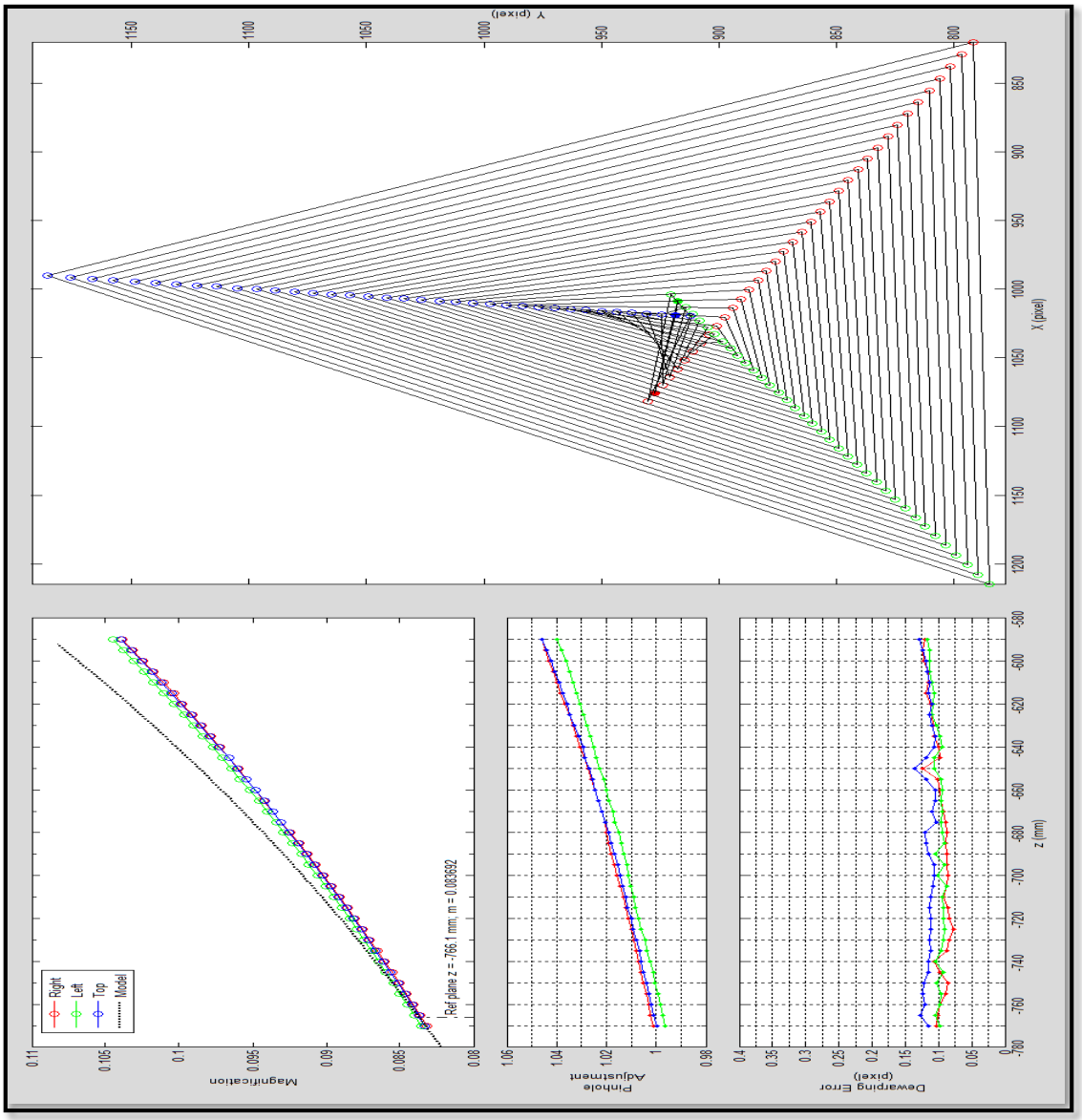

Figure C.1: V3V camera multi plane calibration graph

Appendix D

Data Processing Flow Chart

Figure D.1 shows the V3V processing step to generate the three-dimensional flow field.

Step1: Particle processor

Generated the P2D file by finding the particles from each of the six images. The identification of the particle is discovered by the advanced 2D Gaussian fitting algorithm. Using the particle image to get the information of every pixel then obtain a highly accurate subpixel particle seeds position.

Step 2: Triplet processor

Among the three apertures to match particles and calculate 3D particle location from matched triplets, then produce P3D files that contain the particle 3D positions. The triplet processor first step is to get rid of the error in particle image positions by utilize the V3V 4G calibration. Second, perform the triplet process beginning from the right aperture then moving to the left and top aperture. Finally, the three-matched particle is formed, by deriving the 3D location of the particle in the camera coordinate system.

Step 3: Velocity processor

Track the particles between frame A and frame B then generate the PV3D files that contain the velocities and 3D positions information.

Step 4: Velocity Interpolation processor

To interpolate particle vectors to a regular grid. Due to the particles, vectors are distributed randomly inside the 3D measurement volume. Thus, the interpolation is to acquire velocity data in a regular grid, which is preferred for vortex structure, flow visualization and further analysis.

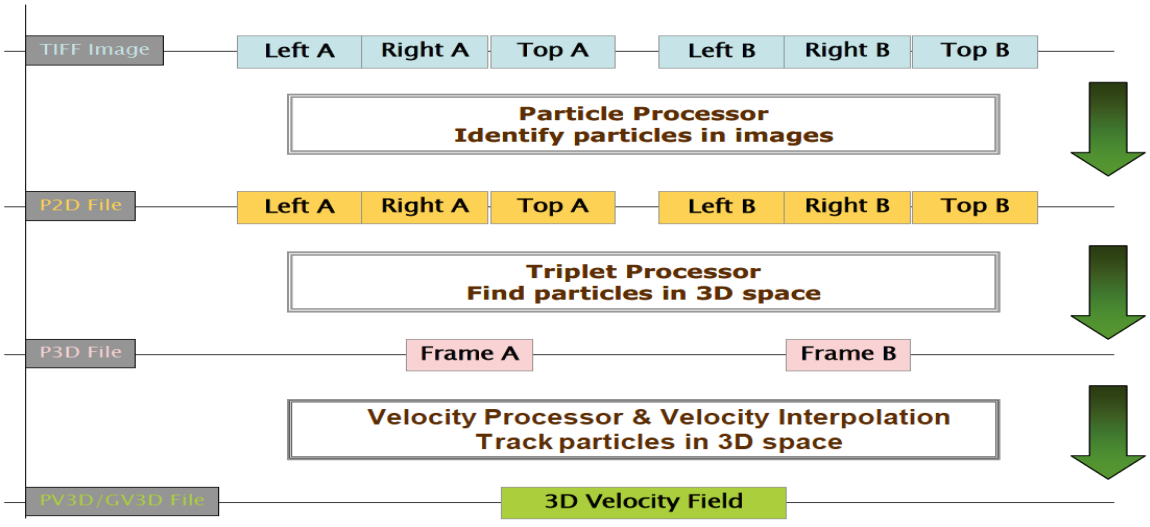

Figure D.1: V3V processing flow chart

Appendix E

Three-Dimensional Flow Field

The figures show the flow over the wavy body with wavelength λ/D_{mean} = 1.2 by a three dimensional graph. Figure E.1 clearly exhibits the flow behind the geometric node has a narrower wake Figure E.2 clearly displays the wake behind the wavy cylinder has a sinuous wave along the spanwise direction and streamwise vortices form near the geometric node. The three-dimensional flow field shows the velocity magnitude by the equation below

$$V = \sqrt{u^2 + v^2 + w^2} \tag{11}$$

and the vorticity by the equation below

$$\begin{bmatrix} \omega_x \\ \omega_y \\ \omega_z \end{bmatrix} = \begin{bmatrix} \frac{\partial w}{\partial y} - \frac{\partial v}{\partial z} \\ \frac{\partial u}{\partial z} - \frac{\partial w}{\partial x} \\ \frac{\partial v}{\partial x} - \frac{\partial u}{\partial y} \end{bmatrix} \tag{12}$$

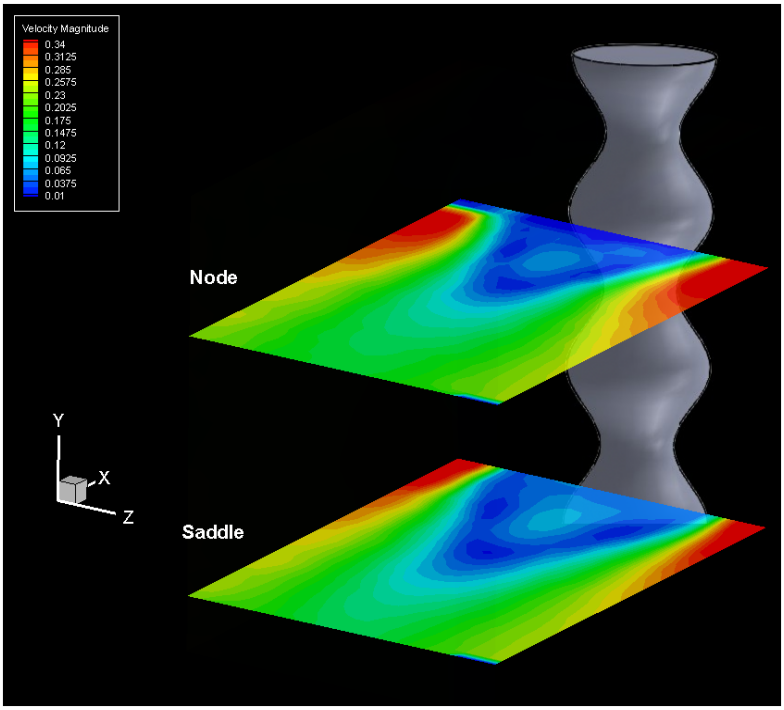

Figure E.1: Velocity contours in node plane and saddle plane
(Re = 20,000, λ/D_{mean} = 1.2)

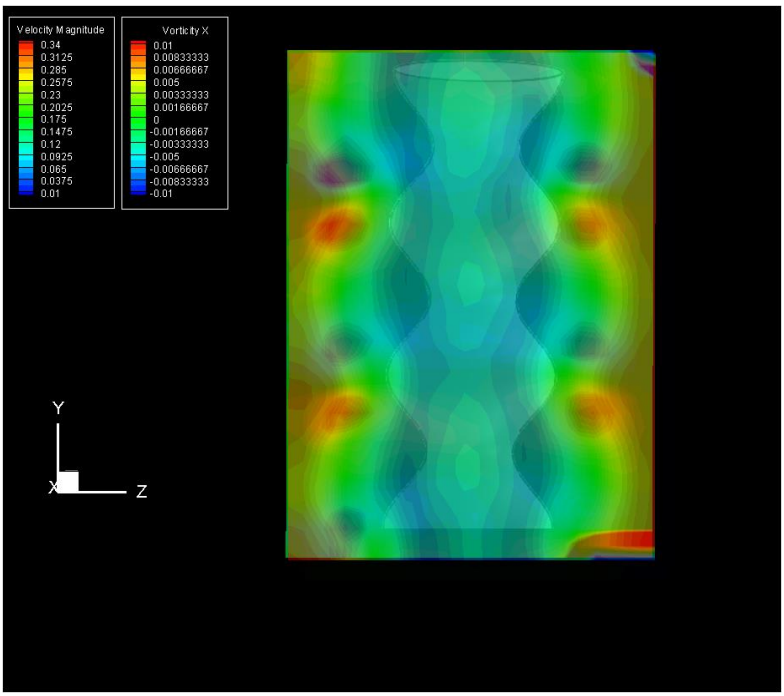

Figure E.2: Velocity and vorticity contours in YZ plane
(Re = 20,000, λ/D_{mean} = 1.2)

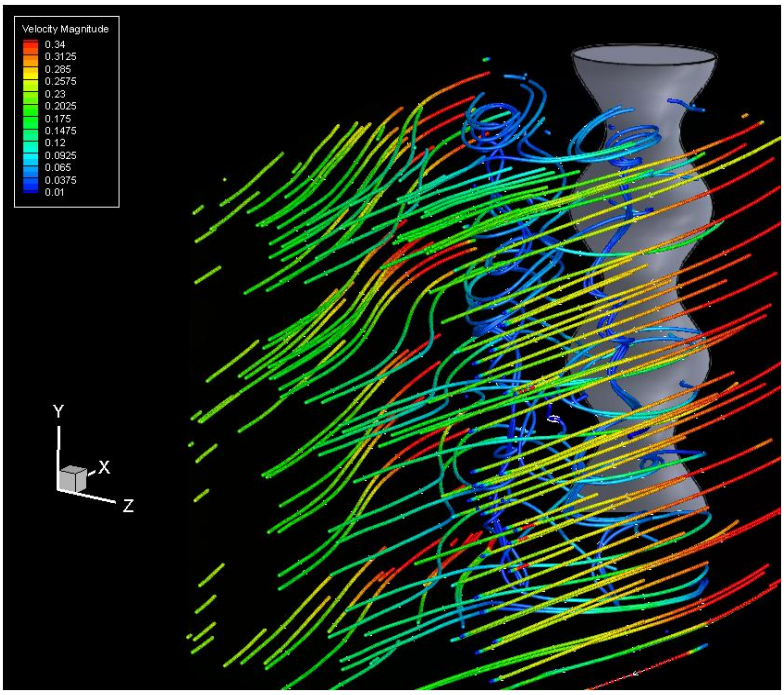

Figure E.3: Streamtrace topology shown flow over the wavy cylinder
(Re = 20,000, λ/D_{mean} = 1.2)

Figure E.4 and Figure E.5 displays the multi plane behind the wavy cylinder; the velocity contour plot shows the velocity variation along the spanwise direction and sinuous shape is correspond to the wavy geometry. Figure E.5 shoes the streamwise vortices formation behind the geometric node and diffuse and decay along the downstream.

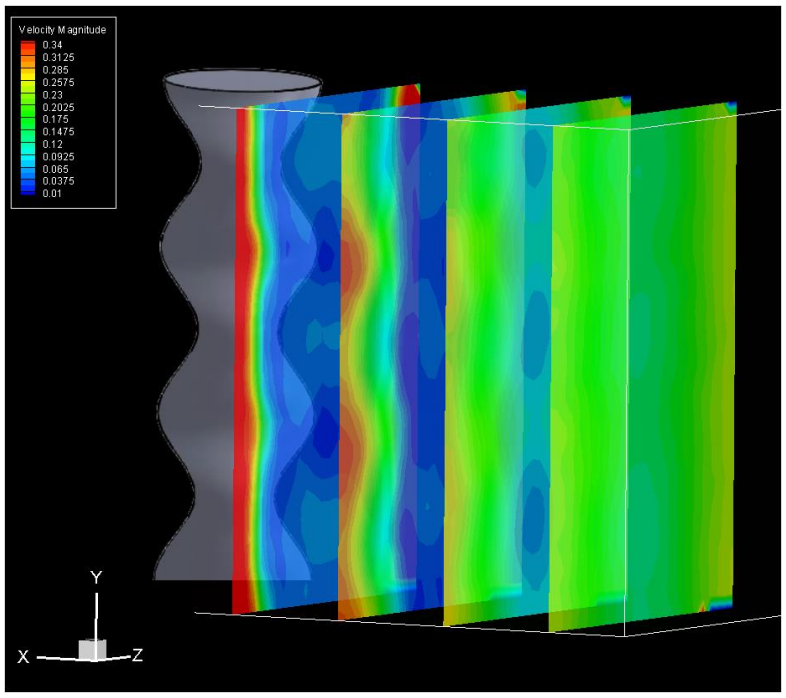

Figure E.4: Velocity contour plots in YZ plane (Re = 20,000, λ/D_{mean} = 1.2)

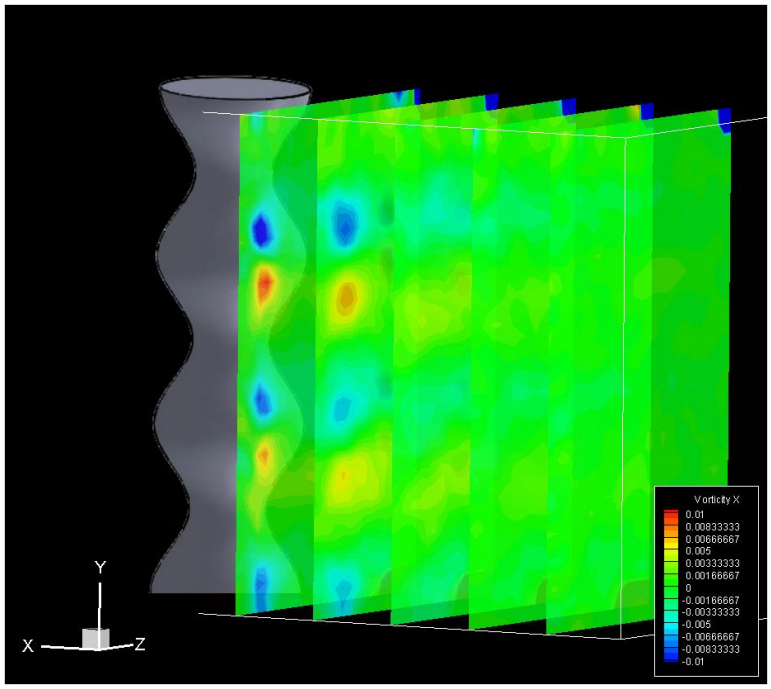

Figure E.5: Vorticity contour plots in YZ plane (Re = 20,000, λ/D_{mean} = 1.2)

Figure E.6 display the velocity isosurface and clearly shown the sinuous variation along the spanwise direction. The vorticity plot exhibit the streamwise developed behind the geometric node.

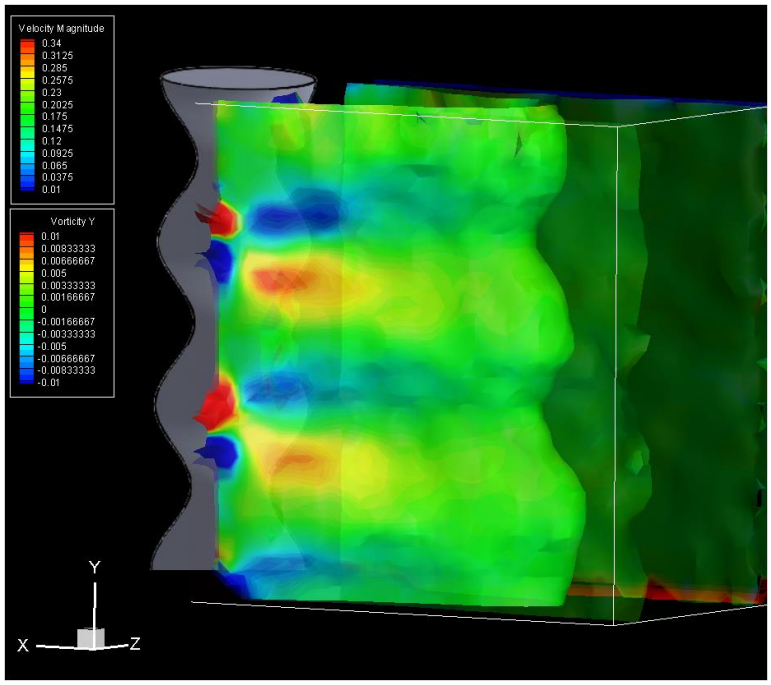

Figure E.6: Isosurface and vorticity contour plots (Re = 20,000, λ/D_{mean} = 1.2)

FigureE.8 shows the streamwise vortices form behind the geometric node and reveal the stronger vortices diffuse further downstream.

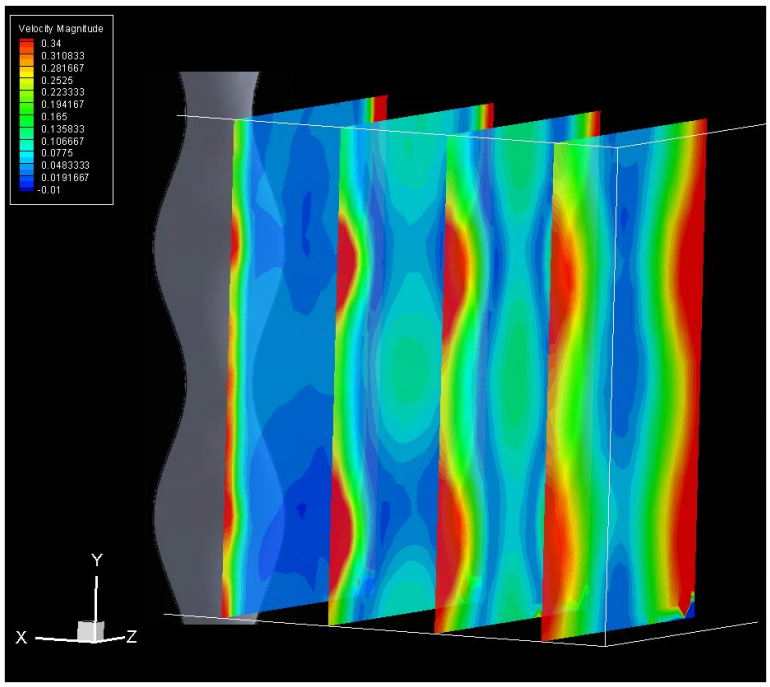

Figure E.7: Velocity contour plots in YZ plane (Re = 20,000, λ/D_{mean} = 1.6)

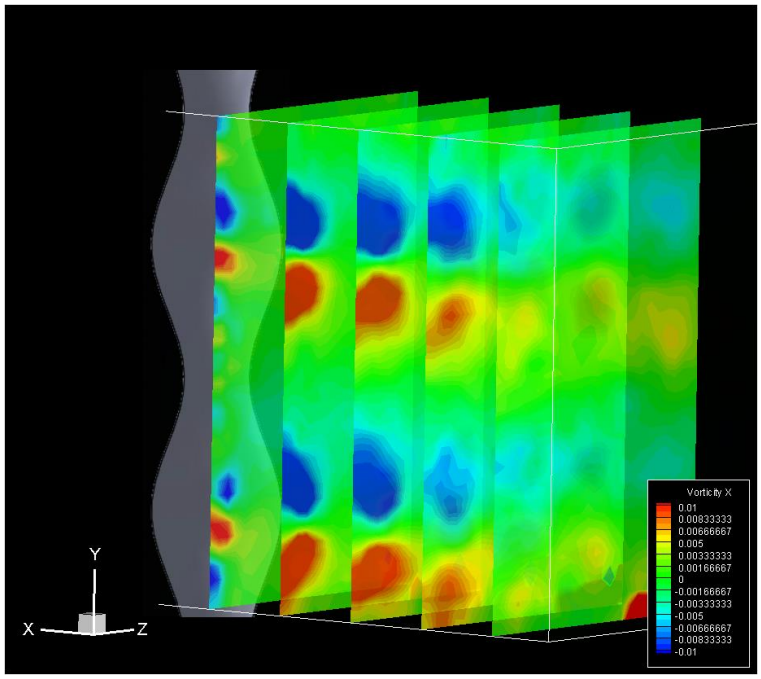

Figure E.8: Vorticity contour plots in YZ plane (Re = 20,000, λ/D_{mean} = 1.6)

Figure E.9 and E.10 displays the velocity isosurface and vorticity, in Figure E.10 adding the streamtrace and clearly exhibit the flow from saddle toward to node then rolling up into streamwise vortices.

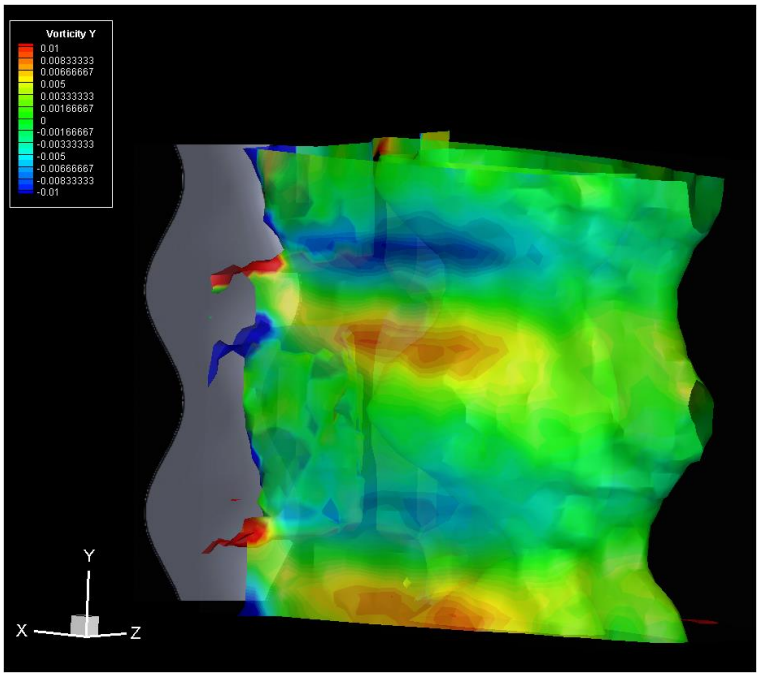

Figure E9: Isosurface and vorticity contour plots (Re = 20,000, λ/D_{mean} = 1.6)

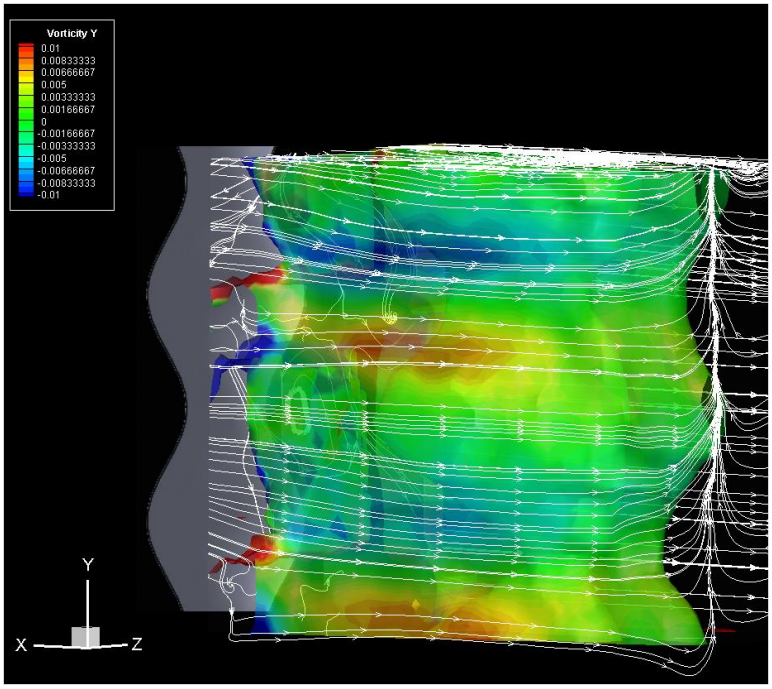

Figure E.10: Isosurface, streamtrace and vorticity contour plots (Re = 20,000, λ/D_{mean} = 1.6)

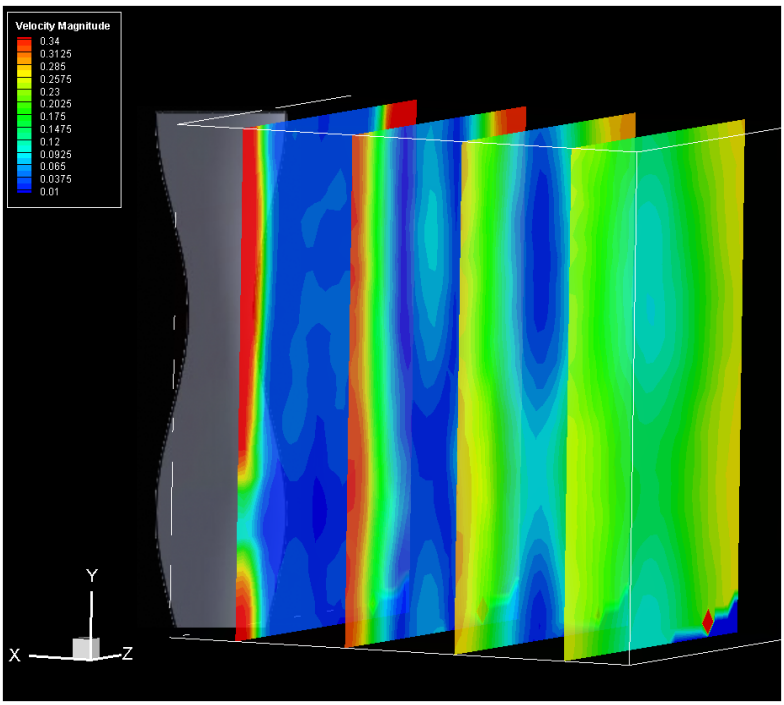

Figure E.11: Velocity contour plots in YZ plane (Re = 20,000, λ/D_{mean} = 2.4)

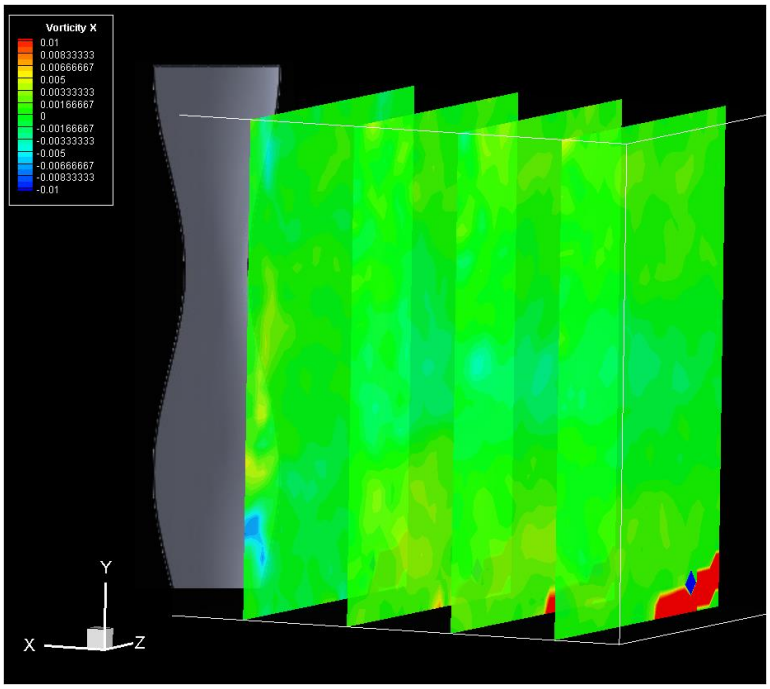

Figure E.12: Vorticity contour plots in YZ plane (Re = 20,000, λ/D_{mean} = 2.4)

Appendix F

Streamtrace Contour Plots

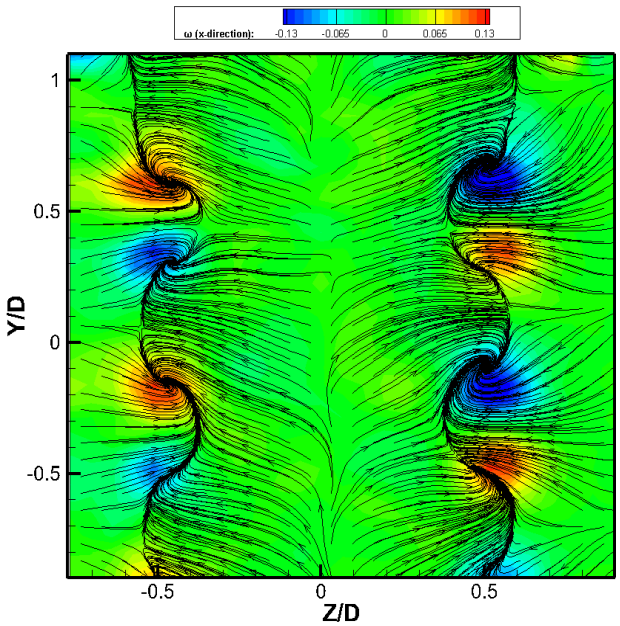

Figure F.1: Streamtrace vorticity contour plots (Re = 15,000, λ/D_{mean} = 1.2, X/D = 0.3)

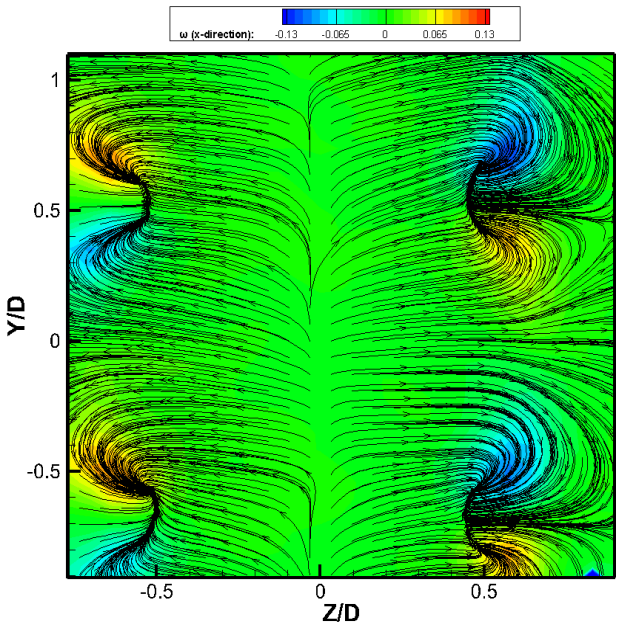

Figure F.2: Streamtrace vorticity contour plots (Re = 15,000, λ/D_{mean} = 1.6, X/D = 0.3)

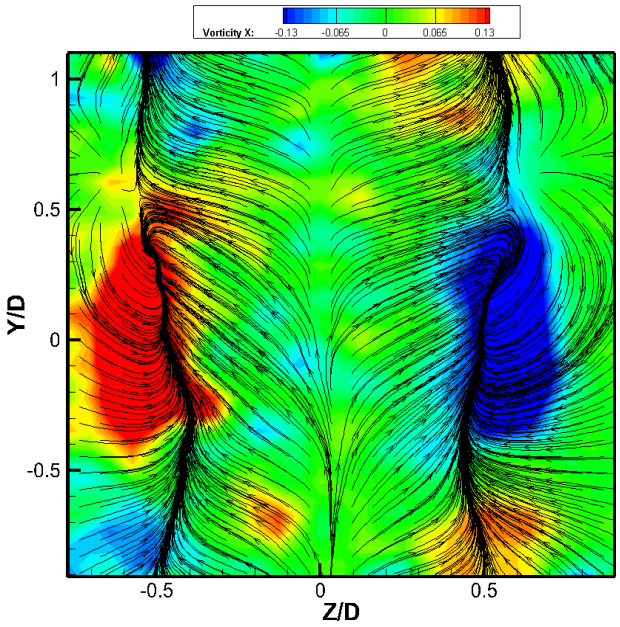

Figure F.3: Streamtrace vorticity contour plots (Re = 15,000, λ/D_{mean} = 2.4, X/D = 0.3)

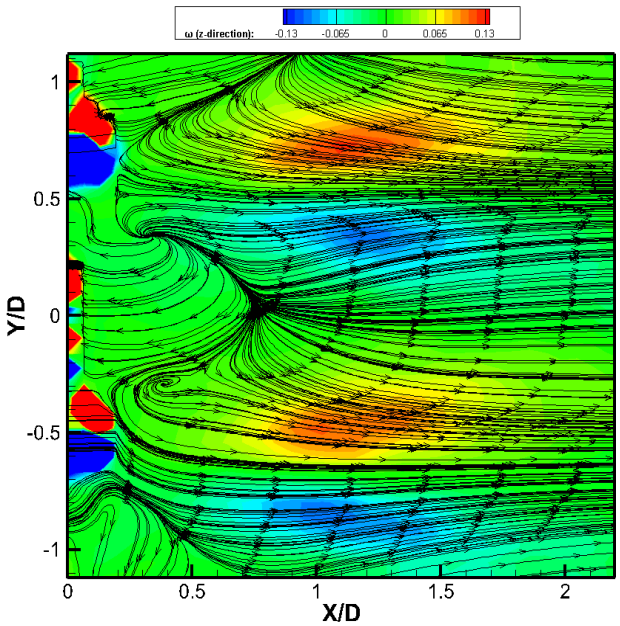

Figure F.4: Streamtrace vorticity contour plots (Re = 15,000, λ/D_{mean} = 1.6, Z/D = -0.45)

Appendix G

V3V Camera Details

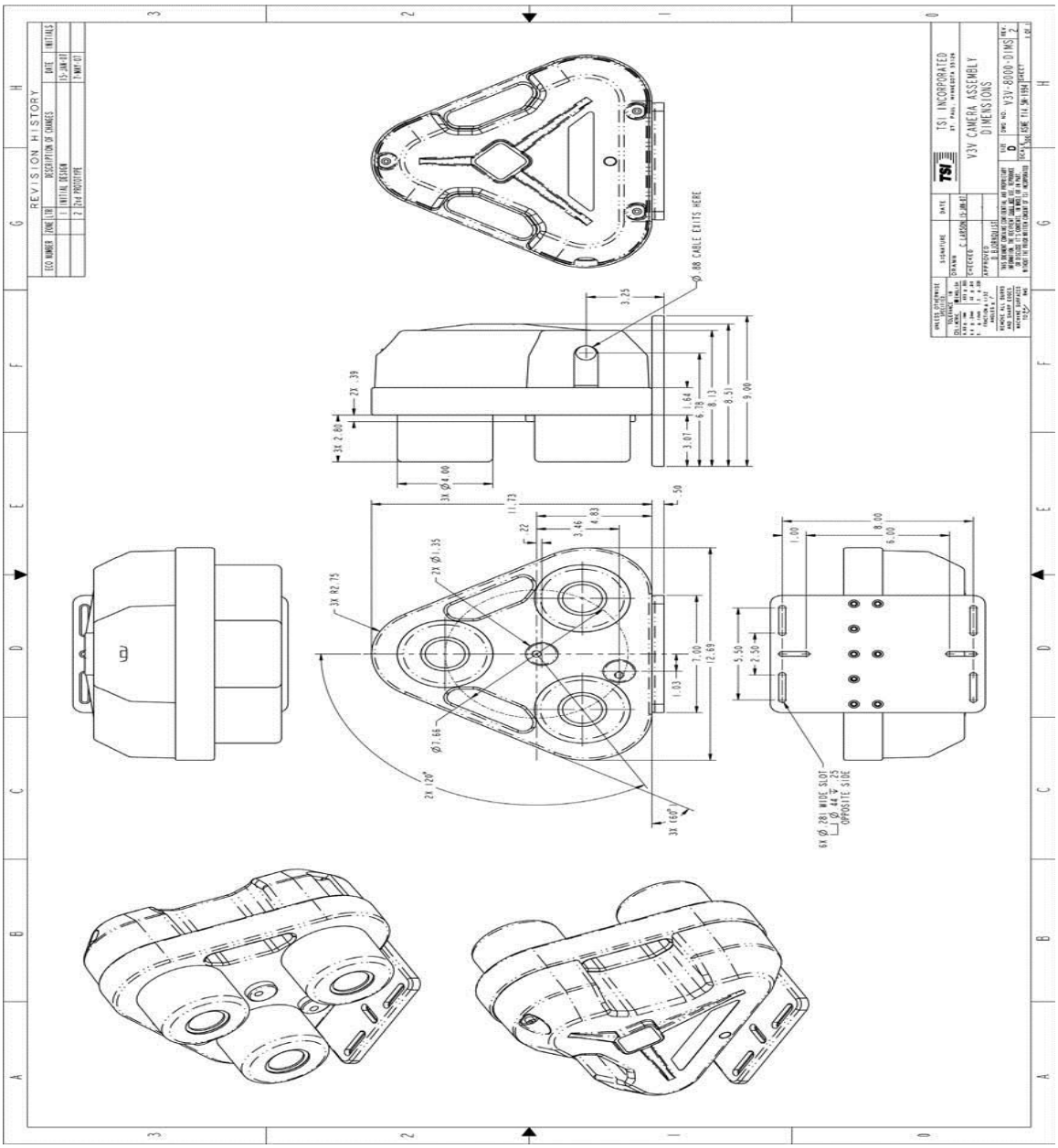

Figure G.1: Details of V3V camera

Appendix H

Water Tunnel Layout

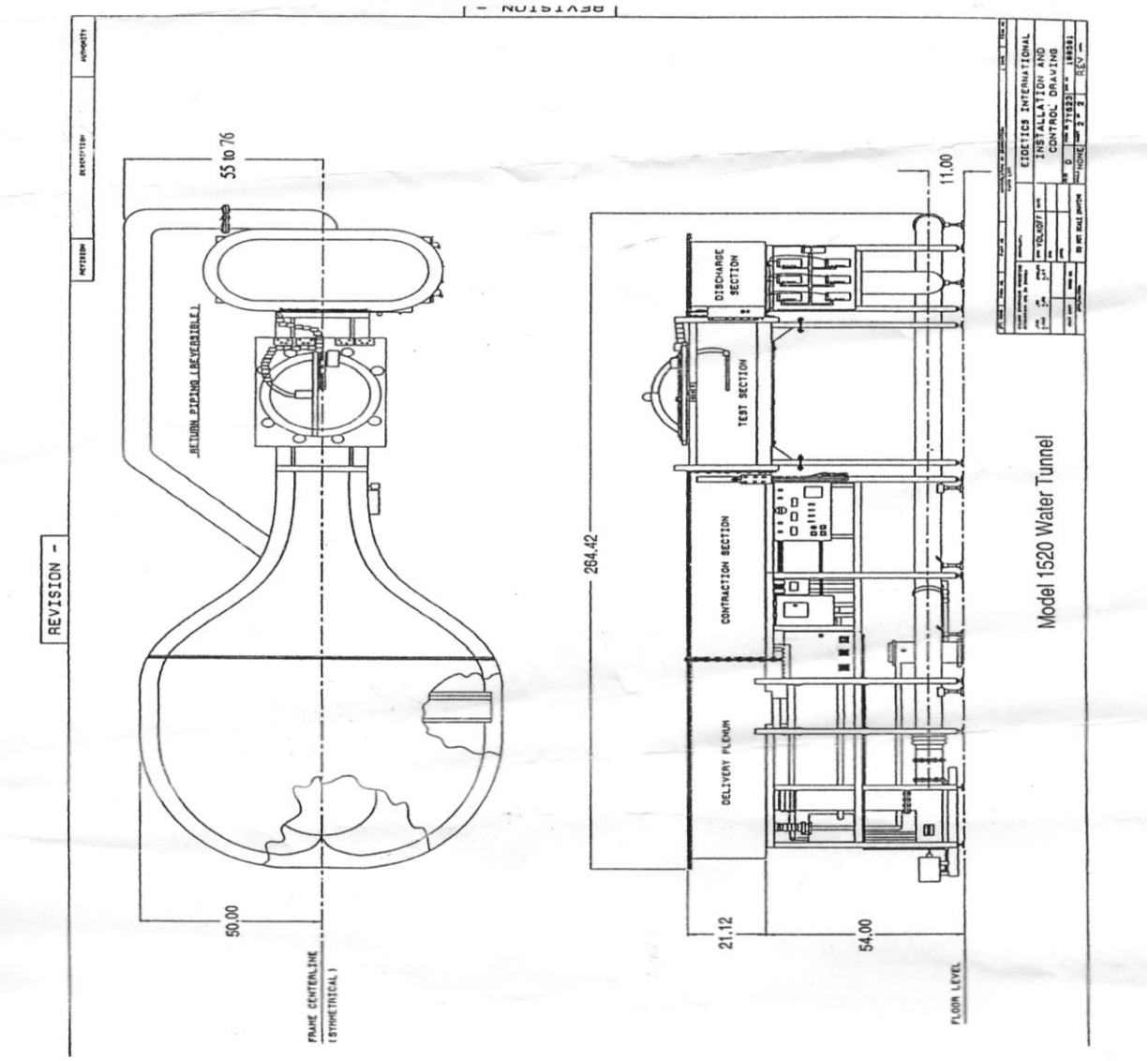

Figure H.1: Details of water tunnel